

The hyperfine interaction as a probe of the microscopic structure of the atomic nucleus

D. Janković,^{1,2,3,*} J. -G. Hartmann,^{2,4,*} J. Bartel,⁵

H. Molique,⁵ L. Bonneau,⁶ and P. -A. Hervieux^{2,†}

¹*Center for Quantum Nanoscience, Institute for Basic Science, Seoul 03760, Republic of Korea*

²*Université de Strasbourg, CNRS, Institut de Physique et Chimie des Matériaux de Strasbourg, UMR 7504, F-67000 Strasbourg, France*

³*Ewha Womans University, Seoul 03760, Republic of Korea*

⁴*Université de Strasbourg, CNRS, Institut de Chimie, UMR 7177 F-67000 Strasbourg, France*

⁵*Université de Strasbourg, CNRS, Institut pluridisciplinaire Hubert Curien, UMR 7178, F-67000 Strasbourg, France*

⁶*LP2i Bordeaux, UMR5797, University of Bordeaux, CNRS, F-33170 Gradignan, France*

(Dated: February 23, 2026)

Abstract

The study of highly charged electronic and muonic hydrogen-like ions, provides an intriguing way to probe the internal structure of their atomic nuclei. In this work, we use nuclear structure calculations to accurately calculate the hyperfine splitting of electronic and muonic hydrogen-like ions, focusing in particular on the incorporation of finite-volume corrections, such as Bohr-Weisskopf and Breit-Rosenthal, due to the penetration of the electron and muon wavefunction into the nuclear electric charge and magnetic dipole densities. These corrections are essential for refining our understanding of the nuclear magnetic dipole and electric quadrupole moments. Our simulations use a Skyrme-Hartree-Fock-BCS model known for its effectiveness in modeling well-deformed nuclei such as $^{159}\text{Tb}^{64+}$ and $^{165}\text{Ho}^{66+}$, with particular emphasis on $^{161,163}\text{Dy}^{65+}$ isotopes. It can also be generalised to multi-electron ions by studying the hyperfine anomaly between two isotopes.

CONTENTS

I. Introduction	4
II. Nuclear description	9
A. The Skyrme effective interaction	10
B. The Skyrme–Hartree–Fock equations	17
C. Cases of spherical and axial symmetries of the nucleus ground-state shape	19
D. Including pairing correlations	22
E. Treatment of odd nuclei	23
F. Calculation of the nuclear charge density	26
G. Calculation of the magnetic dipole moment	29
III. Atomic-structure framework and nuclear-size effects in spectroscopy	35
A. Atomic description	35
B. Multipole expansions of the electric and magnetic potentials	37
1. Electric Potential	37

* These two authors contributed equally

† hervieux@unistra.fr

2. Magnetic potential	39
C. Hyperfine interactions	41
1. Magnetic dipole hyperfine structure constant	41
2. Electric quadrupole hyperfine structure constant	43
D. Isotope Shift	44
1. Breit-Rosenthal correction	44
2. Bohr-Weisskopf correction	45
3. Web of Hyperfine Anomalies	45
4. Hyperfine Anomaly	46
IV. Results and discussions	50
A. Nucleon density distributions and nuclear currents	50
B. Results combining nuclear and atomic descriptions	62
1. Charge corrections	62
2. Magnetic corrections	67
3. Hyperfine anomaly	71
4. Correction of the quadrupole term	72
5. Remark regarding the choice of the empirical nuclear radius	77
V. Conclusions	78
VI. Perspectives	80
VII. Acknowledgements	81
VIII. Appendices	81
A. Intrinsic vs. spectroscopic multipole moments	81
1. General expressions	81
2. Electric quadrupole moment	89
3. Magnetic dipole moment	91
B. Multipole expansion of the magnetic vector potential	92
1. General case	92
2. Magnetic dipole moment	94

C. Hyperfine interactions	95
1. Dipole	95
2. Quadrupole	99
D. Note on the definition of the nuclear radius	101
E. Results for ^{161}Dy	103
References	109

I. INTRODUCTION

Hyperfine interactions serve as a fundamental bridge between atomic and nuclear physics, connecting the electromagnetic properties of the nucleus with the atomic energy levels of the electrons. In a hyperfine transition, the magnetic dipole and electric quadrupole moments of the nucleus interact with the electromagnetic field of the electron cloud, producing small shifts or splittings in atomic energy levels. This phenomenon effectively links two regimes of vastly different scales and characters. The ability of hyperfine measurements to probe nuclear properties has long been recognised as an important avenue for cross-disciplinary insights. Moreover, hyperfine interactions play a crucial role in many physical and chemical processes, with applications ranging from metrology to condensed matter physics and quantum computing on molecular complexes..

In metrology, the definition of the SI second is based on a hyperfine transition ($F = 4 \leftrightarrow 3$) in ground-state ^{133}Cs [1]. More recently, in ^{229}Th nuclear clocks, the hyperfine coupling mediates electronic-bridge and internal-conversion pathways that connect optical electronic excitations to the ~ 8 eV nuclear isomer, critically shaping excitation rates, linewidths, and readout [2–7]. Another example in the field of solid-state physics is ferromagnetic nuclear resonance (FNR), a technique that provides unique insights into ferromagnetic films, multilayers, and nanocomposites. Its spectra reveal the distribution of hyperfine fields, offering valuable information about chemical configurations, site symmetries, phases, structures, and defects [8]. Finally, even in emerging areas like quantum information, hyperfine couplings between electron and nuclear spins are exploited for qubit storage and control [9–11], reflecting the same fundamental interaction at work in disparate contexts. These examples highlight how hyperfine spectroscopy provides a common thread linking atomic-scale measurements to nuclear-scale phenomena, albeit one that demands both high precision and careful disentangling of nuclear and electronic contributions.

Likewise, muonic atoms – where an electron is replaced by a heavier muon – dramatically magnify hyperfine effects, allowing nuclear charge and magnetisation distributions to be extracted with high sensitivity [12, 13].

One fundamental challenge in hyperfine physics is therefore the enormous disparity in spatial scale between the nucleus and the atom. The atomic electron cloud extends over tens of thousands of fermis, while the nucleus occupies only a few fermis. As a consequence, the overlap of the electronic wavefunction with the tiny nucleus is extremely small. Bridging this gap with reliable theory is difficult: atomic physicists must incorporate nuclear-structure corrections, and nuclear physicists must deliver those corrections in a form useful for atomic calculations.

Traditionally, simple nuclear models have been used to approximate the nucleus in hyperfine calculations. In the most naive picture, one treats the nucleus as a point-like source of charge and magnetism. This approximation often suffices for order-of-magnitude estimates. More refined descriptions introduce spherical or Fermi-like charge distributions and uniformly magnetised spheres, to capture finite-size corrections – known respectively as the Breit-Rosenthal (BR) and Bohr-Weisskopf (BW) effects [14–16]. Yet such parametrisations come with limitations: they may capture the gross nuclear radius but not detailed variations in deformation or the distinct contributions of orbital and spin currents to the magnetic dipole moment. In heavy or deformed nuclei, and in particular muonic ions, these simplifications can introduce significant uncertainties.

These deviations manifest empirically as hyperfine anomalies: departures from the expected scaling of hyperfine constants with nuclear moments across isotopes. Such anomalies encode nuclear-structure effects that are not captured by point-like or simplistic models and can therefore serve as indirect diagnostics. Very few studies have investigated this matter [17]. Crucially, hyperfine anomalies can be exploited in ways that negate *electronic* uncertainties in such measurements. By taking specific combinations or differences of hyperfine measurements, physicists can design observables that are largely independent of the atomic wavefunction in the region of the nucleus, thereby isolating nuclear structural effects. A prominent example is the “specific difference” between hyperfine splittings in hydrogen-like (H-like) and lithium-like (Li-like) heavy ions, designed to eliminate electronic-structure uncertainties [18].

Motivated by these challenges, in the present study we go beyond traditional models by implementing a microscopic nuclear-structure framework based on the Skyrme-Hartree-Fock (Skyrme-HF) model, including Bardeen-Cooper-Schrieffer (BCS) pairing correlations [19]. We shall refer

to this framework as Skyrme-HF-BCS, or equivalently the abbreviated “HFBCS”. This method is well-suited for describing deformed and open-shell nuclei close to the valley of β -stability, and provides spatially-resolved charge and current densities directly from nuclear many-body structure. An important benefit of using Skyrme-HF-BCS densities is the ability to *dissect the origin of the nuclear magnetisation*: we can compute separate contributions to the hyperfine constant coming from the motion of charged nucleons (orbital magnetism) versus their intrinsic spin alignment (spin magnetism). This opens a new window onto the magnetic hyperfine constant a : rather than obtaining only an empirical a -value, we can quantify how much of it is due to, say, a polarised looping current from a core proton as opposed to a net spin alignment of an unpaired neutron. Similarly, our microscopic approach naturally yields the nuclear electric quadrupole tensor, allowing us to compute the electric quadrupole hyperfine constant b without assuming a point-like quadrupole moment. We can thereby study how nuclear deformations (deviations from sphericity) influence b , an effect usually collapsed into a single number Q (the electric quadrupole moment) in conventional treatments.

The rare-earths are home to some of the largest observed nuclear deformations; dysprosium, in particular, has a rich isotopic spectrum (36 isotopes, 7 of which are stable) and contains some of the most prolate known nuclei. In addition, the dysprosium atom plays a major role in quantum computing because it carries a partially filled f -electron shell – characteristic of the lanthanide family – and can be chemically protected by suitable ligands. Molecular complexes such as TbPc_2 exhibit hyperfine levels that can be selectively addressed using radio-frequency pulses of different energies. This addressability is enabled by the hyperfine constant b , which is directly linked to nuclear deformation. The tuning of this parameter for optimisation – such as by substituting isotopes within the molecule, producing different isotopologues – lies at the core of the quantum-computing strategy developed over several years by Ruben’s and Wernsdorfer’s groups at KIT [20]. Indeed, it is the non-equidistant hyperfine energy levels arising from nuclear deformation that are essential for implementing quantum algorithms in these molecular complexes (for example, Grover’s quantum search algorithm on TbPc_2 [10]). Consequently, microscopic modeling of the hyperfine interaction in dysprosium and its isotopes remains a central challenge in this field.

By validating our calculations against the known magnetic dipole moments and electric quadrupole moments of dysprosium, we can verify that the Skyrme-HF-BCS model reproduces empirical nuclear observables before predictions are made for hyperfine constants. In addition to our primary

focus on the even-proton isotopes ^{161}Dy and ^{163}Dy , we also compute and analyse nuclear densities and currents for neighbouring odd-proton isotopes ^{159}Tb and ^{165}Ho . These nuclei provide valuable comparative baselines for exploring systematic trends and the interplay of nuclear structure and magnetic observables across isotopic and isotonic chains. The key novelty of this microscopic approach compared with phenomenological models is that it naturally incorporates deformation, shell structure, core polarisation and the interplay of proton and neutron contributions in both charge and magnetisation densities, and yields observables compatible with measurements without requiring free parameters from experiments.

On the atomic side, we focus on hyperfine interactions in highly charged hydrogen-like ions of the element dysprosium, specifically the aforementioned isotopes: ^{161}Dy and ^{163}Dy . In such ions, with only a single electron bound to a high- Z nucleus, theoretical calculations are comparatively clean: any electron-electron correlation is absent, and the one-electron Dirac equation can be solved to very high precision for a given nuclear potential. At the same time, as already mentioned, the calculation of the hyperfine anomaly of these two isotopes in the single-electron case already provides insight into the multi-electronic case, as its calculation largely cancels electronic uncertainties, thus isolating nuclear effects. Moreover, the strong electric and magnetic fields near a bare $Z = 66$ nucleus amplify relativistic effects, making this regime a demanding test of theory. We therefore employ a fully relativistic (Dirac) framework for the bound electron to properly account for high- Z kinematics (e.g. the $1s$ electron in Dy^{65+} moves at a significant fraction of the speed of light). The QED or radiative corrections (vacuum polarisation and self-energy) are then of the order of a few percent of the total energy of the hyperfine transition [21]. These corrections must be considered if the total energy of the hyperfine transition is to be accurately determined. Since the latter has already been the subject of extensive studies [22–27], in this work we only focus on the corrections due to the effect of the finite nucleus on the classical electromagnetic potentials. Our work coupled with QED corrections can produce theoretical predictions comparable with modern high-precision experiments, enabling sensitive tests of nuclear structure or potential physics beyond the Standard Model.

Importantly, we extend this analysis to muonic hydrogen-like dysprosium ions. Since the muon’s Bohr radius is much smaller, its wavefunction overlaps more strongly with the nucleus, thereby amplifying the sensitivity to nuclear structure by several orders of magnitude compared with the electronic case. Consequently, differences between nuclear-model approximations lead to

measurable differences in Bohr-Weisskopf and Breit-Rosenthal corrections, hyperfine anomalies, and quadrupole shifts. We show that, unlike electronic H-like dysprosium – where such differences may be masked by electronic uncertainties – muonic systems allow these distinctions to emerge clearly, and are reachable with current experimental capabilities. Muonic atoms, therefore, stand out as promising benchmarks for refining microscopic nuclear models. Moreover, the close proximity of the muon to the nucleus inverts the hierarchy of the dipolar and quadrupolar shifts, resulting in much larger quadrupolar effects [28] and the ensuing “hyperfine quadrupole anomaly”, which are also subjects of this work.

In essence, the isotopes investigated in this study allow us to demonstrate how a detailed nuclear-structure model can improve the interpretation of hyperfine data for mid- Z nuclei, which are heavy enough to demand relativistic treatment yet light enough that laser spectroscopy of H-like ions may be feasible, with modern high-intensity beams even providing the relevant infrastructure for muonic matter [29].

The remainder of this article is organised as follows. In Sec. II we present the nuclear-structure framework used in this work: the Skyrme effective interaction, the Skyrme-Hartree-Fock equations for spherical and axially deformed ground states including BCS pairing correlations, the treatment of odd nuclei, and the extraction of the nuclear charge densities and magnetic dipole moments. Section III is devoted to the atomic-structure framework of this work: in subsection III A we summarise the atomic description of highly charged hydrogen-like ions and the relativistic one-electron wavefunctions used in the calculations. Subsection III B is devoted to the multipole expansion of the electric and magnetic potentials generated by the microscopic nuclear charge and current distributions; we discuss in particular the electric monopole and quadrupole contributions, and the magnetic potential. In subsection III C we define the hyperfine interaction and introduce the magnetic dipole and electric quadrupole hyperfine-structure constants that will be our main observables. Subsection III D discusses the isotope shift: we review the Breit-Rosenthal and Bohr-Weisskopf finite-size corrections, introduce a hierarchical scheme for composing hyperfine anomalies across increasingly realistic nuclear charge and current models, going from point-like to more involved models, and define the magnetic-dipole and electric-quadrupole contributions to the anomaly. Our numerical results and their discussion are presented in Sec. IV. We first analyse the nucleon density distributions and nuclear currents obtained from the Skyrme-HF-BCS calculations for ^{159}Tb , ^{161}Dy , ^{163}Dy , and ^{165}Ho , and then combine the nuclear and atomic ingredients to evaluate charge

and magnetic corrections to the hyperfine constants, the resulting hyperfine anomaly, and the correction to the electric-quadrupole term for the $^{161}\text{Dy}^{65+}$ and $^{163}\text{Dy}^{65+}$ electronic and muonic ions. Finally, Sec. V contains our conclusions and perspectives.

II. NUCLEAR DESCRIPTION

The general goal of low-energy nuclear theory is to obtain a precise description of the structure of nuclei and their elementary excitation and decay modes. There are two fundamental difficulties in the realisation of this project. First of all, since the nucleus is generally composed of a rather large number of protons and neutrons, it constitutes an N -body problem which (except for very small nuclei at the very beginning of the nuclear table) cannot be solved exactly, as is the case for the atomic problem. An additional problem arises from the fact that, unlike the atomic problem (where the interaction between the electrons is the exact Coulomb interaction), the interaction between the nuclear constituents (protons and neutrons), which is mainly due to the strong interaction, is known only very approximately. Indeed, although the bare interaction between two nucleons is rather well known, it is not so between two nucleons in the nuclear environment, i.e. in the presence of all the other $N - 2$ nucleons. It then becomes inevitable to use some approximations. Moreover, a three-nucleon contribution is expected in addition to the two-nucleon interaction. The Hartree-Fock (HF) approach allows one to find a variational solution of the nuclear N -body problem by requiring that the total nuclear energy of a Slater determinant many-body wave function is minimal with respect to a simultaneous variation of the wave functions of the N particles, as is done in atomic physics [30]. As a result, there exists a mean field potential V to which all nucleons are subject and which is generated by the interaction of all nucleons with each other. Such an approximation is indeed justified, since the distance between two nucleons inside the nucleus is large compared to the correlation length (the so-called *healing distance*). It is therefore possible to perform a HF calculation with a nucleon-nucleon interaction, but this is an interaction in the nuclear medium. This two-body interaction is therefore far from being the bare interaction between two free nucleons, for the simple reason that it takes into account the correlations between the nucleons, among which the *Pauli principle* plays an important role. One then speaks of an *effective interaction*, which can in principle be obtained from the *bare* (or *free*) nucleon-nucleon interaction by the method proposed by Brueckner [31], but which has to be corrected for an important density dependence, as shown

by Negele [32]. The effective interaction obtained in this way is often referred to as the Brueckner G matrix derived from a given bare nucleon-nucleon interaction. Such Brueckner-Hartree-Fock calculations do exist, though mostly for infinite nuclear matter, or by considering the finite nucleus as composed of pieces of nuclear matter at a given local density (see e.g. [32–35]), but they are generally extremely time-consuming. It is therefore essentially out of the question to perform such calculations on a large scale for finite nuclei.

A. The Skyrme effective interaction

It is then necessary to resort to what is often called *phenomenological effective interaction*, which attempts to model the interaction between the nucleons inside the nucleus in some analytical form, taking into account the essential components of the bare interaction. This interaction is of course finite, vanishing at distances beyond about 2 fm, with an attractive component between 1 and 1.5 fm, and becoming strongly repulsive at short distances below ≈ 0.7 fm. One could imagine a linear combination of two functions of Gaussian form, one attractive with a width of about 1.2 fm, the other strongly repulsive with a width of about 0.7 fm. As we will see below, Gogny proposed such a finite-range effective interaction [36, 37], which, almost 50 years later, is still one of the most successful phenomenological effective interactions.

In light of the short-range nature of the nucleon-nucleon interaction, a direct approach would be to parameterise it using a Dirac delta distribution. This would effectively account for the short-range character of the strong interaction in the extreme limit. Such interactions include Moszkowski’s modified delta force [38] and the interaction originally proposed by Skyrme [39]. The latter has been the subject of substantial research and has enjoyed considerable success following the pioneering work of Vautherin and Brink [40, 41]. In its original form [40], the nuclear part of this interaction can be expressed in coordinate space as follows

$$V_{\text{Sk}} = V_{\text{Sk},2} + V_{\text{Sk},3} , \quad (1)$$

i.e. as a sum of a two-body potential

$$\begin{aligned} V_{\text{Sk},2}(\vec{R}_1, \vec{R}_2) = & t_0 \left[1 + x_0 P_\sigma \right] \delta(\vec{R}_{12}) + \frac{1}{2} t_1 \left[\delta(\vec{R}_{12}) \vec{k}^2 + \vec{k}'^2 \delta(\vec{R}_{12}) \right] \\ & + t_2 \vec{k}' \cdot \delta(\vec{R}_{12}) \vec{k} + iW_0(\sigma_i + \sigma_j) \cdot [\vec{k}' \times \delta(\vec{R}_{12}) \vec{k}] , \end{aligned} \quad (2)$$

and a three-body term

$$V_{\text{Sk},3}(\vec{R}_1, \vec{R}_2, \vec{R}_3) = t_3 \delta(\vec{R}_{12}) \delta(\vec{R}_{23}) , \quad (3)$$

where the coefficients t_i , x_i and W_0 are defined as constant parameters, which serve to define the Skyrme force and where \vec{R}_{12} in Eqs. (2) and (3) stands for the relative distance $\vec{R}_{12} = \vec{R}_1 - \vec{R}_2$ between the nucleons, \vec{k} for the operator $(\vec{\nabla}_1 - \vec{\nabla}_2)/2i$ acting on its right and \vec{k}' its Hermitian conjugate, i.e. the operator $-(\vec{\nabla}_1 - \vec{\nabla}_2)/2i$ acting on its left. The operator P_σ is the spin-exchange operator and σ_i , $i = 1, 2, 3$ in Eq. (2) are the Pauli matrices. It can be shown (see e.g. [40]) that the first three terms of Eq. (2) can be obtained, in the short-range limit, from a finite-range central force of Gaussian type including exchange terms. The last term in Eq. (2) is a zero-range two-body spin-orbit potential. Note that, due to the presence of a δ distribution in the two-body potential, no other exchange operators, such as P_r (position exchange) or P_τ (isospin exchange), are required in $V_{\text{Sk},2}$.

Furthermore, as demonstrated in [40], when time-reversal symmetry is respected, as is the case in the ground state of even-even nuclei, the three-body potential in Eq. (3) is equivalent to a density-dependent two-body interaction

$$V_{\text{Sk},3}(\vec{R}_1, \vec{R}_2, \rho) = \frac{1}{6} t_3 \left[1 + x_3 P_\sigma \right] \delta(\vec{R}_{12}) \rho(\vec{\mathcal{R}}_{12}) , \quad (4)$$

where ρ is the total nucleon density ($\rho = \rho_n + \rho_p$, where n is used for neutron and p for proton) evaluated at the center-of-mass position $\vec{\mathcal{R}}_{12} = (\vec{R}_1 + \vec{R}_2)/2$ of two interacting nucleons. Equation (4) provides a straightforward representation of the aforementioned density dependence of the effective nucleon-nucleon interaction. It depicts the manner in which the interaction between two nucleons is influenced by the presence of other nucleons within the nucleus. The Skyrme interaction can therefore be understood as a kind of phenomenological G matrix, which takes into account the effect of short-range correlations. As previously outlined, the linear dependence of the density-dependent term in Eq. (4) is achieved with the use of a three-body force. Because we want to include such a density dependence in a more general way, we write this term with a density dependence of the form $\rho^\alpha(\vec{\mathcal{R}}_{12})$, where the power α is a parameter.

It should be noted that following this initial attempt, numerous additional parametrisations of the phenomenological effective nucleon-nucleon interaction of the Skyrme type have been proposed, as has already been mentioned above. To this end, the form of the interaction, as expressed in Eqs. (2) and (4), has been generalised by incorporating exchange parameters, designated as x_j , into

the momentum-dependent terms, which are characterised by strength parameters, denoted as t_1 and t_2 . This encompasses the density-dependent term with the corresponding exchange parameter x_3 . Furthermore, it would be advantageous to have access to a density-dependent term that is not necessarily linear in density. As a result, the correspondence of this term to the three-body interaction of Eq. (3) is lost, but a more flexible density dependence of the effective interaction is gained. As previously discussed, this is the final objective, namely to bridge the gap between a bare inter-nucleon interaction in the vacuum and an effective interaction between nucleons inside the nucleus. One thus writes

$$\begin{aligned}
V_{\text{Sk}}(\vec{R}_1, \vec{R}_2) &= t_0(1 + x_0 P_\sigma) \delta(\vec{R}_{12}) + \frac{t_1}{2}(1 + x_1 P_\sigma) [\delta(\vec{R}_{12}) \vec{k}^2 + \vec{k}'^2 \delta(\vec{R}_{12})] \\
&+ t_2(1 + x_0 P_\sigma) \vec{k}' \cdot \delta(\vec{R}_{12}) \vec{k} + \frac{1}{6} t_3(1 + x_3 P_\sigma) \delta(\vec{R}_{12}) \rho^\alpha(\vec{R}_{12}) \\
&+ iW_0(\vec{\sigma}_1 + \vec{\sigma}_2) \cdot \vec{k}' \times \delta(\vec{R}_{12}) \vec{k}.
\end{aligned} \tag{5}$$

If we consider a nucleus whose ground state is described by a Slater determinant $|\Phi\rangle$ of single-particle states $|\varphi_k\rangle$, we can write down the expectation value E of the Hamiltonian operator ${}^{\text{nuc}}H$ of the nucleus

$${}^{\text{nuc}}H = T_{\text{intr}} + V_{\text{Sk}} + V_{\text{Coul}}, \tag{6}$$

where T_{intr} is the intrinsic kinetic energy, V_{Sk} the density-dependent Skyrme interaction and V_{Coul} the Coulomb interaction, as the integral

$$E = \langle \Phi | {}^{\text{nuc}}H | \Phi \rangle = \int \mathcal{H}(\vec{R}) d^3R \tag{7}$$

of a Hamiltonian density $\mathcal{H}(\vec{R})$ given by [42–44]

$$\begin{aligned}
\mathcal{H}(\vec{R}) &= \left(1 - \frac{1}{A}\right) \frac{\hbar^2}{2m} \tau(\vec{R}) + B_1 \rho^2(\vec{R}) + B_{10} \vec{s}^2(\vec{R}) + B_3 \left(\rho(\vec{R}) \tau(\vec{R}) - \vec{j}^2(\vec{R})\right) \\
&+ B_5 \rho(\vec{R}) \Delta \rho(\vec{R}) + B_{18} \vec{s}(\vec{R}) \cdot \Delta \vec{s}(\vec{R}) + \rho^\alpha(\vec{R}) \left(B_7 \rho^2(\vec{R}) + B_{12} \vec{s}^2(\vec{R})\right) \\
&+ B_9 \rho(\vec{R}) \vec{\nabla} \cdot \vec{J}(\vec{R}) + B_{14} \left(\sum_{\mu, \nu=x, y, z} J_{\mu\nu}^2(\vec{R}) - \vec{s}(\vec{R}) \cdot \vec{T}(\vec{R}) \right) \\
&+ \sum_{q=n, p} \left[B_2 \rho_q^2(\vec{R}) + B_{11} \vec{s}_q^2(\vec{R}) + B_4 \left(\rho_q(\vec{R}) \tau_q(\vec{R}) - \vec{j}_q^2(\vec{R})\right) \right. \\
&\quad + B_6 \rho_q(\vec{R}) \Delta \rho_q(\vec{R}) + B_{19} \vec{s}_q(\vec{R}) \cdot \Delta \vec{s}_q(\vec{R}) + \rho^\alpha(\vec{R}) \left(B_8 \rho_q^2(\vec{R}) + B_{13} \vec{s}_q^2(\vec{R})\right) \\
&\quad \left. + B_9 \rho_q \vec{\nabla} \cdot \vec{J}_q + B_{15} \left(\sum_{\mu, \nu=x, y, z} J_{\mu\nu, q}^2(\vec{R}) - \vec{s}_q(\vec{R}) \cdot \vec{T}_q(\vec{R}) \right) \right],
\end{aligned} \tag{8}$$

where the B_i coefficients are functions of the Skyrme-force parameters t_j and x_j . They have been introduced to simplify the notation and are given in Appendix A of Ref. [45]. The functions of \vec{R} appearing in the right member are called local densities and are defined below. The charge index q refers to a neutron or proton contribution. Quantities without index q correspond to the sum of neutron and proton contributions (e.g. $\rho = \rho_n + \rho_p$, $\tau = \tau_n + \tau_p$, $\vec{s} = \vec{s}_n + \vec{s}_p \dots$). Because the proton mass m_p and the neutron mass m_n are almost equal, one takes $m = (m_n + m_p)/2$ for neutrons and protons in the kinetic energy term. Their actual difference is thus absorbed in the adjustment to experimental data of the interaction parameters. Note that the factor $-\frac{1}{A}$ in the Hamiltonian density, Eq. (8), with $A = N + Z$ the number of nucleons, reflects the one-body contribution to the center-of-mass kinetic energy that has to be subtracted from the total kinetic energy to obtain the intrinsic part only. The two-body contribution to the center-of-mass kinetic energy is usually omitted, as done here, and is thus absorbed in the fit of the interaction parameters.

The various local densities for charge state q appearing in the Hamiltonian density $\mathcal{H}(\vec{R})$ are expressed in terms of the matrix elements in the space-spin-isospin representation $|\vec{R}\sigma q\rangle$ of the one-body density operator $\hat{\varrho}$ associated with the Slater determinant $\Phi(\vec{R})$

$$\varrho(\vec{R}, \sigma, q; \vec{R}', \sigma', q') = \langle \vec{R}' \sigma' q' | \hat{\varrho} | \vec{R} \sigma q \rangle, \quad (9)$$

where $\sigma = \pm 1/2$ is the spin projection on the symmetry axis. The operator $\hat{\varrho}$ can be defined by its spectral decomposition

$$\hat{\varrho} = \sum_k v_k^2 |\varphi_k\rangle \langle \varphi_k|, \quad (10)$$

where the eigenvalue v_k^2 represents the occupation probability of the single-particle state $|\varphi_k\rangle$. For a Slater determinant, one has $v_k^2 = 0$ if the state is empty and $v_k^2 = 1$ if it is occupied. Because single-particle states $|\varphi_k\rangle$ do not mix neutrons and protons, one has

$$\varrho(\vec{R}, \sigma, q; \vec{R}', \sigma', q') = \delta_{q'q} \sum_k v_k^2 \varphi_k^*(\vec{R}', \sigma', q) \varphi_k(\vec{R}, \sigma, q). \quad (11)$$

The Hamiltonian density $\mathcal{H}(\vec{R})$ defined by Eq. (8) involves three local densities that are invariant under time reversal, called “time-even” densities, and three local densities which change sign under time reversal, called “time-odd” densities. The former densities are:

- the nucleon matter density $\rho_q(\vec{R})$

$$\rho_q(\vec{R}) = \sum_{\sigma} \varrho_q(\vec{R}, \sigma, q; \vec{R}, \sigma, q) = \sum_{k, \sigma} v_k^2 |\varphi_k(\vec{R}, \sigma, q)|^2, \quad (12)$$

- the kinetic energy density

$$\tau_q(\vec{R}) = \sum_{\sigma} \vec{\nabla} \cdot \vec{\nabla}' \varrho_q(\vec{R}, \sigma, q; \vec{R}', \sigma, q) |_{\vec{R}'=\vec{R}} = \sum_{k, \sigma} v_k^2 |\vec{\nabla} \varphi_k(\vec{R}, \sigma, q)|^2, \quad (13)$$

where $\vec{\nabla}$ and $\vec{\nabla}'$ denote the gradient operators with respect to the coordinates \vec{R} and \vec{R}' , respectively and,

- the tensor density

$$J_{q, \mu\nu}(\vec{R}) = \frac{1}{2i} \sum_{\sigma, \sigma'} (\partial_{\mu} - \partial'_{\mu}) \varrho_q(\vec{R}, \sigma, q; \vec{R}', \sigma', q) |_{\vec{R}'=\vec{R}} \langle \sigma | \sigma_{\nu} | \sigma' \rangle \quad (14)$$

$$= \frac{1}{2i} \sum_{k, \sigma, \sigma'} v_k^2 \left(\varphi_k^*(\vec{R}, \sigma, q) [\partial_{\mu} \varphi_k(\vec{R}, \sigma', q)] - [\partial_{\mu} \varphi_k^*(\vec{R}, \sigma, q)] \varphi_k(\vec{R}, \sigma', q) \right) \langle \sigma | \sigma_{\nu} | \sigma' \rangle, \quad (15)$$

where μ, ν are cartesian indices. From this density one deduces the so-called spin-orbit density $\vec{J}_q(\vec{R})$, which is the antisymmetric part of $J_{q, \mu\nu}(\vec{R})$ in the sense that its component $J_{q, \lambda}(\vec{R})$ is defined by

$$J_{q, \lambda}(\vec{R}) = \sum_{\mu\nu} \varepsilon_{\lambda\mu\nu} J_{q, \mu\nu}(\vec{R}), \quad (16)$$

where $\varepsilon_{\lambda\mu\nu}$ is the Levi-Civita symbol.

The time-odd local densities are:

- the spin density

$$\begin{aligned} \vec{s}_q(\vec{R}) &= \sum_{\sigma, \sigma'} \varrho_q(\vec{R}, \sigma, q; \vec{R}, \sigma', q) \langle \sigma | \vec{\sigma} | \sigma' \rangle \\ &= \sum_{k, \sigma, \sigma'} v_{q, k}^2 \varphi_k^*(\vec{R}, \sigma, q) \varphi_k(\vec{R}, \sigma', q) \langle \sigma | \vec{\sigma} | \sigma' \rangle, \end{aligned} \quad (17)$$

- the current density

$$\begin{aligned} \vec{j}_q(\vec{R}) &= \frac{1}{2i} \sum_{\sigma} \left[(\vec{\nabla} - \vec{\nabla}') \varrho_q(\vec{R}, \sigma, q; \vec{R}', \sigma, q) \right] |_{\vec{R}'=\vec{R}} \\ &= \frac{1}{2i} \sum_{k, \sigma} v_{q, k}^2 \left[\varphi_k^*(\vec{R}, \sigma, q) \vec{\nabla} \varphi_k(\vec{R}, \sigma, q) - \varphi_k(\vec{R}, \sigma, q) \vec{\nabla} \varphi_k^*(\vec{R}, \sigma, q) \right], \end{aligned} \quad (18)$$

- and the spin-kinetic density

$$\begin{aligned}
\vec{T}_q(\vec{R}) &= \sum_{\sigma, \sigma'} \left[\vec{\nabla} \cdot \vec{\nabla}' \varrho_q(\vec{R}, \sigma, q; \vec{R}', \sigma', q) \right]_{\vec{R}'=\vec{R}} \langle \sigma' | \vec{\sigma} | \sigma \rangle \\
&= \sum_{k, \sigma, \sigma'} v_{q,k}^2 \left[\vec{\nabla} \varphi_k^*(\vec{R}, \sigma, q) \cdot \vec{\nabla} \varphi_k(\vec{R}, \sigma, q) \right] \langle \sigma' | \vec{\sigma} | \sigma \rangle .
\end{aligned} \tag{19}$$

For Slater determinants $\Phi(\vec{R})$ that are invariant under time-reversal symmetry, all time-odd densities vanish. This is the case for the 0^+ ground state of an even-even nucleus. In contrast, these densities do not vanish in the self-consistent solution describing an excited state of an even-even nucleus, or any state of an odd-mass or doubly-odd nucleus.

As mentioned above, by introducing a density-dependent term in the interaction, which is not necessarily linear in ρ , we have given up the correspondence of such a term with a three-body force. However, since the energy of the nucleus can still be written as a functional of a certain number of local densities, and since this will continue to be the case for all subsequent extensions of what we called at the beginning the Skyrme phenomenological effective interaction, we will speak in the following of an energy-density functional (EDF) of the Skyrme type, the concept of an EDF being of course well known from quantum chemistry [46] and materials Science [47] to investigate the electronic structure.

The phenomenological effective interaction or EDF that we are looking for should of course be applicable not only to a given nucleus or group of nuclei in a given region of the nuclid chart, but rather to the whole nuclear chart, with the possible exception of very light nuclear systems, where the concept of mean field loses its meaning and where *ab initio* methods would be much better suited. With this exception, the basic ingredients of an effective nucleon-nucleon interaction, which are rooted in the strong interaction, obviously do not depend on the nuclear system under study. It should then be expected that such a self-consistent approach will be able to accurately describe the ground state properties of a very large number of nuclei, but also to predict some of their excitation and decay modes, such as their stability against fission.

The first really very successful Skyrme-like effective interaction that fulfilled these requirements, namely to adequately describe the binding energies of nuclei along and near the β -stability line, their ground-state radii and multipole moments, but also their low-energy spectroscopy and decay probabilities, was the SIII parametrisation [48]. In the fitting procedure of this interaction, the authors also had in mind to reproduce at the same time some nuclear-matter properties such

as the energy per particle E/A , the nuclear saturation density as it is realised in the center of heavy nuclei, or the nuclear-matter incompressibility, which is essential for the description of the nuclear isoscalar monopole resonance, the so-called *breathing mode*. It should be noted that for ground-state or spectroscopic properties the SIII parametrisation is still one of the most successful Skyrme-type EDFs available today and will be used in the nuclear magnetic-moment studies presented here.

However, it quickly became apparent that essentially all of the early-day EDFs failed to adequately account for the stability against fission of heavy nuclei in the actinide region, and thus produced fission barriers that were far too high. It was the Skyrme SkM* parameterisation [49] which showed that it was indeed possible to obtain a fission barrier height compatible with the experimental data, while retaining the ability to describe the binding energies of nuclei along or near the β stability line. It is only when one moves away from the β valley, i.e. when one explores the regions closer to the neutron and proton drip lines, that these early parameterisations begin to fail.

However, the prospect of radioactive-beam facilities and the search for *super-heavy elements* rapidly motivated the interest in using these EDFs also for nuclei away from the β -stability line, which requires studying more specifically the neutron-proton part of the interaction. This requires an improvement of the available parameterisations with respect to their isospin degrees of freedom. Improving the effective interaction in this direction also opens the way to studying nuclear matter under extreme conditions, such as those encountered in astrophysical applications such as calculations of the structure of neutron stars or their formation by supernova explosions. Work in this direction has been carried out by the Lyon group [50, 51] and has led to EDFs such as SLy4 to describe the spectroscopic properties of nuclei from the β -stability line to the driplines of protons and neutrons. Additional EDF parameterisations (SLy5, SLy6, SLy7) have been proposed to be used when including a spin gradient term or/and taking into account the two-body center-of-mass correction.

Later attempts of improvement included a tensor part in the EDF [44, 52, 53], density-dependent generalisations of the gradient (t_1 and t_2) terms [54], or the introduction of a true 3-body interaction [55]. One should also mention the EDFs of the Bruxelles-Montreal collaboration, which try to include terms simulating correlations beyond the mean field in order to obtain a good reproduction of nuclear masses already at the level of the Hartree-Fock or Hartree-Fock-Bogoliubov approach (see [54, 56, 57] and references therein).

In all these cases the Hamiltonian density $\mathcal{H}(\vec{R})$ of Eq. (7) can always be written as a functional of the local densities, so its space integral is an energy-density functional. The concept of Density Functional Theory (DFT) has, for decades, had enormous success in atomic physics. In atomic DFT, this EDF is used as a corrective term to account for exchange effects and correlations, while the dominant contribution comes from the Coulomb interaction between the electrons and the nucleus and among the electrons themselves, and can in principle be treated exactly. In contrast, in the nuclear case, the dominant contribution comes from the interaction energy of the nucleons among themselves, that one tries to put into some analytical form because the nucleon-nucleon interaction is only known in some approximate way.

Once the Hamiltonian density is known, it can be used to determine, as a function of the force parameters, the expressions for the binding energy per nucleon B/A (where $B = -E > 0$) in symmetric nuclear matter, a hypothetical infinite system with $N = Z \rightarrow \infty$, in the absence of the Coulomb field. From the second derivative of B/A with respect to the Fermi momentum k_f , the incompressibility of nuclear matter is obtained, as explained, e.g., in the original article by Vautherin and Brink [40]. The case of nuclear matter is considered to be approximately realised in heavy nuclei, and the nuclear incompressibility is considered to be a quantity that determines the energy of the isoscalar giant monopole resonance (the so-called breathing mode). In addition, the energy per nucleon should be stationary with respect to variations of the Fermi momentum, giving the nuclear saturation condition $\partial(E/A)/\partial k_f = 0$. The three equations that fix the energy per nucleon, the saturation density and the nuclear incompressibility have traditionally been used to get a first idea of the range of values that some of the Skyrme force parameters can take. In [49] an attempt was made to control the nuclear surface energy, which enters, together with the nuclear incompressibility, in a crucial way in the determination of the height of the fission barriers in heavy (actinide) nuclei.

B. The Skyrme–Hartree–Fock equations

Let us introduce the single-particle two-component Pauli spinor for a nucleon of charge state q $[\varphi_j](\vec{R}, q) = \begin{pmatrix} \varphi_j(\vec{R}, \sigma = 1/2, q) \\ \varphi_j(\vec{R}, \sigma = -1/2, q) \end{pmatrix}$. The Skyrme–Hartree–Fock equations can be obtained from the energy density by requiring that the total energy in Eq. (7) be stationary with respect to the

individual variations of the single-particle states, under the constraint that these are normalised

$$\frac{\delta}{\delta[\varphi_k]^\dagger(\vec{R}, q)} \left[E - \sum_k e_k^{(q)} \int [\varphi_k]^\dagger(\vec{R}, q) [\varphi_k](\vec{R}, q) d^3R \right] = 0, \quad (20)$$

where the single-particle energies $e_k^{(q)}$ play the role of Lagrange parameters. Using the explicit expression in Eq. (8) of the Hamiltonian density appearing in Eq. (7) we find that the single-particle spinors $[\varphi_k](\vec{R}, q)$ must satisfy the following set of equations

$$h_q[\varphi_k](\vec{R}, q) = e_k^{(q)}[\varphi_k](\vec{R}, q), \quad (21)$$

where the Hartree–Fock Hamiltonian, h_q , for charge state q in coordinate representation takes the form [44]

$$\begin{aligned} h_q[\varphi_k](\vec{R}, q) = & -\vec{\nabla} \cdot \left[\left(\frac{\hbar^2}{2m_q^*(\vec{R})} + \vec{C}_q(\vec{R}) \cdot \vec{\sigma} \right) \vec{\nabla}[\varphi_k](\vec{R}, q) \right] \\ & + \left(U_q(\vec{R}) + \delta_{qp} V_{\text{Coul}}(\vec{R}) \right) [\varphi_k](\vec{R}, q) + i \vec{W}_q(\vec{R}) \cdot \left(\vec{\sigma} \times \vec{\nabla}[\varphi_k](\vec{R}, q) \right) \\ & - i \sum_{\mu, \nu=x, y, z} \left[W_{q, \mu\nu}(\vec{R}) \sigma_\nu \partial_\mu [\varphi_k](\vec{R}, q) + \partial_\mu \left(W_{q, \mu\nu}(\vec{R}) \sigma_\nu [\varphi_k](\vec{R}, q) \right) \right] \\ & - i \vec{A}_q(\vec{R}) \cdot \vec{\nabla}[\varphi_k](\vec{R}, q) + \vec{S}_q(\vec{R}) \cdot \vec{\sigma}[\varphi_k](\vec{R}, q). \end{aligned} \quad (22)$$

In Eq. (22) the functions m_q^* , U_q , V_{Coul} , \vec{W}_q and $W_q^{\mu\nu}$ are the effective-mass field, the central-plus-density-dependent scalar field, the Coulomb field, the spin-orbit vector field and the spin-current tensor field, respectively. They are called “time-even” fields because they are invariant with respect to time reversal and are defined by [44]

$$\begin{aligned} U_q(\vec{R}) = & 2 \left(B_1 \rho(\vec{R}) + B_2 \rho_q(\vec{R}) \right) + B_3 \tau(\vec{R}) + B_4 \tau_q(\vec{R}) + 2 \left(B_5 \Delta \rho(\vec{R}) + B_6 \Delta \rho_q(\vec{R}) \right) \\ & + \rho^{\alpha-1}(\vec{R}) \left[(2 + \alpha) B_7 \rho^2(\vec{R}) + B_8 \alpha \left(\rho_n^2(\vec{R}) + \rho_p^2(\vec{R}) + 2 \rho(\vec{R}) \rho_q(\vec{R}) \right) \right] \\ & + B_9 \left(\vec{\nabla} \cdot \vec{J}(\vec{R}) + \vec{\nabla} \cdot \vec{J}_q(\vec{R}) \right) + \delta_{qp} V_{\text{Coul}}(\vec{R}), \end{aligned} \quad (23)$$

$$\frac{\hbar^2}{2m_q^*(\vec{R})} = \frac{\hbar^2}{2m} + B_3 \rho(\vec{R}) + B_4 \rho_q(\vec{R}), \quad (24)$$

$$\vec{W}_q(\vec{R}) = B_9 \left(\vec{\nabla} \rho(\vec{R}) + \vec{\nabla} \rho_q(\vec{R}) \right), \quad (25)$$

$$W_{q, \mu\nu}(\vec{R}) = B_{14} J_{\mu\nu} + B_{15} J_{q, \mu\nu}. \quad (26)$$

The Coulomb field concerning only protons is the sum of direct $V_{\text{Coul}}^{(\text{dir})}$ and exchange $V_{\text{Coul}}^{(\text{exc})}$ contributions

$$V_{\text{Coul}}(\vec{R}) = V_{\text{Coul}}^{(\text{dir})}(\vec{R}) + V_{\text{Coul}}^{(\text{exc})}(\vec{R}). \quad (27)$$

While the direct Coulomb potential can be easily calculated as

$$V_{\text{Coul}}^{(\text{dir})}(\vec{R}) = e^2 \int \frac{\rho_p(\vec{R}')}{|\vec{R} - \vec{R}'|} d^3 R', \quad (28)$$

one generally uses (to avoid very time-consuming calculations) the so-called Slater approximation for the exchange contribution [58]

$$V_{\text{Coul}}^{(\text{exc})}(\vec{R}) = -e^2 \left(\frac{3}{\pi} \rho_p \right)^{1/3}. \quad (29)$$

In contrast, the spin field \vec{S}_q , the current field \vec{A}_q and the spin-gradient field \vec{C}_q appearing in Eq. (22) change their sign under time reversal and are called “time-odd fields”. Their expressions are [44]

$$\begin{aligned} \vec{S}_q(\vec{R}) = & 2(B_{10} + B_{12} \rho^\alpha(\vec{R})) \vec{s}(\vec{R}) + 2(B_{11} + B_{13} \rho^\alpha(\vec{R})) \vec{s}_q(\vec{R}) - B_9 \vec{\nabla} \times (\vec{j}(\vec{R}) + \vec{j}_q(\vec{R})) \\ & - B_{14} \vec{T}(\vec{R}) - B_{15} \vec{T}_q(\vec{R}) + 2(B_{18} \Delta \vec{s}(\vec{R}) + B_{19} \Delta \vec{s}_q(\vec{R})), \end{aligned} \quad (30)$$

$$\vec{A}_q(\vec{R}) = -2(B_3 \vec{j}(\vec{R}) + B_4 \vec{j}_q(\vec{R})) + B_9 \vec{\nabla} \times (\vec{s}(\vec{R}) + \vec{s}_q(\vec{R})), \quad (31)$$

$$\vec{C}_q(\vec{R}) = -B_{14} \vec{s}(\vec{R}) - B_{15} \vec{s}_q(\vec{R}), \quad (32)$$

where the vector Laplacian of \vec{s} is related to the spin-kinetic density through

$$\Delta \vec{s}(\vec{R}) = 2 \vec{T}(\vec{R}) + \sum_{k,q} v_k^2 \left\{ \left(\Delta [\varphi_k]^\dagger(\vec{R}, q) \right) \vec{\sigma} [\varphi_k](\vec{R}, q) + [\varphi_k]^\dagger(\vec{R}, q) \vec{\sigma} \Delta [\varphi_k](\vec{R}, q) \right\}. \quad (33)$$

The Skyrme-Hartree-Fock equations (21) are part of the self-consistent procedure and have to be solved iteratively. Starting with some initial guess for the fields entering this Schrödinger-type equation, one finds a first solution for the wave functions $\varphi_k(\vec{R}, \sigma, q)$ for neutrons and protons, which can then be used to determine the densities Eqs. (9) to (19) and through them the fields Eqs. (23) to (32), which enter the Skyrme-Hartree-Fock equations (21). This procedure is iterated until convergence of some observable quantities is obtained.

C. Cases of spherical and axial symmetries of the nucleus ground-state shape

The calculations described above can be carried out for the ground state of nuclei close to magic (closed-shell) nuclei, such as ^{16}O , ^{40}Ca , ^{48}Ca , ^{90}Zr , ^{132}Sn , ^{208}Pb , by imposing spherical symmetry. These nuclei are the ones mainly considered in the fitting procedures of many parameterisations of the Skyrme EDF. They possess a spherical shape in their ground state and a pure Slater-determinant

wave function is a reasonably good approximation to the exact ground-state wave function. In practice the Skyrme-Hartree-Fock equations (21) can be solved in configuration space as described in Ref. [40]. The nucleon wave functions $\varphi_k(\vec{R}, \sigma, q)$ are then characterised by the principal quantum number n , the orbital angular momentum ℓ , the total angular momentum quantum number j and the magnetic quantum number m_j . From the definition of the local densities, Eqs. (9) to (19), it follows that these depend only on the radial variable R .

However, if the spherical symmetry is broken in the nuclear ground-state shape, neither of these quantum numbers is conserved. If one imposes axial symmetry around the z axis, the projection Ω onto the symmetry z axis of the total angular momentum \vec{j} of a particle evolving in the mean field is conserved. If left-right symmetry (reflection through the xy plane) is additionally imposed, the single-particle states $|\varphi_k\rangle$ are eigenstates of the parity operator π , in addition to being eigenstates of j_z . To solve the Skyrme-Hartree-Fock equations in this case, one can perform an expansion of the wave functions $\varphi_k(\vec{R}, \sigma, q)$ in a suitable basis. Given the retained symmetries, an expansion in the basis of an axially deformed harmonic oscillator (HO) is a reasonable choice [59], as in the pioneering work of Vautherin [41] to solve the Skyrme Hartree-Fock equations for axially deformed nuclei.

Such a basis is necessarily truncated as only a finite number of oscillator shells can be considered. The result of the converged Hartree-Fock cycle will obviously depend on the chosen oscillator parameters. Let us call these N_0 , the number of main oscillator shells included, and ω_z and ω_\perp , the oscillator frequencies in the symmetry and perpendicular directions respectively, which will at the same time determine the nuclear deformation. The optimal choice of this basis will then be the one that minimises the total energy of a given system and thus at the same time determines the nuclear ground state deformation. The number N_0 of HO shells must, of course, be chosen large enough so that the final result of the Skyrme-Hartree-Fock calculation is approximately independent of this choice. For example, a value of $N_0 = 14$, corresponding to 680 HO basis states, is enough for rare-earth nuclei. Instead of ω_z and ω_\perp it is often chosen to consider the following basis parameters [60]

$$\eta = \frac{\omega_\perp}{\omega_z} \quad \text{and} \quad b = \sqrt{\frac{m\omega_0}{\hbar}} \quad \text{with} \quad \omega_0 = (\omega_\perp^2 \omega_z)^{1/3}, \quad (34)$$

or otherwise expressed

$$\omega_z = \omega_0 \eta^{-2/3} \quad \text{and} \quad \omega_\perp = \omega_0 \eta^{1/3}. \quad (35)$$

Note that η is denoted by q in Ref. [45]. If the nuclear deformation does not exhibit axial symmetry, then triaxial symmetry can be imposed and the Skyrme–Hartree–Fock calculations are performed with this symmetry. For the rare earth isotopes (and more particularly the lanthanide family, whose atoms have interesting magnetic properties) we are interested in, almost all the nuclei show some well-developed prolate deformation and axial symmetry can safely be imposed.

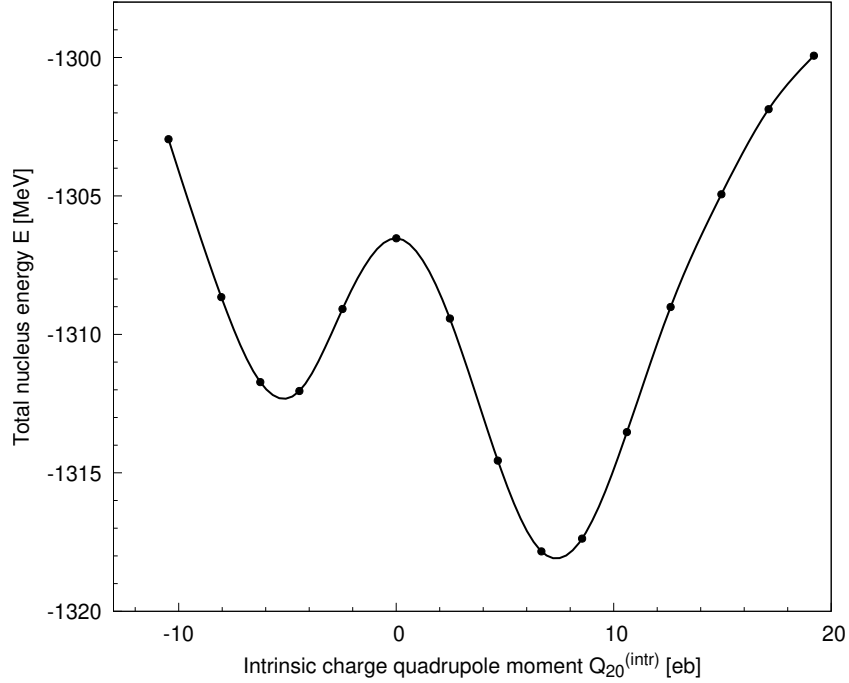


FIG. 1: Energy (in MeV) of the ^{162}Dy nucleus as a function of the constrained expectation value of the intrinsic charge quadrupole moment $Q_{20}^{(\text{intr})}$ in units of ebarn (see subsection II F for its definition). The solid curve is an interpolation through the calculated values marked by filled circles.

If one is only concerned with the ground-state properties of a given nuclear system, the Hartree–Fock iterative cycle will automatically converge to the minimum of the nuclear energy that is realised for such a state (as long as the starting point of the iterative cycle is reasonably chosen). If one is, however, interested in the nuclear deformation energy, i.e. the nuclear energy as a function of deformation, the variational calculation has to be carried out with a constraint on some given multipole moment of the nucleon density. Such constrained Hartree–Fock calculations are usually carried out by imposing the mass quadrupole moment, but higher moments can of course also

be constrained. Figure 1 shows the energy of the nucleus ^{162}Dy as a function of the constrained expectation value of the axial quadrupole moment operator

$$Q_{20} = 2Z^2 - (X^2 + Y^2). \quad (36)$$

Note that this definition yields a value twice as large as that relying on the expression based on spherical harmonics $R^2 Y_{20}(\Theta, \Phi)$, as introduced in Appendix III B. This deformation-energy curve of ^{162}Dy shows two local minima. The lower, ground state configuration, occurs for $Q_{20} > 0$ corresponding a prolate shape, whereas the other configuration occurs for $Q_{20} < 0$ corresponding an oblate isomeric state.

Once the deformation of a given nucleus is well established, the resulting single-particle wave functions $\varphi_k(\vec{R}, \sigma, q)$ can be constructed and used to determine all the local densities, Eqs. (9) to (19). Then one can compute any experimentally accessible quantity such as the nuclear root mean-square (rms) radii or multipole moments (see subsections II F and II G).

D. Including pairing correlations

Pairing correlations are known to affect the nuclear structure in a non-negligible way in all nuclei, with the very rare exception of the regions in the immediate vicinity of closed shells (magic numbers). At the mean-field level, such pairing correlations should, in principle, be taken into account by performing Hartree-Fock-Bogoliubov calculations in which both the mean field and the pairing field are treated equally and determined simultaneously from the same interaction. This is generally done for mean-field calculations with the Gogny force, like in the D1S parameterisation, [37] (see also [61, 62] and references therein for more recent versions of this nucleon-nucleon interaction, such as D1M* and D2). Skyrme EDFs, on the other hand, have generally not been constructed to treat pairing correlations with the same interaction, with the notable exception of the SkP parameterisation of the Skyrme-type EDF [63]. Such correlations have often been taken into account by performing BCS calculations *on top* of the Hartree-Fock iterative cycle using a schematic so-called seniority interaction (constant pairing matrix elements between pairs of time-reversed states, see below). Given a pairing strength G_q , one solves the BCS equations to obtain the Fermi energy λ_q and the gap parameter Δ_q for each nucleon charge state ($q = \{n, p\}$), which then determine the BCS occupation factor v_k^2 for a given single-particle state $|\varphi_k\rangle$. In this framework, all expressions of the local densities Eqs. (12) to (19) remain unchanged and the nuclear energy E

receives an additional contribution E_{pair} called “pair condensation energy” defined by

$$E_{\text{pair}} = \sum_q \sum_{\substack{k>0 \\ l>0}} (\langle \varphi_k \varphi_{\bar{k}} | V_{\text{pair}}^{(q)} | \varphi_l \varphi_{\bar{l}} \rangle - \langle \varphi_k \varphi_{\bar{k}} | V_{\text{pair}}^{(q)} | \varphi_{\bar{l}} \varphi_l \rangle) u_k v_k u_l v_l, \quad (37)$$

where $u_k = \sqrt{1 - v_k^2}$, $|\varphi_{\bar{k}}\rangle$ is the canonically conjugate state of $|\varphi_k\rangle$ (which is associated with the same eigenvalue of $\hat{\varrho}$ as is $|\varphi_k\rangle$ [64]) and V_{pair} is the pairing interaction for the nucleons of charge state q . The summation “ $k > 0$ ” means that one takes only one member of a pair of canonically conjugate states. For the above-mentioned seniority case one has $\langle \varphi_k \varphi_{\bar{k}} | V_{\text{pair}}^{(q)} | \varphi_l \varphi_{\bar{l}} \rangle - \langle \varphi_k \varphi_{\bar{k}} | V_{\text{pair}}^{(q)} | \varphi_{\bar{l}} \varphi_l \rangle = G_q$ (< 0 because V_{pair} is attractive).

The point now is to choose the pairing strength G_q in such a way that the experimental data for quantities such as proton and neutron separation energies are reproduced as well as possible. It turns out that such a choice can indeed be made by defining the pairing strength as

$$G_q = -\frac{G_q^{(0)}}{N_q + 11}, \quad q = \{n, p\}, \quad (38)$$

with $N_n = N$, $N_p = Z$, and where the seniority force strengths $G_n^{(0)}$ and $G_p^{(0)}$ can be chosen for a given mass region as suggested in [45, 65], where also some additional information about the details of the seniority BCS pairing treatment used in our approach can be found.

E. Treatment of odd nuclei

At the heart of the pairing treatment described above is the canonical conjugation as a consequence of the twofold degeneracy of the eigenvalues v_k^2 varying between 0 and 1 of the one-body density operator $\hat{\varrho}$ (the eigenvalues 0 and 1 being highly degenerate). In conjunction with axial symmetry, characterised by the commutation of j_z and $\hat{\varrho}$, we can choose one of the two degenerate eigenstates of $\hat{\varrho}$ as an eigenstate $|\varphi_k\rangle$ of j_z with a positive eigenvalue $\hbar\Omega_k$, while the other eigenstate of $\hat{\varrho}$, denoted $|\varphi_{\bar{k}}\rangle$, is an eigenstate of j_z with the opposite eigenvalue $-\hbar\Omega_k$. According to Herbut and Vujičić [66], there exists an anti-unitary operator P_a , called pairing operator, which maps $|\varphi_k\rangle$ to $|\varphi_{\bar{k}}\rangle$ and is such that $P_a^2 = -1$. When the one-body density operator $\hat{\varrho}_q$ commutes with the time-reversal operator \mathcal{T} , the pairing operator coincides with \mathcal{T} . This happens only in the self-consistent mean-field solution describing the ground state of an even-even nucleus. In this case, one also has a twofold degeneracy of the eigenvalues $e_k^{(q)}$ of the Hartree–Fock Hamiltonian h_q , known as the Kramers degeneracy.

In contrast, when time-reversal symmetry is broken, the Kramer degeneracy no longer holds and the pairing operator differs from the time-reversal operator. This happens in an excited configuration of an even-even nucleus or when the number of neutrons and/or protons is odd. However, at least in axially symmetric Hartree–Fock–BCS calculations, it turns out that for every single-particle state $|\varphi_k\rangle$ with a good quantum number $\Omega_k > 0$ it is always possible to find a state $|\varphi_{\bar{k}}\rangle$ of the same isospin (proton or neutron), which we will call the *conjugate partner* of $|\varphi_k\rangle$, with a good quantum number $-\Omega_k < 0$ and maximising the overlap modulus $|\langle\varphi_{\bar{k}}|(\mathcal{T}|\varphi_k)\rangle|$ with a value close to 1. The states $|\varphi_k\rangle$ and $|\varphi_{\bar{k}}\rangle$ form what we will call a *pseudo pair* [45, 67]. This suggests that the BCS approach presented above can be extended to odd-even or odd-odd nuclei, provided that one works with *pseudo pairs* instead of Cooper pairs, which involve time-reversed states. In a dedicated study [45], it has been shown that the polarisation effect of the even-even core nucleus due to the presence of the unpaired nucleon, which is responsible for the time-reversal symmetry breaking in the odd-mass nucleus, is able to give a fair reproduction of the experimentally measured magnetic dipole moments.

Let us next explain how to calculate properties of an odd-even nucleus using the example of the dysprosium ($Z = 66$) isotopes ^{161}Dy and ^{163}Dy , which have an unpaired neutron hole (^{161}Dy) or neutron particle (^{163}Dy) with respect to the even-even ^{162}Dy nucleus. For this investigation we use a standard Skyrme EDF without any tensor contribution, namely the SIII parametrisation [48], known for its good and well established spectroscopic properties. It is implemented in what is called the *minimal scheme*. In this scheme adapted to SIII, the B_{18} , B_{14} , B_{19} and B_{15} terms of the Hamiltonian density $\mathcal{H}(\vec{R})$ in Eq. (8) are discarded, causing the spin-current tensor field $W_{q,\mu\nu}$ and the spin-gradient field \vec{C}_q defined by Eqs. (26) and (32), respectively, to contribute neither to the Hamiltonian density Eq. (8) nor to the Hartree-Fock Hamiltonian in Eq. (22). This is consistent with the fact that these terms of the spin field \vec{S}_q defined by Eq. (30) have not entered the fitting process of this particular Skyrme EDF (see Ref. [45] for details).

In a first step, we determine the ground state deformation of these nuclei. Assuming that the two odd-mass dysprosium isotopes have the same deformation as the common even-even ^{162}Dy neighbour, one varies the basis parameters b and q of Eq. (34) to minimise the ground-state energy of ^{162}Dy for a fixed value of the number N_0 of HO major shells. Using $N_0 = 14$ turns out to provide a large-enough HO basis (see subsection III.C above). One finds that the optimal parameters are $b = 0.49$ and $\eta = 1.24$. Choosing the pairing strengths $G_n^{(0)} = 16.2$ and $G_p^{(0)} = 15.1$ in Eq. (38)

adjusted to give a good description of the odd-even mass differences in the considered region of the nuclear chart [65], the single-particle spectra of neutrons and protons are then found as shown in Fig. 2.

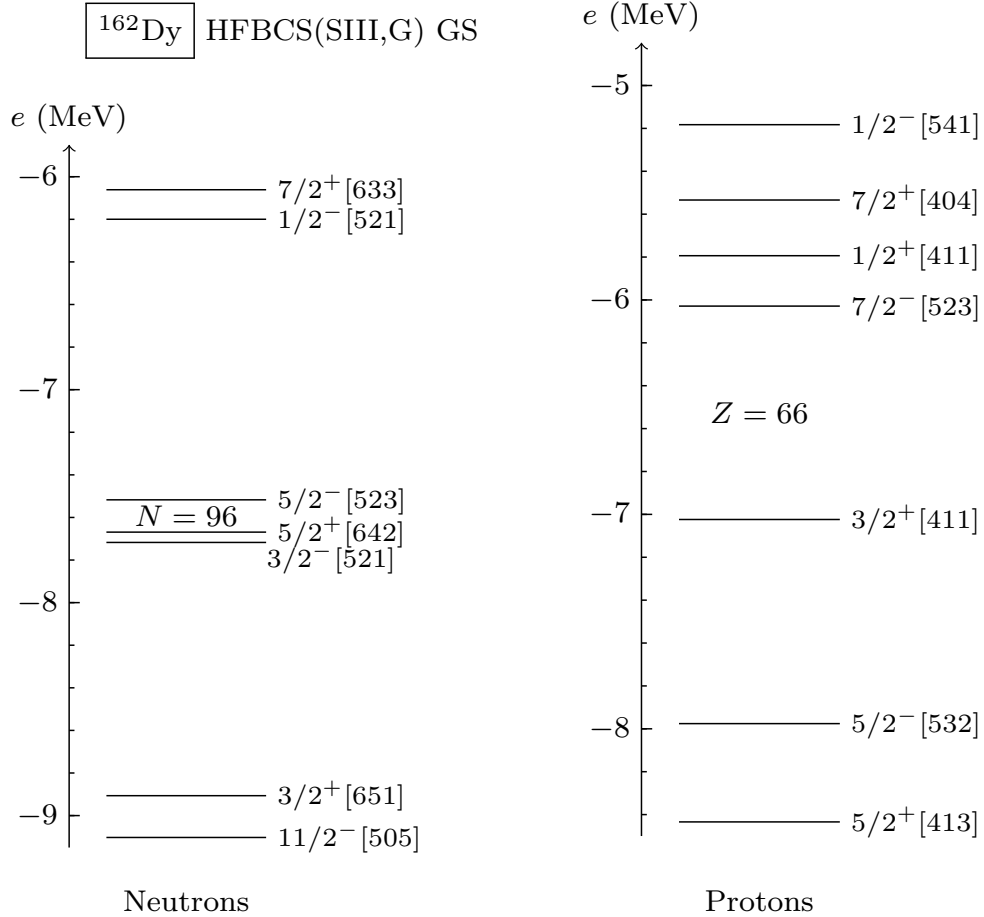


FIG. 2: Single-particle spectra for the ground state of ^{162}Dy near the Fermi level obtained from the HFBCS calculations. Each level is twice degenerate because of the time-reversal symmetry. They are both labeled by the same Nilsson quantum numbers, $\Omega^\pi[Nn_z\Lambda]$, representing the dominant contribution of either single-particle state. $\Omega > 0$ and Λ are the projections onto the symmetry axis of the total and orbital angular momenta, respectively, n_z is the number of oscillator quanta along that axis and N is the total number of oscillator quanta.

Experimentally, the odd dysprosium isotopes ^{161}Dy and ^{163}Dy are found to have ground-state spin and parity $5/2^+$ and $5/2^-$, respectively [68, 69]. In the calculated single-particle neutron spectrum of the ground state of ^{162}Dy in Fig. 2, where the label $N = 96$ corresponds to a filling of

the lowest single-particle twofold degenerate energy levels, we do find single-particle states with these quantum numbers in the immediate vicinity of the neutron Fermi level (corresponding to the last occupied state if pairing is not taken into account). Since the single-particle states are expanded in the harmonic-oscillator basis, the displayed Nilsson quantum numbers $[Nn_z\Lambda]$ are not good quantum numbers but those of the dominant contribution to the given single-particle state. Encouraged by these results, we can then carry out the self-consistent mean-field calculations for the two odd-mass dysprosium isotopes. To do so, we start the Hartree–Fock–BCS iterative process from the Hartree–Fock Hamiltonian and local densities of the converged ^{162}Dy ground-state solution, and impose that the relevant single-particle state identified above with quantum numbers K and π is now blocked with an occupation probability equal to 1, while the *conjugate partner* with quantum numbers $-K$ and π is blocked with a vanishing occupation probability. This is what we call mean-field calculations with self-consistent blocking. This *pseudo pair* of states therefore does not participate in pair excitations and this quenches pairing correlations. The energy spectrum of the first three bandhead states resulting from such calculations is displayed in Fig. 3 and compared with experimental spectra. It can be considered as a good agreement with the experimental data to reproduce such a spectrum within less than 200 keV, even much less in ^{161}Dy .

F. Calculation of the nuclear charge density

As a result of Skyrme–Hartree–Fock–BCS calculations, one obtains all the local densities, defined in Eqs. (12) to (19), from which we get information about the structure of the odd-mass nucleus. In particular, we can calculate observable quantities like the root-mean-square charge radius and the electric quadrupole moment and compare them with experimental data.

In a simple nonrelativistic approach, the nuclear charge density $\rho_c(\vec{R})$ can be obtained by folding the proton charge density $\rho_p(\vec{R})$, which corresponds to point-like particles, with a proton form factor $F(\vec{r})$ that takes into account the charge distribution inside the proton generated by its quark substructure

$$\rho_c(\vec{R}) = \int \rho_p(\vec{R}') F(\vec{R} - \vec{R}') d^3R'. \quad (39)$$

The proton density $\rho_p(\vec{R})$ is defined by Eq. (12) for the charge state $q = p$. The mean-square radius

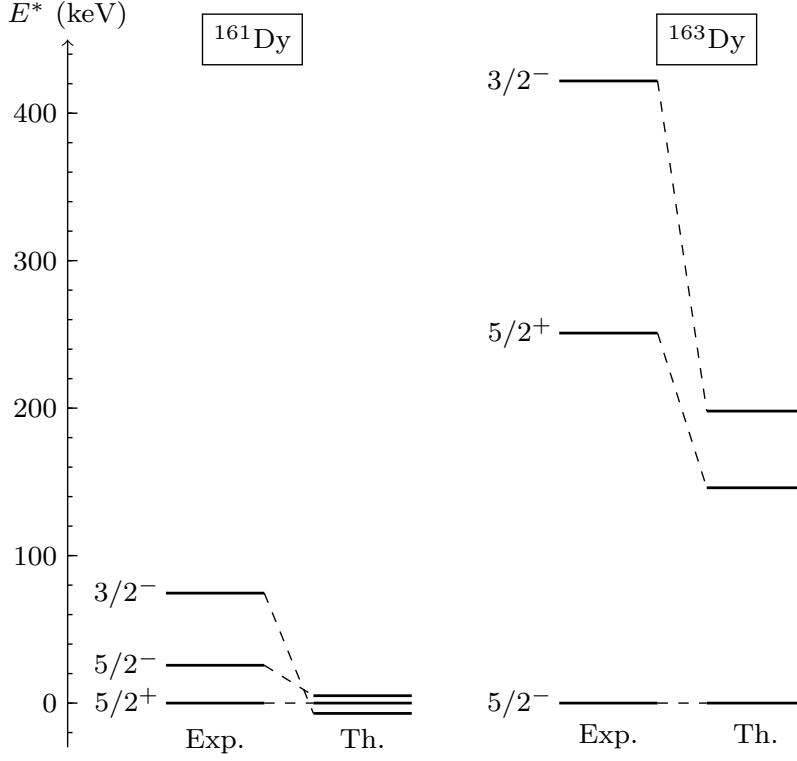


FIG. 3: Excitation energies of the first three bandhead states in ^{161}Dy and ^{163}Dy isotopes. Experimental data (levels labelled “Exp.”) are taken from [68] and [69], respectively. The levels labelled “Th.” correspond to the results of the present Skyrme–HF–BCS calculations using the Skyrme SIII parametrisation and the seniority pairing strengths $G_n = -16.2/(11 + N)$ MeV and $G_p = -15.1/(11 + Z)$ MeV for neutrons and protons, respectively, with $N = 96$ and $Z = 66$ (see text for details).

R_c^2 of the charge density is given by

$$R_c^2 = \frac{\int R^2 \rho_c(\vec{R}) d^3 R}{\int \rho_c(\vec{R}) d^3 R}. \quad (40)$$

With a spherically symmetric Gaussian form factor $F(\vec{R}) = (\sqrt{2\pi} d)^{-3} e^{-R^2/(2d^2)}$ normalised to unity, as in Ref. [70] for instance, the denominator of Eq. (40) becomes

$$\int \rho_c(\vec{R}) d^3 R = \int \rho_p(\vec{R}) d^3 R = Z, \quad (41)$$

and the root mean square radius R_c can be written in the form

$$R_c = \sqrt{\langle R^2 \rangle_p + r_p^2}, \quad (42)$$

where $\langle R^2 \rangle_p$ is the proton contribution to the average value of R^2 considered as a one-body operator

$$\langle R^2 \rangle_p = \frac{\int R^2 \rho_p(\vec{R}) d^3 R}{\int \rho_p(\vec{R}) d^3 R} = \frac{1}{Z} \int R^2 \rho_p(\vec{R}) d^3 R, \quad (43)$$

and r_p^2 is the mean-square radius of the proton

$$r_p^2 = \int R^2 F(\vec{R}) d^3 R = 3 d^2. \quad (44)$$

The CODATA 2022 recommended value of r_p is about 0.84 fm [71].

The intrinsic charge quadrupole moment of the nucleus $Q_{20}^{(\text{intr})}$ is calculated as the proton contribution to the expectation value of the axial quadrupole operator Q_{20} , defined by Eq. (36), in the intrinsic nucleus state $|\Phi\rangle$. It thus takes the integral form:

$$Q_{20}^{(\text{intr})} = e \int \rho_p(\vec{R}) [2 Z^2 - (X^2 + Y^2)] d^3 R \quad (45)$$

Indeed, using the above spherically symmetric proton charge form factor F , one can show that the axial quadrupole moment of the charge density ρ_c is equal to $Q_{20}^{(\text{intr})}$.

Because the intrinsic state $|\Phi\rangle$ and the corresponding quadrupole moment $Q_{20}^{(\text{intr})}$ are defined in the body-fixed frame, while the experimental quadrupole moment as tabulated, e.g., by Stone [72] is measured in the laboratory frame, one needs to perform a change of frame as explained in detail in Appendix VIII A. In a nucleus state of total angular momentum I and projection K on the symmetry axis, the axial quadrupole moment in the laboratory frame, called ‘‘spectroscopic’’ and denoted by $Q_{20}^{(\text{spec})}$, is given by

$$Q_{20}^{(\text{spec})} = \frac{3K^2 - I(I+1)}{(I+1)(2I+3)} Q_{20}^{(\text{intr})}. \quad (46)$$

For the lowest-energy state of a rotational band, identified as the bandhead state, one has $I = K$ (with rare exceptions when $K = 1/2$). In this case the spectroscopic quadrupole moment $Q_{20}^{(\text{spec})}$ becomes

$$Q_{20}^{(\text{spec})} = \frac{K(2K-1)}{(K+1)(2K+3)} Q_{20}^{(\text{intr})} \equiv \mathcal{I}_{\text{intr/spec}}^{E_2} Q_{20}^{(\text{intr})}. \quad (47)$$

The calculated charge rms radius R_{rms} , the nuclear radius $R_N = \sqrt{\frac{5}{3}R_{\text{rms}}^2}$ [73], and the charge quadrupole moment Q_{20} in the body-fixed frame $Q_{20}^{(\text{intr})}$ and in the laboratory frame $Q_{20}^{(\text{spec})}$ together with experimental data are given in Tab. I for the studied Dy isotopes $^{161,163}\text{Dy}$ as well as stable isotopes of odd-proton neighbour elements, namely ^{159}Tb and ^{165}Ho . The numerical parameters used for the latter two nuclei are the same as those reported in subsection II E for the $^{161,163}\text{Dy}$ isotopes. Despite a slight systematic overestimation for R_c and $Q_{20}^{(\text{spec})}$, a good agreement is found for these four prolate-deformed nuclei.

Nucleus	K^π configuration	R_N (fm)		Rms charge radius R_c (fm)		Charge quadrupole moment (eb)		
		Emp.	HFBCS	HFBCS	Exp.	$Q_{20}^{(\text{intr})}$	$Q_{20}^{(\text{spec})}$	Exp. [74]
$^{159}_{65}\text{Tb}$	$3/2^+[411]_p$	6.583	6.704	5.258	5.06(15) [75]	7.345	1.469	+1.432(8)
$^{161}_{66}\text{Dy}$	$5/2^+[411]_n$			5.277	5.197(6) [68]	7.339	2.621	+2.468(29)
	$5/2^- [523]_n$	6.607	6.730	5.278	—	7.348	2.624	2.506
	$3/2^- [521]_n$			5.279	—	7.400	1.480	1.45
$^{163}_{66}\text{Dy}$	$5/2^- [523]_n$	6.631	6.754	5.296	5.2091(25) [69]	7.644	2.730	+2.648(21)
$^{165}_{67}\text{Ho}$	$7/2^- [523]_p$	6.655	6.781	5.318	5.202(31) [76]	7.766	3.624	+3.58(2)

TABLE I: Root mean square charge radius R_c and charge quadrupole moment in the intrinsic frame $Q_{20}^{(\text{intr})}$ and laboratory frame $Q_{20}^{(\text{spec})}$ calculated in the Hartree–Fock–BCS nuclear-structure model compared with experimental data when available for the lowest-three bandhead states of rotational bands of ^{161}Dy isotopes, as well as ground-state values for ^{163}Dy and the stable isotopes of odd-proton neighbour elements ^{159}Tb and ^{165}Ho . In addition, the empirical nuclear radius R_N (see subsection IV A) is given in the third column.

G. Calculation of the magnetic dipole moment

Finally, in this last subsection, we investigate to what extent the presented mean-field approach with self-consistent blocking is able to reproduce the experimental data on the magnetic dipole moments.

Following Schwartz [77], we assume that the response of the nucleus to an external electromagnetic field can be described in a non-relativistic way by means of electric multipole one-body

operators of even rank and magnetic multipole one-body operators of odd rank. As shown by Chemtob in Ref. [78], this means that one can to a good approximation neglect the two-body interaction currents arising from meson exchange between nucleons. Because of the above discussed axial symmetry of the nuclear shape around the z axis of the intrinsic frame, we need only the component along this axis of the magnetic dipole moment one-body operator μ_z as derived by Schwartz [77], namely

$$\mu_z = g^{(\ell)} \ell_z + g^{(s)} s_z, \quad (48)$$

where ℓ_z and $s_z = \frac{\sigma_z}{2}$ are, respectively, the components of the orbital and spin-1/2 angular momentum operators of a nucleon along the z axis, and $g^{(\ell)}$, $g^{(s)}$ are, respectively, the orbital and spin gyromagnetic ratios (or Landé g factors). The values of these constants depend on the isospin of the nucleon and are given in Tab. II. Let $|\Phi\rangle$ denote the normalised many-body state of the odd-

Nucleon	$g^{(\ell)}$	$g^{(s)}$
p	1	+5.585695
n	0	-3.826085

TABLE II: Values with up to six decimal places of the orbital $g^{(\ell)}$ and spin $g^{(s)}$ gyromagnetic ratios (Landé factors) for protons and neutrons entering the magnetic dipole moment through Eq. (48) and implemented in the Skyrme–Hartree–Fock–BCS code used to produce the results of Tab. III.

mass nucleus in the configuration of interest, characterised by the quantum numbers K^π of the blocked nucleon. The expectation value of the magnetic dipole-moment operator μ_z in the intrinsic (body-fixed) frame, $\mu^{(\text{intr})} = \langle \Phi | \mu_z | \Phi \rangle$, defines the intrinsic magnetic dipole moment, denoted μ_0^K in Appendix VIII A. When $|\Phi\rangle$ is obtained as a Skyrme–Hartree–Fock–BCS solution for the specified blocked configuration, $\mu^{(\text{intr})}$ represents the magnetic dipole moment of the nucleus within the Skyrme–Hartree–Fock–BCS framework.

To compare the calculated magnetic dipole moment with experiment, one has, in the same way as for the quadrupole moment discussed in the previous subsection, to perform a change of frame as explained in detail in Appendix VIII A. More precisely, the magnetic dipole moment in the laboratory frame (called spectroscopic) $\mu^{(\text{spec})}$ is proportional to the magnetic dipole moment in the body-fixed frame (called intrinsic) $\mu^{(\text{intr})}$ according to the relation

$$\mu^{(\text{spec})} = \frac{K}{K+1} \mu^{(\text{intr})} \equiv \mathcal{I}_{\text{intr/spec}}^{M_1} \mu^{(\text{intr})}. \quad (49)$$

To obtain this relation, we have applied Eq. (195) to the bandhead state of a rotational band for which the total angular momentum I of the nucleus is equal to its projection K on the symmetry axis, where we have assumed that $K \neq 1/2$.

However, it is known from the unified-model picture of Bohr and Mottelson [79] that a collective contribution g_R (called collective gyromagnetic ratio) has to be added to the contribution $\mu^{(\text{intr})}$ from the intrinsic degrees of freedom. It can be calculated in a microscopic approach relying on a perturbative treatment of the Hamiltonian in a rotating frame according to [80, 81]

$$g_R = \frac{\sum_{k,\ell} \langle \varphi_\ell | \mu_- | \varphi_k \rangle \langle \varphi_k | j_+ | \varphi_\ell \rangle (u_k v_\ell - u_\ell v_k)^2 / (E_k + E_\ell)}{\sum_{k,\ell} \langle \varphi_\ell | j_- | \varphi_k \rangle \langle \varphi_k | j_+ | \varphi_\ell \rangle (u_k v_\ell - u_\ell v_k)^2 / (E_k + E_\ell)}, \quad (50)$$

where the sums run over all states of the HFBCS single-particle spectrum (for each nucleon type) except for blocked state and its pair partner, where u_k and v_k are the usual BCS occupation amplitudes, and E_k are the quasiparticle energies (see Ref. [45] for details). The $j_\pm = j_x \pm ij_y$ are the standard angular momentum ladder operators and the $\mu_\pm = g^{(\ell)} \ell_\pm + g^{(s)} s_\pm$ operators are defined in an analogous way. Setting

$$\mu_{\text{intr}}^{(\text{spec})} = \frac{K}{K+1} \langle \Phi | \mu_z | \Phi \rangle \quad (51)$$

$$\mu_{\text{coll}}^{(\text{spec})} = \frac{K}{K+1} g_R, \quad (52)$$

we therefore have the total magnetic moment in the laboratory frame

$$\mu_{\text{tot}}^{(\text{spec})} = \mu_{\text{intr}}^{(\text{spec})} + \mu_{\text{coll}}^{(\text{spec})}. \quad (53)$$

Table III presents the calculated values of $\mu_{\text{tot}}^{(\text{spec})}$ and its contributions $\mu_{\text{intr}}^{(\text{spec})}$ and $\mu_{\text{coll}}^{(\text{spec})}$ compared with experimental data when available for the lowest three bandhead states of $^{161,163}\text{Dy}$, as well as the ground states of ^{159}Tb and ^{165}Ho .

In almost all cases for which experimental data are available, the calculated intrinsic contribution $\mu_{\text{intr}}^{(\text{spec})}$ (transformed into the laboratory frame) underestimates the measured value and the addition of the collective contribution improves the agreement with experiment. This was already observed in Ref. [45] over a larger sample of nuclei. Keeping in mind the approximations made in these calculations and that the parameters of the Skyrme EDF used here were not fitted to reproduce this observable, we can say that a rather good agreement is reached.

Now we are in a position to establish a relationship between the different contributions (neutron and proton, orbital and spin) to the magnetic moment of a nucleus and the different contributions

Nucleus	K^π configuration	Magnetic dipole moment (μ_N)			
		$\mu_{\text{intr}}^{(\text{spec})}$	$\mu_{\text{coll}}^{(\text{spec})}$	$\mu_{\text{tot}}^{(\text{spec})}$	Exp. [72]
^{159}Tb	$3/2^+[411]_p$	1.886	0.283	+2.169	+2.014(4)
^{161}Dy	$5/2^+[411]_n$	-0.656	0.383	-0.274	-0.480(3)
	$5/2^- [523]_n$	0.647	0.214	+0.861	+0.594(3)
	$3/2^- [521]_n$	-0.639	0.210	-0.428	-0.403(4)
^{163}Dy	$5/2^- [523]_n$	0.663	0.128	+0.791	+0.673(4)
	$5/2^+[411]_p$	-0.638	0.334	-0.304	—
	$3/2^- [521]_p$	-0.644	0.169	-0.475	—
^{165}Ho	$7/2^- [523]_p$	3.946	0.126	+4.072	+4.17(3)

TABLE III: Magnetic dipole moment of the lowest three bandhead states of $^{161,163}\text{Dy}$, as well as of the ground states of ^{159}Tb and ^{165}Ho , calculated within the Skyrme–Hartree–Fock–BCS approach and compared with experimental data when available [72].

to the so-called “convection current density” $\vec{j}_q^{(\ell)}$ and the “spin current density” $\vec{j}_q^{(s)}$. According to Ref. [77], these currents can be expressed respectively in terms of the local densities $\vec{j}_q(\vec{R})$, Eq. (18), and $\vec{s}_q(\vec{R})$, Eq. (17), as

$$\vec{j}_q^{(\ell)}(\vec{R}) = g_q^{(\ell)} \frac{\mu_N}{i} \sum_{k,\sigma} v_k^2 \left(\varphi_k^*(\vec{R}, \sigma, q) \vec{\nabla} \varphi_k(\vec{R}, \sigma, q) - \varphi_k(\vec{R}, \sigma, q) \vec{\nabla} \varphi_k^*(\vec{R}, \sigma, q) \right) \quad (54)$$

$$= 2 g_q^{(\ell)} \mu_N \vec{j}_q(\vec{R}) \quad (55)$$

$$\vec{j}_q^{(s)}(\vec{R}) = g_q^{(s)} \mu_N \vec{\nabla} \times \left(\sum_k v_k^2 [\varphi_k]^\dagger(\vec{R}, q) \frac{\vec{\sigma}}{2} [\varphi_k](\vec{R}, q) \right) \quad (56)$$

$$= \frac{1}{2} g_q^{(s)} \mu_N \vec{\nabla} \times \vec{s}_q(\vec{R}), \quad (57)$$

where $\mu_N = \frac{e\hbar}{2m}$ is the nuclear magneton. Using the expressions of Eqs. (55) and (57), let us

calculate half the integrals $\int \vec{R} \times \vec{j}_q^{(s)}(\vec{R}) d^3 R$ and $\int \vec{R} \times \vec{j}_q^{(\ell)}(\vec{R}) d^3 R$. For the former we have

$$\frac{1}{2} \int \vec{R} \times \vec{j}_q^{(s)}(\vec{R}) d^3 R = \frac{1}{2} g_q^{(s)} \mu_N \int \vec{R} \times \left(\vec{\nabla} \times \vec{s}_q(\vec{R}) \right) d^3 R \quad (58)$$

$$= \frac{1}{4} g_q^{(s)} \mu_N \int \left[\vec{\nabla}(\vec{R} \cdot \vec{s}_q) - \left(R \frac{\partial \vec{s}_q}{\partial R} + \vec{s}_q(\vec{R}) \right) \right] d^3 R \quad (59)$$

$$= -\frac{1}{4} g_q^{(s)} \mu_N \left[\int \left(\int_0^\infty \frac{\partial \vec{s}_q}{\partial R} R^3 dR \right) d\Omega + \int \vec{s}_q(\vec{R}) d^3 R \right] \quad (60)$$

where $\int \dots d\Omega$ denotes the double integral over the two angles of the spherical coordinate system. Because the single-particle states are partially-occupied bound states in the nucleus, their wave functions exponentially decrease to 0 when $R \rightarrow \infty$, and consequently so do all the local densities of the Skyrme energy functional treatment, Eqs. (17) to (19), in particular the spin density $\vec{s}_q(\vec{R})$.

Therefore one can perform an integration by parts over R

$$\int_0^\infty \frac{\partial \vec{s}_q}{\partial R} R^3 dR = -3 \int_0^\infty \vec{s}_q(\vec{R}) R^2 dR ,$$

so that

$$\frac{1}{2} \int \vec{R} \times \vec{j}_q^{(s)}(\vec{R}) d^3 R = \frac{1}{2} g_q^{(s)} \mu_N \int \vec{s}_q(\vec{R}) d^3 R \quad (61)$$

$$= \frac{1}{2} g_q^{(s)} \mu_N \sum_k v_k^2 \int [\varphi_k]^\dagger(\vec{R}, q) \vec{\sigma} [\varphi_k](\vec{R}, q) d^3 R \quad (62)$$

$$= g_q^{(s)} \mu_N \sum_k^{(q)} v_k^2 \langle \varphi_k | \frac{\vec{\sigma}}{2} | \varphi_k \rangle , \quad (63)$$

where $\sum^{(q)} \dots$ means that one sums only over single-particle states having the charge state q .

Finally we obtain, for the z component:

$$\left[\frac{1}{2} \int \vec{R} \times \vec{j}_q^{(s)}(\vec{R}) d^3 R \right]_z = g_q^{(s)} \mu_N \langle \Phi | \frac{\sigma_z}{2} | \Phi \rangle_q , \quad (64)$$

where the notation $\langle \Phi | \dots | \Phi \rangle_q$ refers to the contribution of nucleons of charge state q to the expectation value in the Slater determinant or BCS state $|\Phi\rangle$. Regarding the convection current, setting $\vec{p} = -i\hbar\vec{\nabla}$ one has

$$\frac{1}{2} \int \vec{R} \times \vec{j}_q^{(\ell)}(\vec{R}) d^3 R = g_q^{(\ell)} \mu_N \int \vec{R} \times \vec{j}_q(\vec{R}) d^3 R \quad (65)$$

$$= g_q^{(\ell)} \frac{e}{2m} \int \vec{R} \times \sum_k v_k^2 \text{Re} \left([\varphi_k]^\dagger(\vec{R}, q) \vec{p} [\varphi_k](\vec{R}, q) \right) d^3 R \quad (66)$$

$$= g_q^{(\ell)} \frac{e}{2m} \text{Re} \left[\sum_k v_k^2 \int \left([\varphi_k]^\dagger(\vec{R}, q) (\vec{R} \times \vec{p}) [\varphi_k](\vec{R}, q) \right) d^3 R \right] . \quad (67)$$

Therefore, owing to the Hermitian character of the orbital angular momentum operator $\vec{\ell} = \vec{R} \times \vec{p}$, one obtains for the z component:

$$\left[\frac{1}{2} \int \vec{R} \times \vec{j}_q^{(\ell)}(\vec{R}) d^3 R \right]_z = g_q^{(\ell)} \mu_N \langle \Phi | \ell_z | \Phi \rangle_q. \quad (68)$$

The relations Eq. (64) and Eq. (68) have been tested numerically by computing each member separately: the integrals have been performed by the Gauss-like quadratures discussed above with the same number of mesh points, while the expectation values in the right members have been calculated through matrix elements in the axially-symmetric harmonic-oscillator basis. An agreement up to 10^{-6} has been obtained.

Finally, let us apply the above definitions of the convection and spin currents to the case of axially symmetric Skyrme–HF–BCS solutions. The single-particle wave functions $\varphi_k(\vec{R}, \sigma, q)$, with good quantum number Ω_k , can then be put in the following form, using cylindrical coordinates (ϱ, φ, z) where ϱ is the radial coordinate and φ the polar angle:

$$\varphi_k(\vec{R}, \sigma, q) = \phi_k^{(\sigma)}(\varrho, z) \frac{e^{i\Lambda_\sigma \varphi}}{\sqrt{2\pi}} \quad (69)$$

with $\phi_k^{(\sigma)}(\varrho, z) \in \mathbb{R}$, $\Lambda_\sigma = \Omega_k - \sigma$ ($\sigma = \pm 1/2$) and the normalisation

$$\int \sum_{\sigma=\pm 1/2} |\varphi_k(\vec{R}, \sigma, q)|^2 d^3 R = \int_{-\infty}^{\infty} \left\{ \int_0^{\infty} \left[\left(\phi_k^{(1/2)}(\varrho, z) \right)^2 + \left(\phi_k^{(-1/2)}(\varrho, z) \right)^2 \right] \varrho d\varrho \right\} dz = 1. \quad (70)$$

The local density $\vec{j}_q(\vec{R})$ defined by Eq. (18) can be shown to be orthoradial and independent of the polar angle

$$\vec{j}_q(\vec{R}) = j_{q,\varphi}(\varrho, z) \vec{e}_\varphi \quad (71)$$

where $\vec{e}_\varphi = \frac{\partial \vec{R}}{\partial \varphi} / \left\| \frac{\partial \vec{R}}{\partial \varphi} \right\|$ is the unit vector associated with the polar angle, and the orthoradial component $j_{q,\varphi}(\varrho, z)$ can be expressed as

$$j_{q,\varphi}(\varrho, z) = \frac{1}{2\pi\varrho} \sum_{k,\sigma=\pm 1/2} v_k^2 \Lambda_\sigma \left(\phi_k^{(\sigma)}(\varrho, z) \right)^2. \quad (72)$$

It follows that the convection current density $\vec{j}_q^{(\ell)}$, defined by Eq. (55), becomes

$$\vec{j}_q^{(\ell)}(\vec{R}) = j_{q,\varphi}^{(\ell)}(\varrho, z) \vec{e}_\varphi, \quad (73)$$

where

$$j_{q,\varphi}^{(\ell)}(\varrho, z) = \frac{g_q^{(\ell)} \mu_N}{\pi\varrho} \sum_k v_k^2 \left[\left(\Omega_k - \frac{1}{2} \right) \left(\phi_k^{(1/2)}(\varrho, z) \right)^2 + \left(\Omega_k + \frac{1}{2} \right) \left(\phi_k^{(-1/2)}(\varrho, z) \right)^2 \right]. \quad (74)$$

It vanishes for neutrons since $g_n^{(\ell)} = 0$.

In contrast to the local density $\vec{j}_q(\vec{R})$, the spin density $\vec{s}_q(\vec{R})$ with axial symmetry has a vanishing orthoradial component

$$\vec{s}_q(\vec{R}) = s_{q,\varrho}(\varrho, z) \vec{e}_\varrho + s_{q,z}(\varrho, z) \vec{e}_z, \quad (75)$$

where $\vec{e}_\varrho = \frac{\partial \vec{R}}{\partial \varrho}$ is the unit vector associated with the radial coordinate ϱ . The radial component $s_{q,\varrho}$ and the z -component $s_{q,z}$ are independent of the polar angle φ and are shown to have the following expressions:

$$s_{q,\varrho}(\varrho, z) = \frac{1}{\pi} \sum_k v_k^2 \phi_k^{(1/2)}(\varrho, z) \phi_k^{(-1/2)}(\varrho, z), \quad (76)$$

$$s_{q,z}(\varrho, z) = \frac{1}{2\pi} \sum_k v_k^2 \left[(\phi_k^{(1/2)}(\varrho, z))^2 - (\phi_k^{(-1/2)}(\varrho, z))^2 \right]. \quad (77)$$

It is worth noticing that the radial component of the spin local density results from the mixing of spin projection in the single-particle states $|\varphi_k\rangle$. From the above radial and z components of \vec{s}_q one deduces that the curl of \vec{s}_q is orthoradial,

$$\vec{\nabla} \times \vec{s}_q(\vec{R}) = \left(\frac{\partial s_{q,\varrho}}{\partial z} - \frac{\partial s_{q,z}}{\partial \varrho} \right) \vec{e}_\varphi, \quad (78)$$

and so is the spin current density,

$$\vec{j}_q^{(s)}(\vec{R}) = j_{q,\varphi}^{(s)}(\varrho, z) \vec{e}_\varphi, \quad (79)$$

where $j_{q,\varphi}^{(s)}(\varrho, z)$ is given by

$$j_{q,\varphi}^{(s)}(\varrho, z) = \frac{g_q^{(s)} \mu_N}{2\pi} \sum_k v_k^2 \left[\phi_k^{(1/2)} \left(\frac{\partial \phi_k^{(-1/2)}}{\partial z} - \frac{\partial \phi_k^{(1/2)}}{\partial \varrho} \right) + \phi_k^{(-1/2)} \left(\frac{\partial \phi_k^{(-1/2)}}{\partial \varrho} + \frac{\partial \phi_k^{(1/2)}}{\partial z} \right) \right]. \quad (80)$$

III. ATOMIC-STRUCTURE FRAMEWORK AND NUCLEAR-SIZE EFFECTS IN SPECTROSCOPY

A. Atomic description

The (\vec{j}, ρ) source terms constitute the link between the nucleus and the electrons in the atom. As mentioned in the previous section, we have developed a realistic model that allows us to calculate these quantities on a microscopic scale. As we will see later, from (\vec{j}, ρ) and the Maxwell equations one can obtain the magnetic and electric potentials (\vec{A}, ϕ) that will act on the electrons in the atom.

In this work, if not explicitly mentioned, we will only consider hydrogen-like ions (ions with a single electron) or muonic ions which are atomic hydrogen-like bound states formed by a negatively charged muon of mass $m_\mu \approx 207m_e$ and a nucleus. As the net charge of the nucleus is large ($Z = 66$ in the case of a dysprosium atom), a relativistic description is required since the bound leptons start moving at a significant fraction of the speed of light with non-relativistic velocity $v \sim Z\alpha c$, with α the fine structure constant. We therefore need to solve the stationary Dirac equation for a single electron in the presence of external electric $\phi(\vec{r})$ and magnetic $\vec{A}(\vec{r})$ potentials due to the nucleus, which reads:

$$\begin{aligned} {}^{\text{at}}H\psi &= W\psi \\ &:= \left(c\vec{\alpha} \cdot (\vec{p} + e\vec{A}(\vec{r})) - e\phi(\vec{r})\mathbb{1} + mc^2\beta \right) \psi \\ &:= (T + V + mc^2\beta)\psi, \end{aligned} \quad (81)$$

where $\psi(\vec{r}) = (u(\vec{r}), v(\vec{r}))$ is a four-component bispinor with u and v two-component spinors, $V \equiv -e\phi\mathbb{1}$ with $e > 0$ and $T \equiv c\vec{\alpha} \cdot (\vec{p} + e\vec{A})$ is the kinetic energy operator. $\vec{\alpha}$, β are the Dirac matrices [82] and $\mathbb{1}$ is the 4×4 identity matrix. In the following ${}^{\text{at}}H$ refers to the electronic or atomic Hamiltonian.

For the moment, let's ignore the external magnetic potential ($\vec{A} = \vec{0}$) and assume that the external electric potential is spherically symmetrical, i.e. that $\phi(\vec{r}) = \phi(r)$. The Hamiltonian Eq. (81) commutes with $\vec{\ell}^2$, \vec{s}^2 , \vec{j}^2 , and j_z where $\vec{j} = \vec{\ell} + \vec{s}$ is the total angular momentum operator of the electron or muon. In other words, ℓ , s , j , and m_j are good quantum numbers (in addition to the principal quantum number n). As $s = \frac{1}{2}$ is fixed and does not change, it can be left unspecified. Therefore, energy and angular momentum eigenstates can be written in the form

$$\begin{cases} u_{n\kappa}(\vec{r}) = g_{n\kappa}(r)\chi_\kappa^{m_j}(\Omega) \\ v_{n\kappa}(\vec{r}) = if_{n\kappa}(r)\chi_{-\kappa}^{m_j}(\Omega), \end{cases} \quad (82)$$

where χ are the spin spherical harmonics defined by

$$\chi_\kappa^{m_j}(\Omega) = \begin{pmatrix} \langle \ell, \frac{1}{2}, m_j - \frac{1}{2}, +\frac{1}{2} | j, m_j \rangle Y_{\ell, m_j - \frac{1}{2}}(\Omega) \\ \langle \ell, \frac{1}{2}, m_j + \frac{1}{2}, -\frac{1}{2} | j, m_j \rangle Y_{\ell, m_j + \frac{1}{2}}(\Omega) \end{pmatrix}, \quad (83)$$

which satisfy the orthonormalisation conditions

$$\int \chi_\kappa^{m_j*}(\Omega)\chi_{\kappa'}^{m_{j'}}(\Omega)d\Omega = \delta_{\kappa\kappa'}\delta_{m_j m_{j'}}. \quad (84)$$

The radial functions $f_{n\kappa}(r)$ and $g_{n\kappa}(r)$ are solutions of the differential equations

$$\begin{cases} \frac{dg_{n\kappa}}{dr} = -\frac{\kappa+1}{r}g_{n\kappa} + \frac{1}{c\hbar}(W - V + mc^2)f_{n\kappa} \\ \frac{df_{n\kappa}}{dr} = +\frac{\kappa-1}{r}f_{n\kappa} - \frac{1}{c\hbar}(W - V - mc^2)g_{n\kappa} \end{cases} \quad (85)$$

with $m = m_e$ for an electron and $m = m_\mu$ for a muon. By definition we have $P_{n\kappa} \equiv rg_{n\kappa}$ (large component) and $Q_{n\kappa} \equiv rf_{n\kappa}$ (small component) that satisfy the normalisation condition $\int_0^\infty (P_{n\kappa}^2(r) + Q_{n\kappa}^2(r)) dr = 1$. The solutions of the radial Dirac equation are labeled by the quantum numbers $n \in \mathbb{N}^*$ (principal quantum number) and $\kappa \in \mathbb{Z}^*$. Alternatively, they may be labeled by the triplet $n\ell_j$, where $\ell \in \mathbb{N}$ is the orbital angular momentum and $j = \ell \pm \frac{1}{2}$ is the total angular momentum. κ is determined by $\kappa = -\ell - 1 = -(j + \frac{1}{2})$ for $j = \ell + \frac{1}{2}$ and $\kappa = \ell = +(j + \frac{1}{2})$ for $j = \ell - \frac{1}{2}$.

B. Multipole expansions of the electric and magnetic potentials

In the following we will denote $\vec{R} = (R, \Theta, \Phi)$ and $\vec{r} = (r, \theta, \phi)$ as the spherical coordinates of the nucleus and the electron respectively and $C_q^{(k)}(\theta, \phi)$ designates the normalised spherical harmonics defined by $C_q^{(k)}(\theta, \phi) \equiv \sqrt{\frac{4\pi}{(2k+1)}}Y_{k,q}(\theta, \phi)$ and $\Omega \equiv (\theta, \phi)$. In the following, for convenience, in relation to the previous section, we will use different symbols to designate electric and magnetic multipole moments: $Q_{20}^{(\text{intr})} \equiv 2Q_0^{(2)}$ and $\mu_{\text{tot}}^{(\text{intr})} \equiv M_z^{(1)}$.

1. Electric Potential

The electric potential generated by the nucleus through its charge density ($\rho(\vec{R}) = e\rho_p(\vec{R})$ with ρ_p the proton density given by Eq. (12)). Note that, in the following discussion, the symbol ρ denotes the nuclear charge density and should not be confused with the total nucleon density used in the previous section. The potential in which the electron moves then has the form

$$\phi(\vec{r}) = \frac{1}{4\pi\epsilon_0} \int \frac{\rho(\vec{R})}{|\vec{r} - \vec{R}|} d^3R, \quad (86)$$

and ϕ is solution of the Poisson equation $\Delta\phi = -\frac{\rho}{\epsilon_0}$. By using the usual multipolar expansion

$$\frac{1}{|\vec{r} - \vec{R}|} = \sum_{k=0}^{\infty} \sum_{\substack{r < R \\ r > R}} \frac{r^k}{r^{k+1}} \sum_{q=-k}^k (-1)^q C_{-q}^{(k)}(\Theta, \Phi) C_q^{(k)}(\theta, \phi), \quad (87)$$

the electric potential takes the form

$$\begin{aligned}
\phi(\vec{r}) &= \frac{1}{4\pi\epsilon_0} \sum_{k=0}^{\infty} \frac{1}{r^{k+1}} \sum_{q=-k}^k (-1)^q C_q^{(k)}(\theta, \phi) \text{in} \mathcal{Q}_q^{(k)}(r) \\
&+ \frac{1}{4\pi\epsilon_0} \sum_{k=0}^{\infty} r^k \sum_{q=-k}^k (-1)^q C_q^{(k)}(\theta, \phi) \text{ex} \mathcal{Q}_q^{(k)}(r) \\
&= \sum_{k=0}^{\infty} \sum_{q=-k}^k \phi_{k,q}(r) C_q^{(k)}(\theta, \phi) \\
&= \sum_{k=0}^{\infty} \phi_k(\vec{r}) ,
\end{aligned} \tag{88}$$

where we have defined

$$\text{in} \mathcal{Q}_q^{(k)}(r) \equiv \int_{R=0}^r \rho(\vec{R}) R^k C_q^{(k)}(\Theta, \Phi) d^3 R \tag{89}$$

and

$$\text{ex} \mathcal{Q}_q^{(k)}(r) \equiv \int_{R=r}^{\infty} \frac{\rho(\vec{R})}{R^{k+1}} C_q^{(k)}(\Theta, \Phi) d^3 R . \tag{90}$$

Let us recall the usual definition of the multipole electric moment

$$\mathcal{Q}_q^{(k)} \equiv \int_{R=0}^{\infty} \rho(\vec{R}) R^k C_q^{(k)}(\Theta, \Phi) d^3 R . \tag{91}$$

It is worth noting that if the electronic wave function does not penetrate the nucleus (i.e. $R \ll r$), one has $\text{in} \mathcal{Q}_q^{(k)}(r) = \mathcal{Q}_q^{(k)} \forall r$ since $\mathcal{Q}_q^{(k)} = \lim_{r \rightarrow +\infty} \text{in} \mathcal{Q}_q^{(k)}(r)$.

a. Electric monopole The electric monopole term is spherically symmetric, and takes the form

$$\begin{aligned}
\phi_0(\vec{r}) &= \phi_0(r) = \phi_{0,0}(r) = \frac{1}{4\pi\epsilon_0} C_0^{(0)}(\theta, \phi) \left(\frac{\text{in} \mathcal{Q}_0^{(0)}(r)}{r} + \text{ex} \mathcal{Q}_0^{(0)}(r) \right) \\
&= \frac{1}{4\pi\epsilon_0} \left(\frac{\text{in} \mathcal{Q}_0^{(0)}(r)}{r} + \text{ex} \mathcal{Q}_0^{(0)}(r) \right) .
\end{aligned} \tag{92}$$

In the non-penetrating case we would have had

$$\phi_0(\vec{r}) = \phi_0(r) = \phi_{0,0}(r) = \frac{1}{4\pi\epsilon_0} \frac{\mathcal{Q}_0^{(0)}}{r} , \tag{93}$$

where $\mathcal{Q}_0^{(0)}$ is simply the total charge Ze of the nucleus.

To assess the impact of a microscopic calculation of the nuclear charge density on the hyperfine interactions, we will compare the results obtained with those derived from a semi-empirical

description of the density, which is the well-known Fermi distribution. The latter is computed as follows

$$\rho(R) = \frac{\rho_0}{1 + \exp\left(\frac{R-\tilde{c}}{\tilde{a}}\right)}, \quad (94)$$

with

$$\rho_0 = \frac{3}{4\pi\tilde{c}^3 \left(1 + \left(\frac{\pi\tilde{a}}{\tilde{c}}\right)^2\right)}. \quad (95)$$

The parameters \tilde{a} , \tilde{c} have been taken from [73].

b. Electric quadrupole Due to the symmetry of the nucleus, the only non-zero component of the quadrupole tensors is $q = 0$ (see Sec. II, and we recall $Q_{20}^{(\text{intr})} \equiv 2Q_0^{(2)}$). The electric quadrupole term of the electric potential is

$$\phi_2(\vec{r}) = \frac{1}{4\pi\epsilon_0} C_0^{(2)}(\theta, \phi) \left(\frac{\text{in} Q_0^{(2)}(r)}{r^3} + r^2 \text{ex} Q_0^{(2)}(r) \right). \quad (96)$$

Again, without penetration, we have

$$\begin{aligned} \phi_2(\vec{r}) &= \frac{C_0^{(2)}(\theta, \phi)}{4\pi\epsilon_0} \frac{Q_0^{(2)}}{r^3} \\ &= \phi_{2,0}(r) C_0^{(2)}(\theta, \phi). \end{aligned} \quad (97)$$

It is important to note that this potential is no longer spherically symmetric.

2. Magnetic potential

The magnetic field produced by the nucleus and which acts on the electrons of the atom through the potential vector $\vec{A}(\vec{r})$ in the Dirac equation (81) is fully characterised by the nuclear current density $\vec{j}(\vec{R})$ and is given by Eqs. (55) and (57).

In what follows, we give the most important expressions that we will need in the following and refer the reader to the appendix subsection VIII B for the demonstrations that are more complex and technical than for the electric potential.

From Biot and Savart's law, which gives the expression for the magnetic field \vec{B} as a function of the current density \vec{j} , and using the definition of the vector potential $\vec{B} = \vec{\nabla} \wedge \vec{A}$ and the Coulomb gauge ($\vec{\nabla} \cdot \vec{A} = 0$), we obtain the magnetic equivalent of the scalar potential, Eq. (86),

$$\vec{A}(\vec{r}) = \frac{\mu_0}{4\pi} \int \frac{\vec{j}(\vec{R})}{|\vec{r} - \vec{R}|} d^3R. \quad (98)$$

As with the scalar potential, we can perform a multipole expansion of \vec{A} which is expressed as

$$\begin{aligned} \vec{A}(\vec{r}) &= \frac{\mu_0}{4\pi} \sum_{k=0}^{\infty} \sum_{q=-k}^k (-1)^q \frac{(-i)}{\hbar k} \left[\vec{L}C_q^{(k)}(\theta, \phi) \right] \frac{\text{in} M_{-q}^{(k)}(r)}{r^{k+1}} \\ &+ \frac{\mu_0}{4\pi} \sum_{k=0}^{\infty} \sum_{q=-k}^k (-1)^q \frac{(-i)}{\hbar k} \left[\vec{L}C_q^{(k)}(\theta, \phi) \right] \text{ex} M_{-q}^{(k)}(r) r^k, \end{aligned} \quad (99)$$

with

$$\text{in} M_q^{(k)}(r) \equiv -\frac{i}{\hbar(k+1)} \int_{R=0}^r \left[\vec{L}C_q^{(k)}(\Theta, \Phi) \right] \cdot \vec{j}(\vec{R}) R^k d^3 R, \quad (100)$$

and

$$\text{ex} M_q^{(k)}(r) \equiv -\frac{i}{\hbar(k+1)} \int_{R=r}^{\infty} \left[\vec{L}C_q^{(k)}(\Theta, \Phi) \right] \cdot \vec{j}(\vec{R}) \frac{1}{R^{k+1}} d^3 R. \quad (101)$$

In the above expressions, we have defined $\vec{L} \equiv -i\hbar\vec{R} \wedge \vec{\nabla}$. The usual definition of magnetic multipole moments is as follows

$$M_q^{(k)} \equiv -\frac{i}{\hbar(k+1)} \int_{R=0}^{\infty} \left[\vec{L}C_q^{(k)}(\Theta, \Phi) \right] \cdot \vec{j}(\vec{R}) R^k d^3 R = \text{in} M_q^{(k)}(r \rightarrow \infty), \quad (102)$$

and, again, corresponds to the case without penetration of the electron wave function into the nucleus (i.e. $R \ll r$). For the dipole term, which is the only magnetic multipole considered in this work, we obtain the following expressions (see Appendix VIII B 2)

$$\vec{A}(\vec{r}) = \frac{\mu_0}{4\pi} \frac{\text{in} \vec{M}^{(1)}(r) \wedge \vec{r}}{r^3} + \frac{\mu_0}{4\pi} \left(\text{ex} \vec{M}^{(1)}(r) \wedge \vec{r} \right), \quad (103)$$

with

$$\text{in} \vec{M}^{(1)}(r) = \frac{1}{2} \int_{R=0}^r \vec{R} \wedge \vec{j}(\vec{R}) d^3 R \quad (104)$$

and

$$\text{ex} \vec{M}^{(1)}(r) = \frac{1}{2} \int_{R=r}^{\infty} \frac{\vec{R} \wedge \vec{j}(\vec{R})}{R^3} d^3 R. \quad (105)$$

In the situation where the penetration of the electron wave function inside the nucleus is neglected, we obtain the well-known formula

$$\vec{A}(\vec{r}) = \frac{\mu_0}{4\pi} \frac{\text{in} \vec{M}^{(1)} \wedge \vec{r}}{r^3}, \quad (106)$$

with

$$\vec{M}^{(1)} = \frac{1}{2} \int_{R=0}^{\infty} \vec{R} \wedge \vec{j}(\vec{R}) d^3 R. \quad (107)$$

C. Hyperfine interactions

The unperturbed electron Hamiltonian takes into account the monopole term of the scalar potential Eq. (96) that has spherical symmetry. The following terms of the multipole expansions of ϕ and \vec{A} , i.e. the quadrupole term of the scalar potential and the dipole term of the vector potential, contribute very little and can therefore be treated using first-order stationary perturbation theory. The perturbation Hamiltonian reads as

$$\begin{aligned} {}^{\text{at}}H_{\text{hf}} &= -e\phi_2(\vec{r}) + ec\vec{\alpha} \cdot \vec{A}(\vec{r}) \\ &\equiv {}^{\text{at}}H_{\text{hf,quad}} + {}^{\text{at}}H_{\text{hf,dip}} . \end{aligned} \quad (108)$$

Recall that the total angular momentum of the nucleus is generally represented by the symbol I and is called the "nuclear spin". For electrons in atoms, we clearly distinguish between the electron spin, \vec{S} , and the electron orbital moment, \vec{L} , and combine them to obtain the total angular momentum, \vec{J} . However, nuclei often act as a single entity with their own angular momentum \vec{I} . Each nuclear spin has a nuclear magnetic moment. This produces magnetic interactions with its surroundings, leading to the magnetic hyperfine interaction. As detailed in Appendix VIII C 1, for an atom or ion with nuclear spin I and electronic total angular momentum J , the value of the splitting of the electronic energy level, which is characterised by quantum numbers $n\kappa$, is, to first order in ${}^{\text{at}}H_{\text{hf}}$ given by

$$\begin{aligned} W_F &= \langle n\kappa F M_F | {}^{\text{at}}H_{\text{hf}} | n\kappa F M_F \rangle \\ &= \langle n\kappa F M_F | {}^{\text{at}}H_{\text{hf,dip}} | n\kappa F M_F \rangle + \langle n\kappa F M_F | {}^{\text{at}}H_{\text{hf,quad}} | n\kappa F M_F \rangle \\ &= \frac{1}{2}a\tilde{K} + b\frac{\frac{3}{2}\tilde{K}(\tilde{K} + 1) - 2I(I + 1)J(J + 1)}{2I(2I - 1)2J(2J - 1)} , \end{aligned} \quad (109)$$

where $\tilde{K} = F(F + 1) - I(I + 1) - J(J + 1)$, a and b are the magnetic dipole and electric quadrupole structure constants. F is the quantum number of the total angular momentum $\vec{F} = \vec{I} + \vec{J}$.

To illustrate this, let us mention the work [83] that measured the transition between the $F = 4$ and $F = 3$ levels of the $1s_{1/2}$ ground state of the hydrogen-like ion $^{165}\text{Ho}^{66+}$.

1. Magnetic dipole hyperfine structure constant

The first term in Eq. (109) is the magnetic dipole hyperfine interaction, which is responsible for the splitting of one fine structure atomic energy level into a hyperfine multiplet labeled by F .

Consequently, if no other interaction influences the hyperfine levels, and considering the magnetic dipole interaction to be weak compared to the other terms of the electronic Hamiltonian, the energy interval between adjacent F sub-levels is $E_F - E_{F-1} = aF$. This is the so-called Landé interval rule. As a result, the hyperfine levels are equidistant in energy. We will see later that if we include the quadrupole term this property is no longer true. To illustrate the importance of the non-equidistance of hyperfine energy levels—which makes it possible to address individual hyperfine transitions—one can cite, in the field of quantum computing, the implementation of quantum algorithms in molecular complexes [10].

Following the multipole expansion of the magnetic vector potential of the nucleus and its influence on the electrons, we obtain the magnetic dipole hyperfine constant a of electrons, with quantum numbers n and κ , to be equal to (see Appendix VIII C 1)

$$a(\vec{j}, \rho) = \mathcal{U}(\kappa, j) \int_0^\infty \left(\frac{1}{r^2} \int_{R=0}^r [\vec{R} \wedge \vec{j}(\vec{R})]_z d^3R + r \int_{R=r}^\infty \frac{[\vec{R} \wedge \vec{j}(\vec{R})]_z}{R^3} d^3R \right) P_{n\kappa}(r) Q_{n\kappa}(r) dr, \quad (110)$$

where \vec{R} are the coordinates of nuclear current and charge distribution, while r is the electronic radial coordinate. $P_{n\kappa}(r)$ and $Q_{n\kappa}(r)$ are, respectively, the large and small radial components of the Dirac wavefunction of the electrons. $\vec{j}(\vec{R})$ is the electric current distribution of the nucleus, as defined in Eq. (111). The subscript z on the vector product terms indicates that only the z component needs to be considered, as it corresponds to the quantisation axis common to nucleons and electrons. Finally, $\mathcal{U}(\kappa, j)$ is a multiplicative factor depending only on the angular part of the electronic many-body wavefunction. For configurations with two or more electrons it requires the use of group theoretical tools to compute. For ions with one single electron or muon (as studied in this work) we have $\mathcal{U}(\kappa, j) \propto \frac{\kappa}{j(j+1)}$ (see Appendix VIII C 1). The dependence of a on the charge distribution ρ is indirect, via the calculation of $P_{n\kappa}$ and $Q_{n\kappa}$. Indeed, $P_{n\kappa}$ and $Q_{n\kappa}$ are solutions of the Dirac equation containing the electric monopole potential produced by ρ (see ?? III B 1 a). Evidently, the accuracy of the value of a depends on the quality of the nuclear model used to evaluate \vec{j} and ρ .

The calculation of (\vec{j}, ρ) based on a microscopic description of the nucleus has been described in detail in Sec. II. As a reminder we have

$$\vec{j}(\vec{R}) = \vec{j}_p^{(l)}(\vec{R}) + \vec{j}_n^{(l)}(\vec{R}) + \vec{j}_p^{(s)}(\vec{R}) + \vec{j}_n^{(s)}(\vec{R}), \quad (111)$$

where $\vec{j}_{p,n}^{(l,s)}$ are the convection (or orbital) and spin currents of protons and neutrons respectively.

Note that only the proton current as an electric charge current will produce an orbital magnetic moment.

If we assume a point magnetic dipole (i.e. no penetration inside the nucleus can occur and hereafter referred to as “pd”), we have the following simplifications ($\forall r \gg R$)

$$a_{\text{pd}} = \mathcal{U}(\kappa, j) M_z^{(1),(\text{spec})} \left[\int_0^\infty \frac{P_{n\kappa}(r) Q_{n\kappa}(r)}{r^2} dr \right]. \quad (112)$$

If we add up all the constants, we obtain for a one-electron system

$$a_{\text{pd}} = -\frac{e}{4\pi\epsilon_0} \frac{1}{c} \frac{\mu_N}{a_0^2} \frac{\kappa}{j(j+1)} \frac{1}{I} M_z^{(1),(\text{spec})} \left[\int_0^\infty \frac{P_{n\kappa}(r) Q_{n\kappa}(r)}{r^2} dr \right]. \quad (113)$$

In the above expressions $M_z^{(1),(\text{spec})}$ is expressed in units of μ_N and $\left[\int_0^\infty \frac{P_{n\kappa}(r) Q_{n\kappa}(r)}{r^2} dr \right]$ in units of a_0^{-2} . Moreover, $\mathcal{I}_{\text{intr}/\text{spec}}^{M_1}$ is the conversion factor from intrinsic nuclear dipole moment to nuclear dipole moment measured in the laboratory (see Sec. II and Appendix VIII A [100].) leading to the definition of the spectroscopic nuclear dipole moment $M_z^{(1),(\text{spec})} \equiv \mathcal{I}_{\text{intr}/\text{spec}}^{M_1} M_z^{(1)}$.

In the extreme case of a hydrogen atom we have $M_z^{(1)} = g_p^{(s)} I \mu_N$ and $\mathcal{I}_{\text{intr}/\text{spec}}^{M_1} = 1$ with $I = 1/2$, leading to [84]

$$a_{\text{pd}} = -g_p^{(s)} \frac{\kappa}{j(j+1)} \left[\int_0^\infty \frac{P_{n\kappa}(r) Q_{n\kappa}(r)}{r^2} dr \right] \times 13074.7 \text{ MHz}. \quad (114)$$

Furthermore, any change in the radial (spherically-averaged) charge distribution of the nucleus, will change the radial components $P_{n\kappa}(r)$ and $Q_{n\kappa}(r)$ of the electrons. Therefore $P_{n\kappa}(r)$ and $Q_{n\kappa}(r)$ are not the same for a point (charge) nucleus and a finite size one. We call the radial components of the wavefunctions under the consideration of a point nucleus $P_{n\kappa}^0$ and $Q_{n\kappa}^0$. It allows us to define the magnetic dipole hyperfine constant for a point-charge nucleus,

$$a_{\text{point}} = \mathcal{U}(\kappa, j) M_z^{(1),(\text{spec})} \int_0^\infty \frac{P_{n\kappa}^0(r) Q_{n\kappa}^0(r)}{r^2} dr. \quad (115)$$

2. Electric quadrupole hyperfine structure constant

The second term in the expression Eq. (109) is obtained by evaluating the matrix element $\langle n\kappa F M_F |^{\text{at}} H_{\text{hf,quad}} | n\kappa F M_F \rangle$. After fairly lengthy calculations, which are detailed in the appendix subsection VIII C 2, we obtain for the electric quadrupole structure constant

$$b = 2 \frac{e}{4\pi\epsilon_0} \left(\frac{2j-1}{2j+2} \right) \mathcal{I}_{\text{intr}/\text{spec}}^{E_2} \times \int_0^\infty \left(\frac{1}{r^3} \int_{R=0}^r \rho(\vec{R}) R^2 C_0^{(2)}(\Theta, \Phi) d^3 R + r^2 \int_{R=r}^\infty \frac{\rho(\vec{R})}{R^3} C_0^{(2)}(\Theta, \Phi) d^3 R \right) (P_{n\kappa}^2(r) + Q_{n\kappa}^2(r)) dr, \quad (116)$$

where $\mathcal{I}_{\text{intr/spec}}^{E_2}$ is the conversion factor from intrinsic nuclear quadrupole moment to nuclear quadrupole moment measured in the laboratory (see Sec. II and Appendix VIII A [101]).

If we assume a point electric quadrupole (i.e. no penetration inside the nucleus can occur and hereafter referred to as ‘‘pq’’), we have the following simplifications

$$b_{\text{pq}} = 2 \frac{e}{4\pi\epsilon_0} \left(\frac{2j-1}{2j+2} \right) \mathcal{I}_{\text{intr/spec}}^{E_2} \int_{R=0}^{\infty} \rho(\vec{R}) R^2 C_0^{(2)}(\Theta, \Phi) d^3R \int_0^{\infty} \frac{(P_{n\kappa}^2(r) + Q_{n\kappa}^2(r))}{r^3} dr \quad (117)$$

$$= 2Q_0^{(2),(\text{spec})} \left(\frac{2j-1}{2j+2} \right) \left[\int_0^{\infty} \frac{(P_{n\kappa}^2(r) + Q_{n\kappa}^2(r))}{r^3} dr \right] \times 234.965 \text{ MHz} , \quad (118)$$

where the intrinsic quadrupole moment $Q_0^{(2)} \equiv \int_{R=0}^{\infty} \rho(\vec{R}) R^2 C_0^{(2)}(\Theta, \Phi) d^3R$ is expressed in terms of $|e| \times \text{barn}$ and $\left[\int_0^{\infty} \frac{(P_{n\kappa}^2(r) + Q_{n\kappa}^2(r))}{r^3} dr \right]$ in terms of a_0^{-3} . Let us stress that this term cancels out for orbitals with $j = \frac{1}{2}$ i.e. $ns_{\frac{1}{2}}, n'p_{\frac{1}{2}}$ with $n > 0$ and $n' > 1$. The constants in the formulae of Eqs. (114) and (118) alone show that the quadrupole correction is much smaller than the dipole correction.

D. Isotope Shift

Variations in the neutron numbers affects the distributions of both the nuclear charge and magnetisation within the nucleus. This is manifested when one considers a finite-size nuclear model, but is not present in a point-like model. Especially when one considers energy levels of $1s_{1/2}$ and $2p_{1/2}$ electrons, whose wavefunctions penetrate the nucleus and allow for probing of its internal structure. This leads to two effects, for a finite model, that can be represented as correction factors to the point model: (1) The Breit-Rosenthal (BR) effect [85] which results from the extension of the nucleus' charge distribution and (2) Bohr-Weisskopf (BW) effect [86] which is due to the extension of magnetisation in the nucleus.

1. Breit-Rosenthal correction

Breit and Rosenthal first considered the effect of the finite distribution of charge within the nucleus on the electronic wavefunctions. By comparing a finite nuclear model with the point charge model, they found that this effect on the wavefunctions would lead to a shift in the hyperfine interaction energy. The correction factor due to the BR effect can be expressed analytically as

$$a_{\text{pd}} = a_{\text{point}}(1 + \varepsilon_{\text{BR}}) , \quad (119)$$

where a_{pd} is the hyperfine constant for a nuclear model of finite charge distribution but point-dipole nuclear magnetisation, a_{point} for a point-charge nucleus, and ε_{BR} the BR correction factor.

2. Bohr-Weisskopf correction

The distribution of nuclear magnetisation over the nuclear volume leads to the so-called BW effect [87], after Bohr and Weisskopf, who were the first to study the shift of the magnetic dipole constant from a point-dipole model. The correction factor is written as

$$a = a_{\text{pd}}(1 + \varepsilon_{\text{BW}}), \quad (120)$$

where a is the hyperfine constant for a finite nucleus, a_{pd} is the hyperfine constant for a point-dipole nucleus, and ε_{BW} is the BW correction factor.

3. Web of Hyperfine Anomalies

Recall that ε_{BR} and ε_{BW} quantify the shift in the hyperfine constant from point-like to non-point-like models for the distributions of nuclear charge and magnetisation, respectively. Moreover, to denote the dependency structure linking nuclear charge/current models to the resulting BR/BW corrections and isotope shifts, we use the term web of hyperfine anomalies.

We can extend this notion to consider the difference in shifts between two isotopes (1) and (2), the isotope shifts, which we denote by

$$\begin{aligned} {}^1\Delta_{\text{BR}}^2 &= \varepsilon_{\text{BR}}^{(1)} - \varepsilon_{\text{BR}}^{(2)} \\ {}^1\Delta_{\text{BW}}^2 &= \varepsilon_{\text{BW}}^{(1)} - \varepsilon_{\text{BW}}^{(2)}. \end{aligned} \quad (121)$$

Let us now turn our attention to the distributions used to model the nuclei. The point-like model of Eq. (115) is unique (w.r.t. the effect of the nucleus on the electronic wavefunctions) in its definition of μ_{pd} , $F_{n\kappa}^0(r)$ and $Q_{n\kappa}^0(r)$, while non-point-like distributions do not allow for a unique definition of these quantities. Using the general form of the electric current distribution given in Eq. (111) allows us to consider a range of different models, each of which carries its own set of correction factors and isotope shifts. Given the virtually infinite set of possible models, we instead consider a finite set of subsets; i.e. we consider grouping them into categories. For simplicity, consider those models where the terms of Eq. (111) are determined solely by either (i) mathematical functions,

or (ii) numeric (realistic) data. Specifically, we consider the following models, m , where $m \in \{\text{pt}, \text{sp}, \text{fm}, \text{hf}\}$, corresponding to the following: a point charge Eq. (93) ($m = \text{pt}$), a uniformly charged sphere ($m = \text{sp}$), a Fermi function distribution ($m = \text{fm}$), and our mean-field – HFBCS – approach ($m = \text{hf}$). We summarise these considerations in Tab. IV.

$\vec{j}(\vec{R})$ \diagdown $\rho(\vec{R})$	Point charge	Charge distribution model $m \in \{\text{sp}, \text{fm}, \text{hf}\}$
Point dipole	1	$(1 - \varepsilon_{\text{BR}}^m)$
Current distribution model	N/A	$(1 - \varepsilon_{\text{BR}}^m)(1 - \varepsilon_{\text{BW}})$

TABLE IV: Table summarising the composition of hyperfine anomalies due to increasingly realistic models for nuclear charge and current distributions. Note that: (i) $\varepsilon_{\text{BR}}^m$ depends only on the chosen model for charge distribution, namely P^m , Q^m and $\rho(\vec{R})$, and (ii) $\varepsilon_{\text{BW}}^m$ depends both on the charge and current distribution models, namely P^m , Q^m and $\vec{j}(\vec{R})$. Therefore a logical order of composing the effects is indicated by the arrows. Note that it is not physically meaningful to consider a nucleus having a point charge but finite magnetisation.

4. Hyperfine Anomaly

a. Magnetic Dipole Having defined the shift in magnetic hyperfine interaction energies due to different models of nuclear charge and magnetisation distributions, it is possible to compose these two effects by substituting Eq. (119) into Eq. (120), resulting in

$$a = a_{\text{point}}(1 + \varepsilon_{\text{BR}})(1 + \varepsilon_{\text{BW}}). \quad (122)$$

Now, suppose that a is to be obtained from a realistic (experimental or numerically simulated) nuclear model. In general, this is not feasible for complex atoms due to the difficulty in calculating the electronic radial wavefunctions with sufficient accuracy [87]. In practice one may obtain a experimentally (or computationally), but the uncertainties in calculating a_{point} are too large to reasonably produce the correction factors. Therefore, it is necessary to instead consider the differences of these effects between two isotopes of the same atom, referred to as the *hyperfine anomaly*. In doing so, it is possible to effectively cancel out the uncertainties contained in the a_{point} terms. Explicitly,

consider Eq. (122) for isotopes $a^{(1)}$ and $a^{(2)}$

$$\begin{aligned} a^{(1)} &= a_{\text{point}}^{(1)}(1 + \varepsilon_{\text{BR}}^{(1)})(1 + \varepsilon_{\text{BW}}^{(1)}) \\ a^{(2)} &= a_{\text{point}}^{(2)}(1 + \varepsilon_{\text{BR}}^{(2)})(1 + \varepsilon_{\text{BW}}^{(2)}) . \end{aligned} \quad (123)$$

Taking the ratio of these two quantities, we obtain

$$\frac{a^{(1)}}{a^{(2)}} = \frac{a_{\text{point}}^{(1)}(1 + \varepsilon_{\text{BR}}^{(1)})(1 + \varepsilon_{\text{BW}}^{(1)})}{a_{\text{point}}^{(2)}(1 + \varepsilon_{\text{BR}}^{(2)})(1 + \varepsilon_{\text{BW}}^{(2)})} . \quad (124)$$

Here, recall that the $a_{\text{point}}^{(i)}$ is calculated from (to simplify the notation, we have used $\mu_{\text{N}}^{(i)}$ instead of $M_z^{(1)}$) to specify the magnetic dipolar moment of the isotope (i)

$$\begin{aligned} a_{\text{point}}^{(i)} &= \frac{\mu_{\text{N}}^{(i)}}{I^{(i)}} \mathcal{U}(\kappa, j) \int_0^\infty \frac{P_{n\kappa}^0(r) Q_{n\kappa}^0(r)}{r^2} dr \\ &= g_I^{(i)} \mu_{\text{N}} \mathcal{U}(\kappa, j) \int_0^\infty \frac{P_{n\kappa}^0(r) Q_{n\kappa}^0(r)}{r^2} dr , \end{aligned} \quad (125)$$

with $\mu_{\text{N}}^{(i)} = g^{(i)} I^{(i)} \mu_{\text{N}}$, μ_{N} being the nuclear magneton and $g^{(i)}$ the gyromagnetic factor of the nucleus (i) of spin $I^{(i)}$. Note that since $P_{n\kappa}^0(r)$ and $Q_{n\kappa}^0(r)$ are the wavefunctions calculated with a point nucleus model, they are the same for both isotopes. Likewise, since $\mathcal{U}(\kappa, j)$ only depends on the electrons, it is also identical for either isotope. Thus, substituting Eq. (125) into Eq. (124) we obtain:

$$\frac{a^{(1)}}{a^{(2)}} = \frac{g^{(1)}(1 + \varepsilon_{\text{BR}}^{(1)})(1 + \varepsilon_{\text{BW}}^{(1)})}{g^{(2)}(1 + \varepsilon_{\text{BR}}^{(2)})(1 + \varepsilon_{\text{BW}}^{(2)})} . \quad (126)$$

We define $W_F^{(i)} \equiv \langle I^{(i)} I^{(i)} J J |^{\text{at}} H_{\text{hf,dip}} | I^{(i)} I^{(i)} J J \rangle = W_{F=I^{(i)}+J} = a_{\text{point}}^{(i)} I^{(i)} J$, the hyperfine splitting of the state of maximal projection. Under the point nucleus approximation, the ratio in the hyperfine splitting $W_F^{(i)}$ between two isotopes should then be:

$$\begin{aligned} \frac{W_F^{(1)}}{W_F^{(2)}} &= \frac{a_{\text{point}}^{(1)} I^{(1)} J}{a_{\text{point}}^{(2)} I^{(2)} J} \\ &= \frac{g^{(1)} I^{(1)}}{g^{(2)} I^{(2)}} \\ &= \frac{\mu_{\text{N}}^{(1)}}{\mu_{\text{N}}^{(2)}} . \end{aligned} \quad (127)$$

Therefore we define the hyperfine anomaly:

$${}^1\Delta^2 = \frac{W_F^{(1)} \mu_{\text{N}}^{(2)}}{W_F^{(2)} \mu_{\text{N}}^{(1)}} - 1, \quad (128)$$

which is therefore always 0 in a point nucleus model. However, considering a non-point nucleus model, we have

$$\begin{aligned}
\frac{W_F^{(1)}}{W_F^{(2)}} &= \frac{a^{(1)} I^{(1)} J}{a^{(2)} I^{(2)} J} \\
&= \frac{a_{\text{point}}^{(1)} I^{(1)} J}{a_{\text{point}}^{(2)} I^{(2)} J} \times \frac{(1 + \varepsilon_{\text{BR}}^{(1)})(1 + \varepsilon_{\text{BW}}^{(1)})}{(1 + \varepsilon_{\text{BR}}^{(2)})(1 + \varepsilon_{\text{BW}}^{(2)})} \\
&= \frac{\mu_N^{(1)}}{\mu_N^{(2)}} \times \frac{(1 + \varepsilon_{\text{BR}}^{(1)})(1 + \varepsilon_{\text{BW}}^{(1)})}{(1 + \varepsilon_{\text{BR}}^{(2)})(1 + \varepsilon_{\text{BW}}^{(2)})}.
\end{aligned} \tag{129}$$

Therefore the full hyperfine anomaly can be written as

$${}^1\Delta^2 = \frac{W_F^{(1)} \mu_N^{(2)}}{W_F^{(2)} \mu_N^{(1)}} - 1 = \frac{(1 + \varepsilon_{\text{BR}}^{(1)})(1 + \varepsilon_{\text{BW}}^{(1)})}{(1 + \varepsilon_{\text{BR}}^{(2)})(1 + \varepsilon_{\text{BW}}^{(2)})} - 1 \tag{130}$$

To first order approximation, this becomes:

$${}^1\Delta^2 = (1 + \varepsilon_{\text{BR}}^{(1)} - \varepsilon_{\text{BR}}^{(2)})(1 + \varepsilon_{\text{BW}}^{(1)} - \varepsilon_{\text{BW}}^{(2)}) - 1 = (1 + {}^1\Delta_{\text{BR}}^2)(1 + {}^1\Delta_{\text{BW}}^2) - 1 \tag{131}$$

where ${}^1\Delta_E^2 = \varepsilon_E^{(1)} - \varepsilon_E^{(2)}$ for $E \in \{\text{BR}, \text{BW}\}$.

b. Additional Contributions to the Isotope Shift With particular reference to the work of Büttgenbach [87], let us now consider the hyperfine anomaly from the perspective of experiment. We have thus far followed a constructive approach: We obtained ${}^1\Delta^2$ starting from a theoretical description of the electronic wavefunctions, $P_{n\kappa}(r)$ and $Q_{n\kappa}(r)$ and the nuclear charge and current distributions, $\vec{j}(\vec{R})$. However, these quantities are not accessible by experiment. In practice, a goal is to investigate the nuclear current distributions through (spectroscopic) measurements of the hyperfine constant. These may then be compared with existing models in order to infer details about the nuclear structure. Therefore, through the hyperfine anomaly it becomes possible to investigate isotopic effects on nuclear structure, and thereby test the validity of theoretical models of nuclear structure. Additionally, recall that only electrons in the s and $p_{1/2}$ orbitals have wavefunctions with non-zero probability amplitude within the nucleus. These are the only contact terms contributing to the BW Effect, and thus the hyperfine anomaly may also be used to identify contact and non-contact contributions to the hyperfine interaction.

In practice, however, the BR and BW Effects are not the only ones that contribute to the experimentally measured hyperfine anomaly, ${}^1\Delta_{\text{exp}}^2$.

Additional isotopic variations manifest themselves most prominently in mass corrections, due to the finite mass of the nucleus (keep in mind that the relativistic corrections are already included

in the relativistic electronic wavefunctions, $P_{n\kappa}(r)$ and $Q_{n\kappa}(r)$). Accounting for the motion of the nucleus-electron system about the common center of mass will result in reduced mass corrections to (i) the electronic wavefunctions, $(1 + m_e/m_N)^{-3}$ with $m_N \approx Am$ and (ii) the electronic orbital g -factor. However, it is important to note that the magnitude of these effects scales inversely with the mass of the nucleus. This makes it possible to neglect them when considering heavy elements, such as the lanthanides.

Finally, another set of contributions appears due to higher-order corrections to the magnetic hyperfine interaction energy. Indeed, the energy correction, as given in Eq. (109), is only a first-order approximation (assuming J to be a good quantum number). Higher-order terms (off-diagonal terms in the hyperfine interaction Hamiltonian) exist due to effective hyperfine interactions between different fine structure levels, via the nucleus. These interactions make J no longer a good quantum number. Thus second-order perturbation theory is needed to account for this.

c. Electric Quadrupole As in the magnetic case, we investigate how the finite size of the nucleus affects the quadrupole correction to the hyperfine interaction. For this purpose, we introduce the quantity

$$\Delta B^m \equiv \frac{b_{\text{np}}^{\text{pt}} - b_{\text{wp}}^m}{b_{\text{np}}^{\text{pt}}}, \quad (132)$$

where $m \in \{\text{pt}, \text{sp}, \text{fm}, \text{hf}\}$. This dimensionless ratio quantifies the penetration corrections for different nuclear-structure models, ranging from the simplest point-charge model (pt) to the most sophisticated Hartree–Fock–BCS model (hf). The superscript m indicates that the quadrupole constant is evaluated using the radial wave functions $P_{n\kappa}$ and $Q_{n\kappa}$ obtained from the spherically symmetric monopole potential Eq. (96), generated by the nuclear charge distribution of the corresponding model (see Fig. 10). Specifically, we consider a point charge Eq. (93) ($m = \text{pt}$), a uniformly charged sphere ($m = \text{sp}$), a Fermi distribution ($m = \text{fm}$), and an HFBCS distribution ($m = \text{hf}$). The subscript n specifies whether electron penetration into the nucleus is taken into account. When penetration is included ($n = \text{wp}$), the quadrupole constant b is computed using Eq. (116). When penetration is neglected ($n = \text{np}$), one has $b = b_{\text{pq}}$ and Eq. (117) is used instead.

To quantify the effect of the finite nucleus size on the quadrupole hyperfine correction, we also define the quantity

$$\Delta B_{\text{np}}^{\text{wp},m} \equiv \frac{b_{\text{np}}^m - b_{\text{wp}}^m}{b_{\text{np}}^m}. \quad (133)$$

The latter quantity gives us information about the influence of the model used to describe the charge distribution of the nucleus (through the radial wave functions) on the correction of the quadrupole

moment due to penetration into the nucleus. Note that $\Delta B^{\text{pt}} = \Delta B_{\text{np}}^{\text{wp,pt}}$.

In order to quantify the impact on the quadrupole constant of a completely microscopic description (HFBCS) compared with the Fermi model of the nucleus which is the most accurate of the non-microscopic models, we define the quantity

$$\Delta B \equiv \frac{b_{\text{wp}}^{\text{fm}} - b_{\text{wp}}^{\text{hf}}}{b_{\text{wp}}^{\text{fm}}}. \quad (134)$$

Finally, the isotopic effect on b for dysprosium is quantified by evaluating the quantity

$$\Delta B_{161}^{163} \equiv \frac{b_{\text{wp}}^{\text{hf}}(163) - b_{\text{wp}}^{\text{hf}}(161)}{b_{\text{wp}}^{\text{fm}}(161)}. \quad (135)$$

IV. RESULTS AND DISCUSSIONS

A. Nucleon density distributions and nuclear currents

In this section, lengths are normalised by considering the nucleus as a homogeneously charged sphere whose radius is given by

$$R_{\text{N}} = R_{\text{N}}^{(\text{emp})} = \sqrt{\frac{5}{3} R_{\text{rms}}^2}, \quad (136)$$

where R_{rms} is the root mean square (rms) charge radius of the nucleus given by the empirical formula [73]

$$R_{\text{rms}} = (0.836A^{1/3} + 0.57) \text{ fm}. \quad (137)$$

The resulting values of R_{N} (of the order of 6.6 fm for the considered nuclei) are displayed in Tab. I.

Here we discuss the results of nuclear-structure calculations obtained using the microscopic model described in Sec. II. In particular, we focus on the nucleon densities $\rho_q(\vec{R})$ as well as the convection (orbital) $\vec{j}_q^{(\ell)}(\vec{R})$ and spin $\vec{j}_q^{(s)}(\vec{R})$ current densities for neutrons ($q = n$) and protons ($q = p$), as functions of the nuclear coordinates \vec{R} . Our analysis emphasises the two dysprosium isotopes $^{161}_{66}\text{Dy}$ and $^{163}_{66}\text{Dy}$, while also including complementary results for $^{159}_{65}\text{Tb}$ and $^{165}_{67}\text{Ho}$ for the sake of comparison with odd- Z nuclei.

In Fig. 4 we show the proton (row of upper panels) and neutron (row of lower panels) densities $\rho_p(\vec{R})$ and $\rho_n(\vec{R})$ expressed in signed cylindrical coordinates (z, ϱ, φ) , with $\varrho \in \mathbb{R}$, $\phi \in [0, \pi)$, $z \in \mathbb{R}$, the slice along $\varphi = 0$ is shown, and represented with logarithmically spaced contour curves for $^{159}_{65}\text{Tb}$ (left), $^{161}_{66}\text{Dy}$ and $^{163}_{66}\text{Dy}$ (center), and $^{165}_{67}\text{Ho}$ (right).

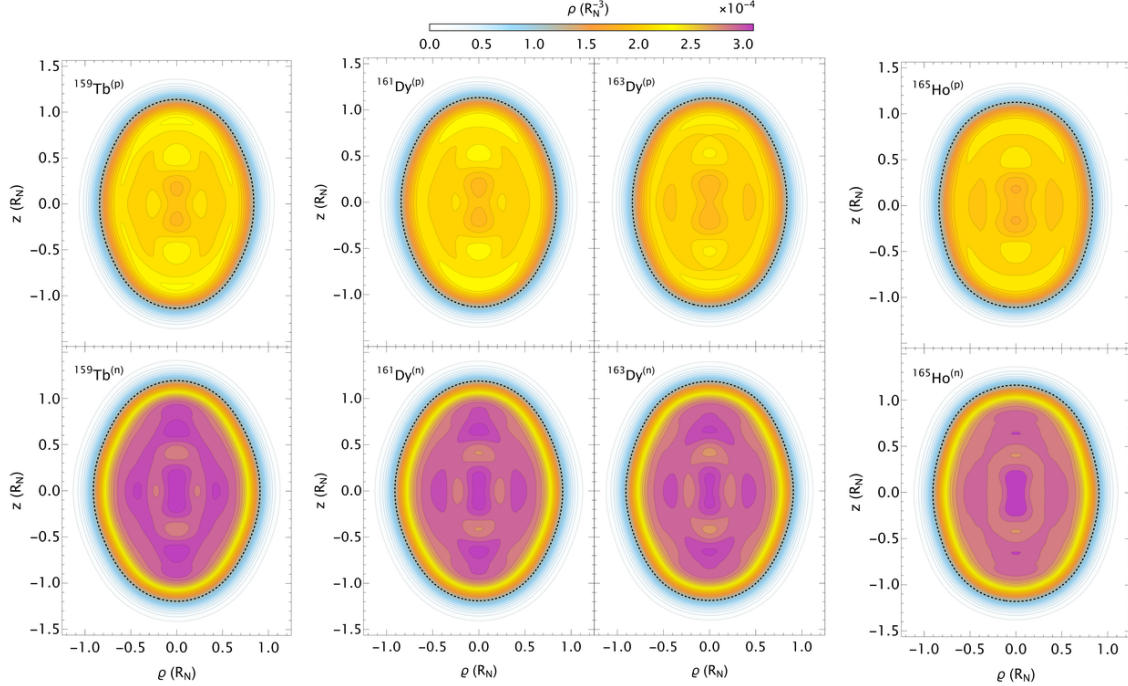


FIG. 4: Nucleon density distributions, $\rho(\vec{R})$, ((p) above: protons, ((n) below: neutrons) of $^{159}_{65}\text{Tb}$ (left), $^{161}_{66}\text{Dy}$ and $^{163}_{66}\text{Dy}$ (center), and $^{165}_{67}\text{Ho}$ (right) on logarithmically spaced contour curves. The figures are plotted in signed cylindrical coordinates (z, ϱ) , on a planar slice through the z -axis. The spatial coordinates are in units of R_N , the empirical nuclear radius (see text) for each isotope, leading to a density distribution in units of R_N^{-3} . The contours represent curves of equal density, with numerical values as indicated by the legend above. The dashed curve indicates the value of the spherically-averaged monopole distribution at a distance of $1 \times R_N$, representing the outer shell of the nucleus.

Contrary to a simplified model, in which such densities would be constant within a certain radius and fall off exponentially beyond a certain constant radius, one notices that nucleon densities show some structure in the nuclear interior and quickly decrease to 0 as the distance to the center-of-mass (at $z = \varrho = 0$) increases. Moreover one notices a deformed pattern of the isodensity contours, revealing a prolate shape for the four considered nuclei. Finally, it is worth noting that, particularly in the inner region of the nuclei, there are clear differences in the proton and neutron densities.

Next we investigate the structure of the proton and neutron current densities depending on the charge state q of the unpaired nucleon. In Fig. 5, the orthoradial components of the spin current (defined by Eq. (80)) and the orbital current (defined by Eq. (74) setting $g_n^{(\ell)}$ to 1, for illustrative

and comparative purposes, as otherwise the neutron orbital current is vanishing for the neutrons) are represented as two-dimensional color maps of the currents for the nucleons having charge state q the same as that of the unpaired nucleon, whereas Fig. 6 shows the currents for the nucleons having charge state \bar{q} different from that of the unpaired nucleon. For a nucleus with an odd number of neutrons and an even number of protons, such as ^{161}Dy or ^{163}Dy , we have $q = n$ and $\bar{q} = p$, whereas for ^{159}Tb and ^{165}Ho we have $q = p$ and $\bar{q} = n$. This choice has been made because the time-odd

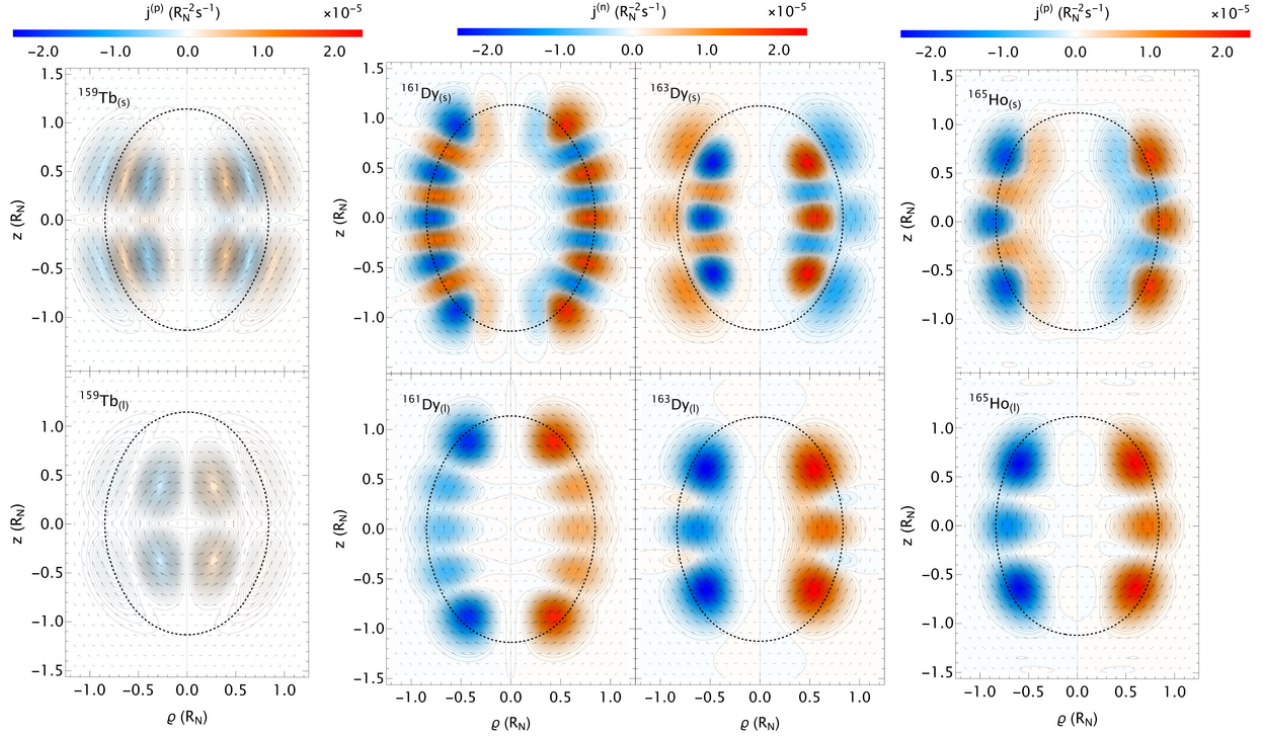


FIG. 5: (color online) Two-dimensional color maps of the orthoradial component of the spin current density $j_{q,\varphi}^{(s)}(\varrho, z)$ (top row) and orbital current density $j_{q,\varphi}^{(\ell)}(\varrho, z)/g_{\bar{q}}^{(\ell)}$ (bottom row) for the charge state q identical to the one of the unpaired nucleon in the ground states of the two odd-proton nuclei ^{159}Tb and ^{165}Ho and the two odd-neutron nuclei ^{161}Dy and ^{163}Dy .

local densities \vec{s}_q and \vec{j}_q involved, respectively, in the spin current and the convection current, are dominated by the contribution of the unpaired nucleon. Taking the example of the spin current density, we can write the orthoradial component for the charge states q as

$$j_{q,\varphi}^{(s)} = j_{\text{odd},\varphi}^{(s)} + j_{q\text{-core},\varphi}^{(s)} \quad (138)$$

where the subscript “odd” refers to the contribution of the unpaired nucleon while the subscript “ q -core” corresponds to the contribution of the remaining nucleons (called “core”) of the same

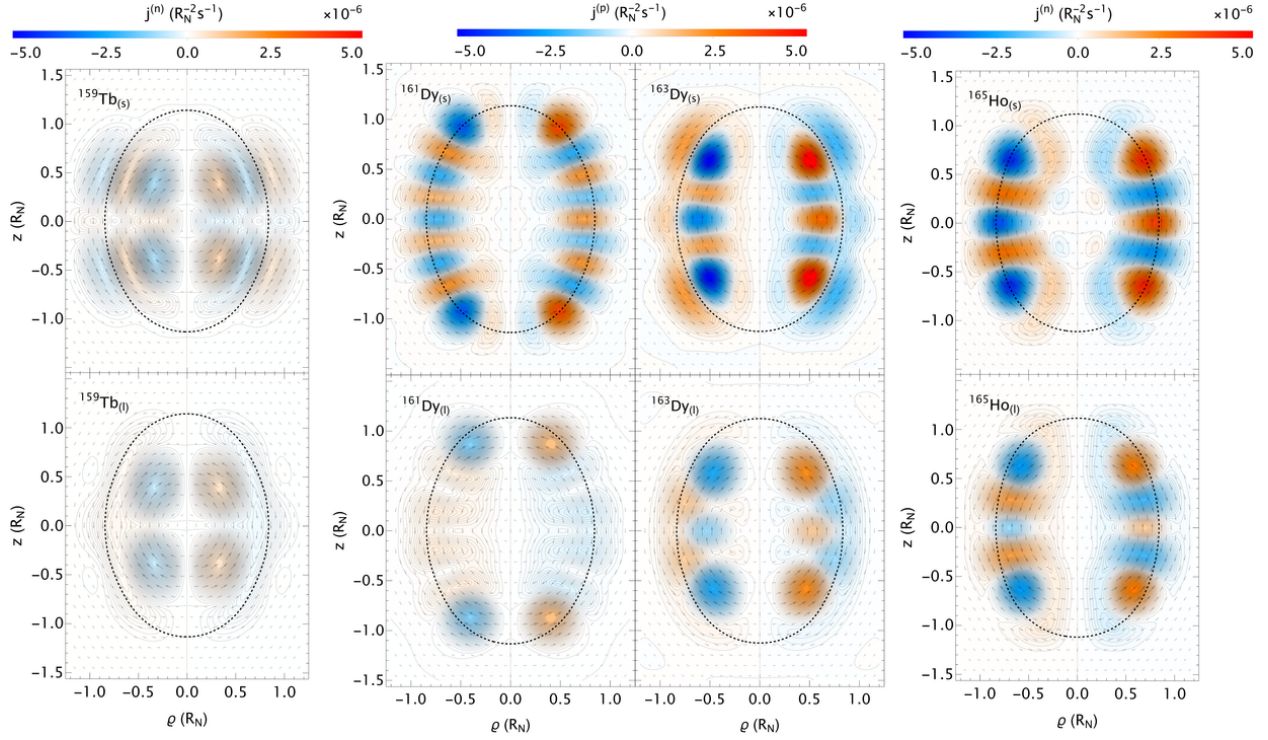


FIG. 6: (color online) Two-dimensional color maps of the orthoradial component of the spin current density $j_{\bar{q},\varphi}^{(s)}(\varrho, z)$ (top row) and orbital current density $j_{\bar{q},\varphi}^{(l)}(\varrho, z)/g_{\bar{q}}^{(l)}$ (bottom row) for the charge state \bar{q} different from the one of the unpaired nucleon in the ground states of the two odd-proton nuclei ^{159}Tb and ^{165}Ho and the two odd-neutron nuclei ^{161}Dy and ^{163}Dy .

charge state as the unpaired nucleon. By definition the current for the charge state \bar{q} receives only contributions from the core (nucleons with isospin opposite to the one of the unpaired nucleon). If the blocking procedure to describe odd nuclei were not self-consistent, the core contribution to the time-odd local densities would vanish and so would $j_{q\text{-core},\varphi}^{(s)}$ and $j_{q\text{-core},\varphi}^{(l)}$.

As can be seen in Figs. 7 and 8, displaying the contributions to both types of currents from, respectively, the unpaired nucleon and the core nucleons with the same isospin as the unpaired one, one always find the latter weaker than the former by a factor of 3 for the spin current and by a factor of 10 for the orbital current. Moreover the core contribution to the spin current is of the opposite sign to that of the unpaired nucleon. This means that the gross features of the currents result from the structure of the wave function of the unpaired nucleon. Since this wave function is dominated by a single deformed harmonic-oscillator component (in cylindrical coordinates), one can attempt to explain the number of local extrema of $j_{\bar{q},\varphi}^{(l)}$ and $j_{\bar{q},\varphi}^{(s)}$ in terms of the Nilsson quantum numbers

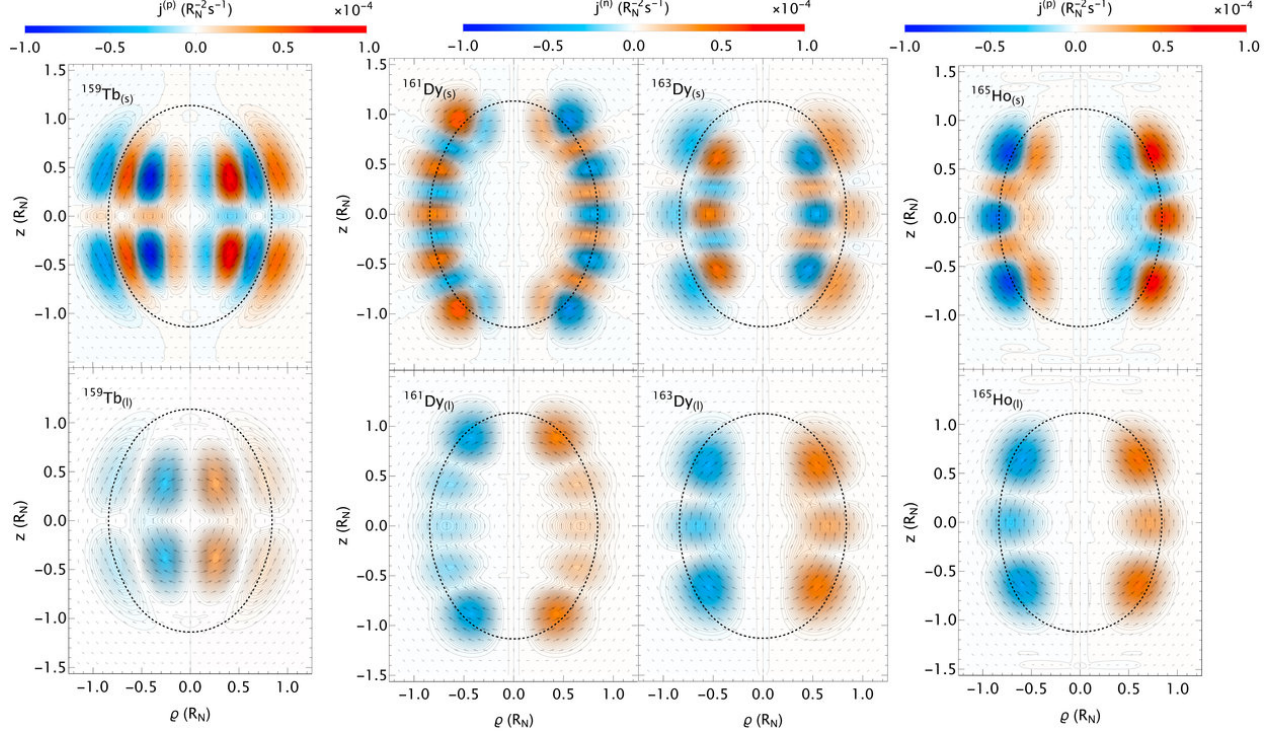


FIG. 7: (color online) Two-dimensional color maps of the orthoradial component of the spin current density $j_{\text{odd},\varphi}^{(s)}(\varrho, z)$ (top row) and orbital current density $j_{\text{odd},\varphi}^{(\ell)}/g_q^{(\ell)}$ (bottom row) of the unpaired nucleon in the ground states of the two odd-proton nuclei ^{159}Tb and ^{165}Ho and the two odd-neutron nuclei ^{161}Dy and ^{163}Dy .

$\Omega^\pi [Nn_z\Lambda]$ of the unpaired nucleon. Within this approximation, the projection $\sigma = \Omega - \Lambda$ of spin angular momentum on the symmetry axis becomes a good quantum number and so do N , n_z and Λ . In Eqs. (74) and (80) the sum over k is reduced to the term corresponding to the unpaired nucleon, for which $\phi_k^{(-\sigma)}(\varrho, z) = 0$ and $\phi_k^{(\sigma)}(\varrho, z) \approx \psi_{Nn_z\Lambda}(\varrho, z)$, a cylindrical harmonic-oscillator wave function defined by

$$\psi_{Nn_z\Lambda}(\varrho, z) = \mathcal{N} H_{n_z}(\xi) \eta^{\Lambda/2} L_{n_r}^{(\Lambda)}(\eta) e^{-(\xi^2 + \eta)/2}, \quad (139)$$

where \mathcal{N} is a normalisation coefficient, H_{n_z} is the Hermite polynomial of degree n_z and $L_{n_r}^{(\Lambda)}$ is the generalised Laguerre polynomial of degree $n_r = (N - n_z - \Lambda)/2$, $\xi = z \sqrt{m\omega_z/\hbar}$ and $\eta = \varrho^2 m\omega_\perp/\hbar$. Among the four studied nuclei, the ^{159}Tb nucleus in its ground-state has a dominant Nilsson configuration of $3/2^+ [411]$, such that $n_r = 1$, while the other three nuclei have $n_r = 0$ in their respective dominant Nilsson configurations. The study of local extrema of the resulting expressions of the orthoradial components of $\vec{\nabla} \times \vec{s}_q$ and \vec{j}_q shows that there are $n_z + 1$ local

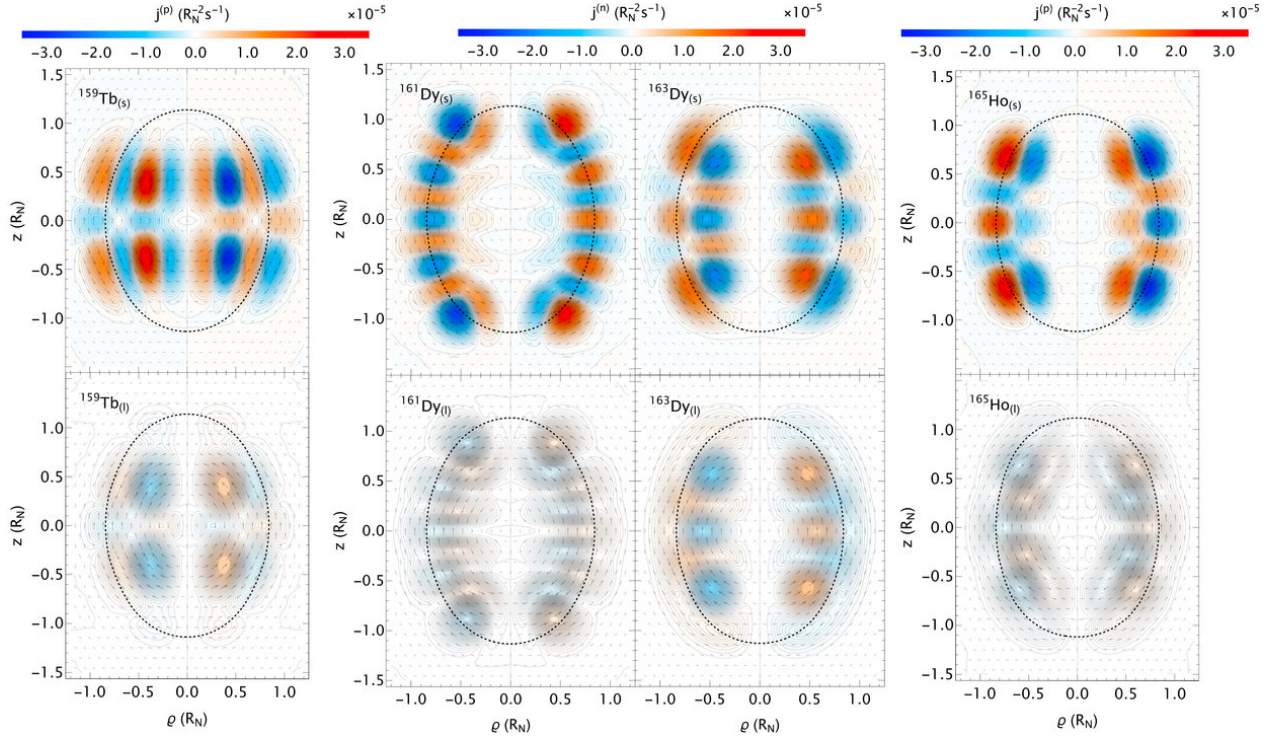


FIG. 8: (color online) Two-dimensional color maps of the orthoradial component of the spin current density $j_{q\text{-core},\varphi}^{(s)}(\varrho, z)$ (top row) and convection current density $j_{q\text{-core},\varphi}^{(l)}(\varrho, z)$ without the $g_q^{(l)}$ factor (bottom row) of the core with same isospin as the unpaired nucleon in the ground states of the two odd-proton nuclei ^{159}Tb and ^{165}Ho and the two odd-neutron nuclei ^{161}Dy and ^{163}Dy .

maxima with respect to z in both functions, whose z values correspond to the roots of $H_{n_z+1}(\xi)$; whereas in the ϱ direction, the spin current has $n_r + 1$ maxima and the convection current has 2 minima and 2 maxima for the cases at play. Table V summarises these properties applied to each of the four studied nuclei. This matches the number of extrema in the exact currents presented in Fig. 5.

In addition, depending on the type of current (orbital or spin), we can identify the origin of the magnetism at the scale of the nucleus. As mentioned above, the neutron orbital current does not contribute to nuclear magnetism.

Although this single-particle model of the unpaired nucleon in a harmonic potential falls short in fully capturing the complex interactions between nucleons in the nucleus and the resulting currents, it offers a useful foundation for understanding the structure of current distributions. For instance, in the case of ^{163}Dy , which has 97 neutrons, simple predictions from the nuclear shell model with-

Nucleus	$\Omega^\pi [Nnz\Lambda]_q$	n_r	Maxima in the z direction	Maxima, minima in the ρ direction	
				$j_{\text{odd},\varphi}^{(s)}/g_q^{(s)}$	$j_{\text{odd},\varphi}^{(\ell)}/g_q^{(\ell)}$
^{159}Tb	$3/2^+[411]_p$	1	2	2, 2	2
^{165}Ho	$7/2^- [523]_p$	0	3	1, 1	1
^{161}Dy	$5/2^+[642]_n$	0	5	1, 1	1
^{163}Dy	$5/2^- [523]_n$	0	3	1, 1	1

TABLE V: Number of extrema along the z and ρ directions of the spin and convection currents without Landé factors in the approximation of the unpaired nucleon in its leading Nilsson configuration $\Omega^\pi [Nnz\Lambda]_q$.

out residual interaction suggest that the unpaired neutron occupies the $1h_{9/2}$ subshell [88], which is the dominant contribution in the expansion of the actual single-particle state in the spherical harmonic-oscillator basis. On the contrary, experimental data shows that the ground state of ^{163}Dy corresponds to a $K^\pi = 5/2^-$ band [72].

Figure 9 shows the normalised current distributions [102] calculated for the 3D spherical harmonic oscillator eigenstate, which corresponds to the quantum state $|n\ell j m_j = -5/2\rangle$. This state can be expressed as a combination of orbital (m_ℓ) and spin (m_s) components

$$|n\ell j m_j = -5/2\rangle = \frac{1}{\sqrt{11}} \left(\sqrt{3} |n\ell m_\ell = -2 m_s = -1/2\rangle - 2\sqrt{2} |n\ell m_\ell = -3 m_s = +1/2\rangle \right). \quad (140)$$

In this expression, $n = 6$ and $\ell = 5$, which correspond to the $1h$ orbital state. The Clebsch-Gordan coefficients in the equation represent the relative contributions of two specific combinations of the orbital angular momentum (m_ℓ) and spin angular momentum (m_s) to form the total angular momentum state $m_j = -5/2$.

The current distribution closely resembles the one obtained for ^{163}Dy . Similar qualitative considerations can be applied to the other isotopes and elements investigated in this study, even though, in some cases, one should also account for configuration mixing and other non-trivial effects. For example, the single particle spectra for both the neutrons and the protons in ^{162}Dy , obtained from the HFBCS calculations, are shown in Fig. 2. The Nilsson quantum numbers of the corresponding harmonic oscillator states are also indicated.

On the upper part of Fig. 10 we have shown the monopole electric potentials, $\phi_{0,0}$, relating to

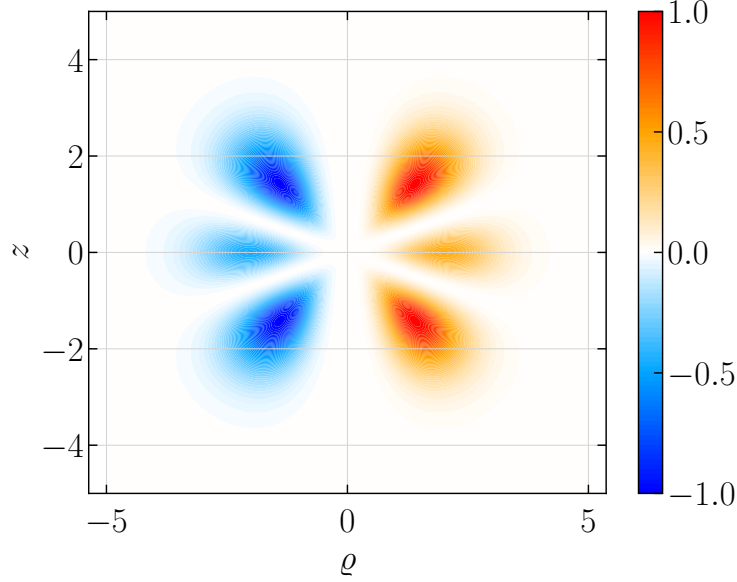


FIG. 9: (color online) Normalised current distribution for the 3D spherical harmonic oscillator eigenstate corresponding to the quantum state $|1h_{9/2} m_j = -5/2\rangle$, which is a component of the single particle ground state of ^{163}Dy according to the shell model. The figure is plotted in signed cylindrical coordinates (z, ρ) , on a planar slice through the z -axis. The contours represent curves of equal density, with numerical values as indicated by the legend.

the effect of the spatial distribution of protons within the nuclei of ^{161}Dy . Due to the spherical symmetry of the monopole, it is given in terms of the electronic radial component r , by averaging over the angular components. Here, and throughout the text unless specified otherwise, r is expressed in units of the nuclear radius, R_N , thus giving the potential in units of $R_N^{-1}e/4\pi\epsilon_0$. Each curve describes a different model for the monopole density distribution. Note how outside of the nuclear radius at $R/R_N = 1$ the potentials are all effectively equivalent, and the differences in the HFBCS calculations for each isotope is also minor (shown by the green curve and the corresponding y -axis on the righthand side). The lower part of the figure shows distributions of the monopolar nuclear charge densities, $\rho_{0,0}(R) = \frac{1}{4\pi} \int \rho(\vec{R})d\Omega$, relating to the radial distribution of protons within the nuclei of isotope ^{161}Dy . Due to the spherical symmetry of the monopole, it is given in terms of the nuclear radial component R , by averaging over the angular components. Here, and throughout the text unless specified otherwise, R is used in units of the nuclear radius, R_N , thus giving the monopole in units of R_N^{-3} . Note how, due to Coulomb repulsion of the protons, the HFBCS model suggests a lower density of protons at the center of the nucleus that increases unevenly towards a

maximum at the outer edge. The results are almost equivalent for the two isotopes, with only a small difference in the HFBCS model near $R = 0$ (see green curve and the corresponding y -axis on the righthand side). The dashed vertical line represents the surface of the nucleus at $R = 1 \times R_N$, to which the other curves are normalised.

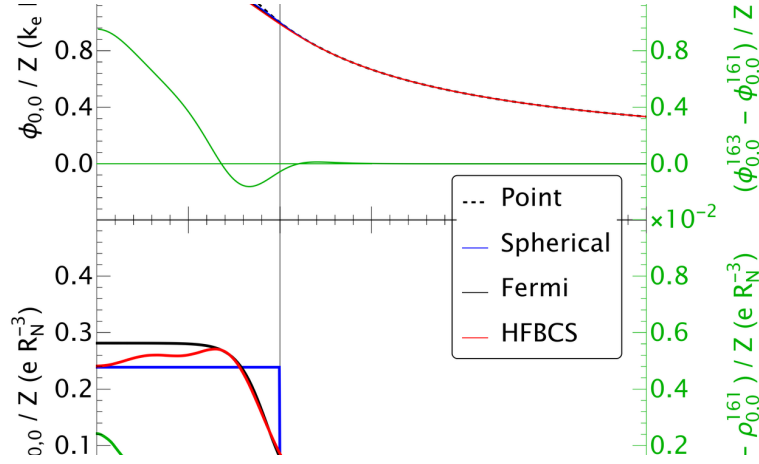


FIG. 10: (color online) Bottom part: proton monopole density (as a function of nuclear radial coordinate R) obtained for the ^{161}Dy nucleus from a uniform sharp-edge (blue), a Fermi-function type (black) and the distribution resulting from the here presented HFBCS type calculation with self-consistent blocking. Upper part: monopole potential (as a function of the electronic radial coordinate r) experienced by the electron resulting from the different approaches for the density. The Coulomb potential generated by a nuclear point-charge density is shown by the dotted line and $k_e = e/4\pi\epsilon_0$. The green lines show the difference in density (bottom) and potential (upper) between the two dysprosium isotopes obtained with the HFBCS model.

In Fig. 11a, we show the monopole potentials and charge densities for ^{159}Tb after normalising by Z , the total charge of the nucleus. The radial coordinates are plotted in units of R_N . One finds, as expected, that the monopole potentials and charge densities for ^{159}Tb bear a strong similarity to those of ^{161}Dy at a first glance. Using

$$\Delta\rho_{159}^A = \frac{\rho_{0,0}^{(A)} - \rho_{0,0}^{(159)}}{\rho_{0,0}^{(159)}}, \quad (141)$$

$$\text{and } \Delta\phi_{159}^A = \frac{\phi_{0,0}^{(A)} - \phi_{0,0}^{(159)}}{\phi_{0,0}^{(159)}}, \quad (142)$$

one can take a closer look and observe the compared radial spherically averaged charge densities of the isotopes ^{161}Dy , ^{163}Dy and ^{165}Ho , relative to ^{159}Tb , in Fig. 11b. They are shown as Z -normalised and rescaled to be expressed in units of the respective nuclear radii eR_N^{-3} . Note that the addition of 2 nucleons has the effect of seemingly concentrating the monopolar charge densities near the nuclear surface (nuclear radius, $r = R_N$). Since R_N increases with A , the charge distributions are also more spread out for the heavier isotopes, as expected. One may consider that for these heavy nuclei with densely-packed, practically incompressible, cores having filled inner shells and charge densities not varying significantly between isotopes, the additional nucleons appear instead to be bound near the surface in the unfilled outer shells.

We now turn our attention to the magnetic dipole moments of the isotopes ^{161}Dy , ^{163}Dy , ^{159}Tb , and ^{165}Ho . The magnetic dipole moments were obtained by integrating the magnetic dipole densities over the volume of the nucleus,

$$\rho_{1,0}(R) = \frac{1}{2} \sqrt{\frac{3}{\pi}} \int \cos(\Theta) \rho(\vec{R}) d\Omega. \quad (143)$$

The magnetic dipole density contributions are given by the sum of the proton and neutron spin densities and the proton orbital current density (the neutron orbital current density makes no contribution since its Landé g factor is zero).

In Fig. 12, we show the magnetic dipole densities for each isotope. The radial part of the dipole density is plotted in units of R_N^{-3} , with the distributions of the magnetic dipole radial density contributions normalised by the total magnetic moment of the respective isotope $\mu_N^{(A)}$, as obtained from the HFBCS model. Across these rare-earth isotopes, the magnetic dipole densities are predominantly governed by the spin currents of the unpaired nucleons. For dysprosium (even Z , odd N), the neutron (spin) currents dominate—most clearly when considering ^{163}Dy , which has two additional neutrons compared to ^{161}Dy . In contrast, for terbium and holmium (odd Z , even N), the dominant contributions arise from the proton spin and orbital currents. In all cases, consistent with this picture of the unpaired nucleons, the dipole-density curves exhibit peaks close to the (spherically averaged) nuclear radius R_N . This is consistent with the current distributions observed in Figs. 8 to 10, as the nuclear magnetism originates mostly from the unpaired nucleon that is naturally more free to move in the lower density outer shell of the nucleus as opposed to the densely packed inner core. Moreover, comparing the Dy isotopes shows that adding only two neutrons can drive a complete sign reversal of the dipole densities, keeping in mind that $\mu_N^{(161)}$ and $\mu_N^{(163)}$ carry

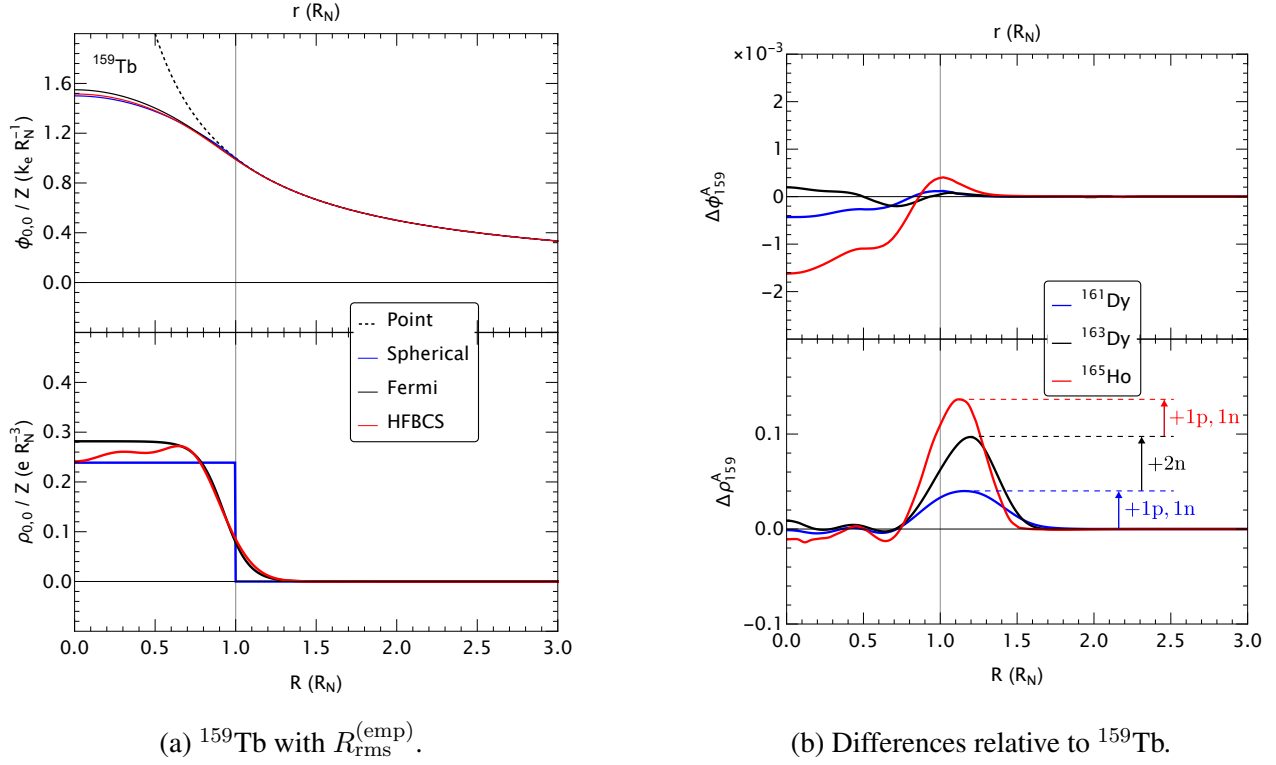


FIG. 11: (color online) Z -normalised (radial, spherically averaged) proton monopole charge densities, $\rho_{0,0}(R) = \frac{1}{4\pi} \int \rho(\vec{R}) d\Omega$ (lower panels), and the corresponding monopole electron potentials (upper panels) for ^{159}Tb . The radial coordinate is shown as r/R_N for the potentials seen by atomic electrons (upper panels) and as R/R_N for the nuclear charge densities (lower panels), normalised with respect to the empirical nuclear radius R_N . The densities are in units of e/R_N^3 ; potentials are in units of k_e/R_N , with $k_e \equiv \frac{e}{4\pi\epsilon_0}$. HFBCS-type (red) calculations are compared with a uniform sphere (blue), a Fermi distribution (black), and a point-charge Coulomb potential (dotted). In (b), differences relative to ^{159}Tb are shown for ^{161}Dy (blue), ^{163}Dy (black) and ^{165}Ho (red), using each isotope's own R_N for normalisation.

different signs.

Quadrupole radial potentials, $\phi_{2,0}(r)$ produced by the spatial distributions of protons within the spherically deformed nuclei of isotopes ^{159}Tb (left), ^{161}Dy (center, black) and ^{163}Dy (center, red) and ^{165}Ho (right) are shown in Fig. 13. By spherically averaging over the angular components, it is given only in terms of the radial component r . r is used in units of the nuclear radius, R_N , thus giving the potential in units of $eR_N^{-3}/4\pi\epsilon_0$. The dashed vertical line represents the surface of the nucleus at $R = R_N$, to which the other curves are normalised. Note the strong similarities in the

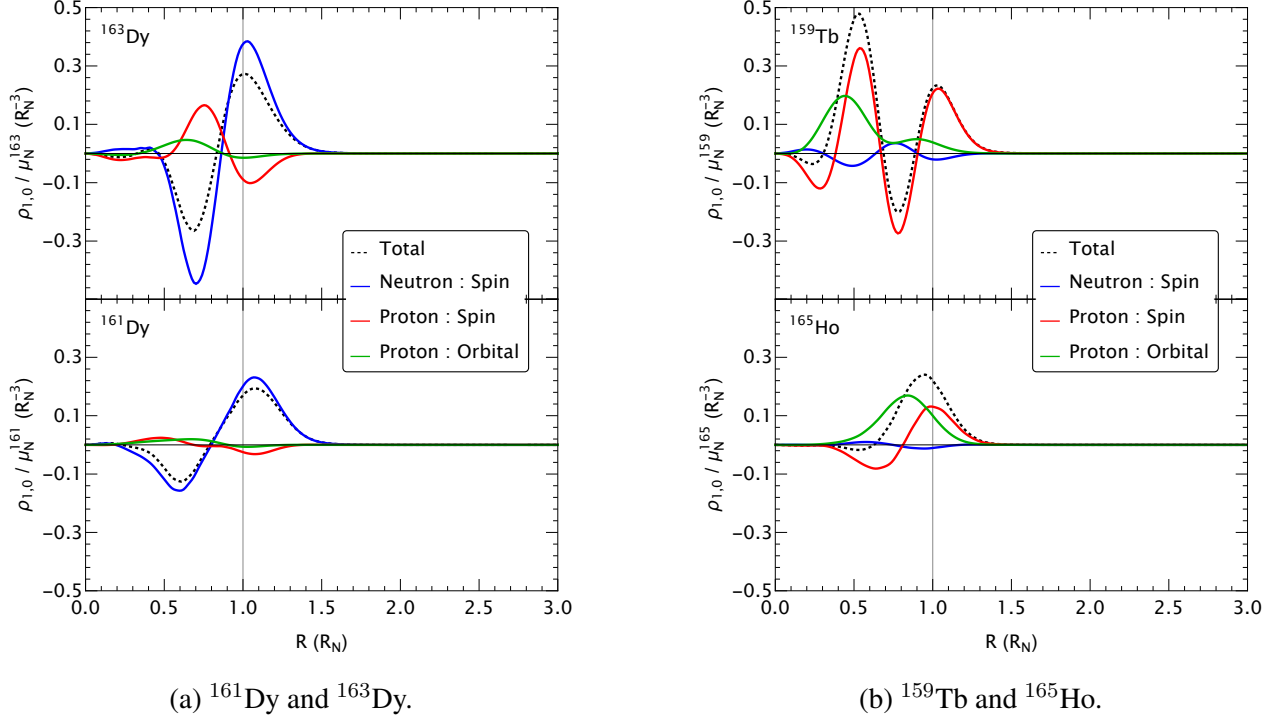


FIG. 12: (color online) Radial distributions of the magnetic dipole density contributions, $\rho_{1,0}(R)$, relating to the spatial distribution of protons and neutrons within the nuclei of isotopes: (a) ^{163}Dy (upper panel) and ^{161}Dy (lower panel), and (b) ^{159}Tb (upper panel) and ^{165}Ho (lower panel). By spherically averaging over the angular components, it is given only in terms of the radial component R . R is used in units of the nuclear radius, R_N , thus giving the dipole in units of $\mu_N R_N^{-3}$. The dashed vertical line represents the surface of the nucleus at $R = 1 \times R_N$, to which the other curves are normalised. Moreover, the dipole densities are normalised by $\mu_N^{(A)}$ for each isotope such that they lie on the same scale. Each curve describes a different contribution to the dipole density distribution: (Dashed) The total dipole density, (Blue) the neutron spins, (Red) the proton spins, and (Green) the proton orbital currents.

curves for each dysprosium isotope, since the neutrons do not contribute towards the quadrupole moment, and they have the same number of protons, yet a slightly higher maximum for ^{163}Dy . We may remark that the relative differences in the quadrupole potentials at the nuclear radius ($r = 1$) for the different elements (Tb, Dy, Ho) are consistent with that of their experimentally measured quadrupole moments (cf. Tab. I). Moreover, in comparison with the monopole potentials (cf. upper panels of Figs. 10 and 11) where Gauss's Law ensures that the potentials due to all nuclear

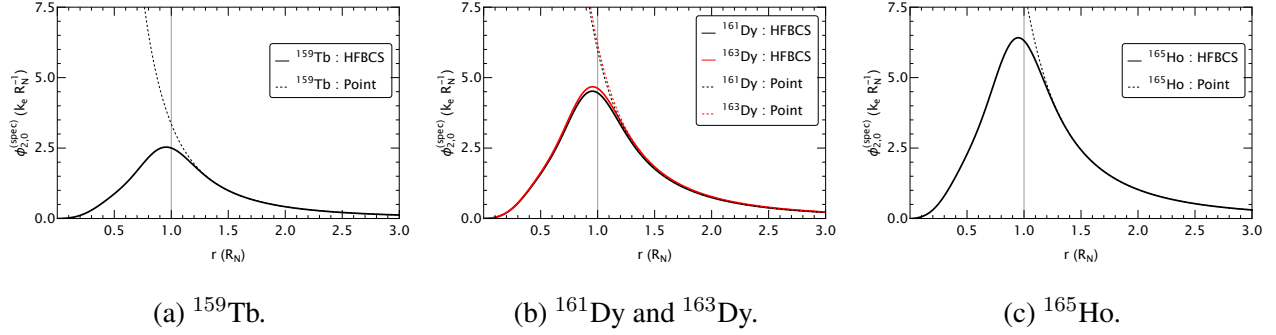


FIG. 13: (color online) The radial part of the spectroscopic quadrupole contribution to the nuclear electric potential, $\phi_{2,0}^{(\text{spec})}$ as defined in Eq. (97), in units of k_e/R_N , for (a) ^{159}Tb (black), (b) ^{161}Dy (black) and ^{163}Dy (red) and (c) ^{165}Ho (black), as obtained from our HFBCS calculations, compared with the corresponding potentials obtained for the quadrupole potential of a point-like model ($\frac{Q_0^{(2)}}{r^3}$) (dashed). Here, $k_e \equiv \frac{e}{4\pi\epsilon_0}$ is the Coulomb constant.

models converge to the same value outside of the nucleus ($r \geq 1$), the quadrupole potentials are not constrained in the same way and exhibit observable differences at, and just outside, the nuclear radius.

B. Results combining nuclear and atomic descriptions

In the following, unless otherwise stated, atomic units are used: $m_e = e = 4\pi\epsilon_0 = \hbar = 1$.

1. Charge corrections

Figure 14 shows the radial parts (large $P_{n\kappa}$ and small $Q_{n\kappa}$ components) of the Dirac wave functions of the first two electronic orbitals $1s_{1/2}$ and $2p_{1/2}$ of $^{163}\text{Dy}^{65+}$ ($Z = 66$). They have been obtained for different models of the nucleus (monopole charge distributions): point charge localised in the center of the nucleus (Point), spherical distribution (Spherical), Fermi distribution (Fermi) and finally the microscopic distribution calculated in the HFBCS model. In all situations, the three models Spherical, Fermi and HFBCS give very similar results to each other. On the other hand, we note that the results obtained with the point charge model deviate significantly from those of the other models for distances smaller than the radius of the nucleus R_N (represented by a vertical line on the graphs). In a way, these electronic wavefunctions converging to the same behaviour outside

of the nuclear radius is an illustration of Gauss's theorem in electrostatics. To show the effect of a microscopic description (HFBCS) compared with the empirical Fermi model usually used in atomic physics, the difference between the HFBCS and Fermi models, multiplied by a factor of 20, is presented in green. As expected, this difference is only visible inside the nucleus and is very small.

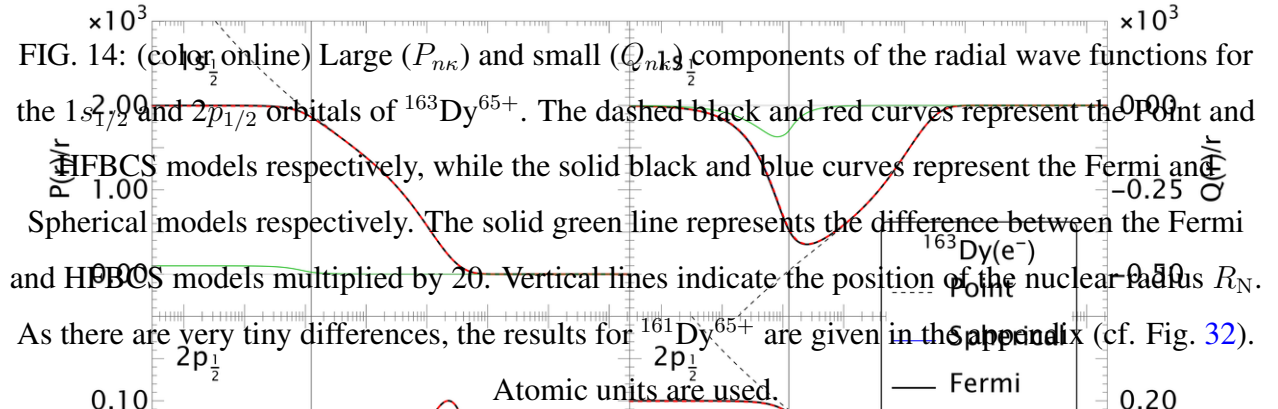
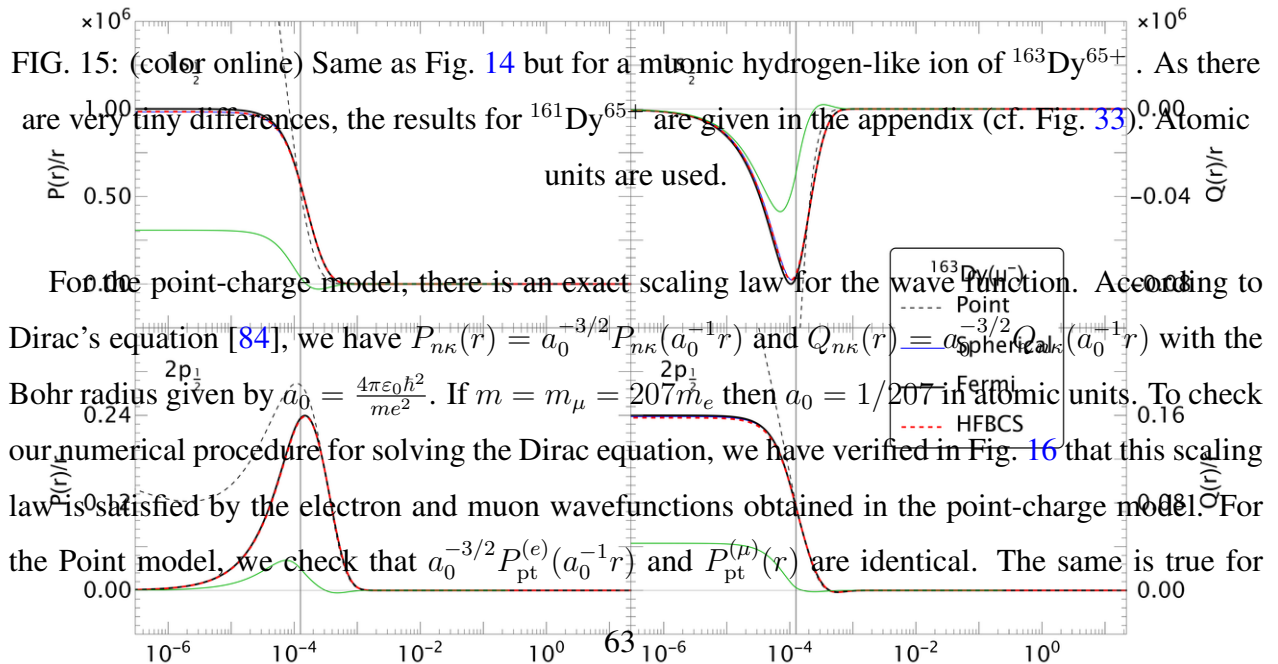


Figure 15 is similar to Fig. 14, but for a muon. Compared with the electron case, it is clear that the density of presence inside the nucleus is much greater. As in the case of the electron, the deviation from the point-charge model also occurs in the vicinity of the nuclear radius. Finally, the difference between the Fermi and HFBCS models is much larger, than in the electronic case. This makes muonic atoms interesting physical systems for probing microscopic properties at the nuclear scale. Muonic atoms can also be used to probe the distribution of the magnetic field inside the nucleus, as we will see later.



$a_0^{-3/2}Q_{\text{pt}}^{(e)}(a_0^{-1}r)$ and $Q_{\text{pt}}^{(\mu)}(r)$. We also note that the latter is no longer fulfilled at all if we use a realistic nucleus model such as HFBCS.

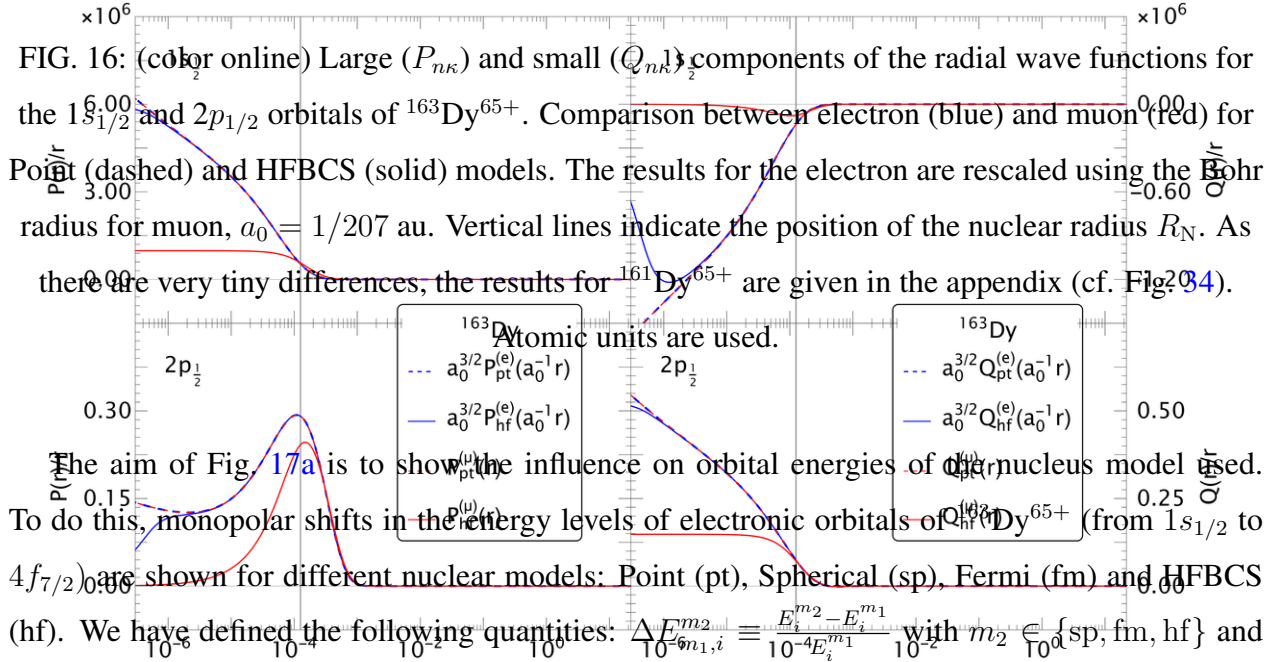


FIG. 16: (color online) Large ($P_{n\kappa}$) and small ($Q_{n\kappa}$) components of the radial wave functions for the $1s_{1/2}$ and $2p_{1/2}$ orbitals of $^{163}\text{Dy}^{65+}$. Comparison between electron (blue) and muon (red) for Point (dashed) and HFBCS (solid) models. The results for the electron are rescaled using the Bohr radius for muon, $a_0 = 1/207$ au. Vertical lines indicate the position of the nuclear radius R_N . As there are very tiny differences, the results for $^{161}\text{Dy}^{65+}$ are given in the appendix (cf. Fig. 234).

The aim of Fig. 17a is to show the influence on orbital energies of the nucleus model used. To do this, monopolar shifts in the energy levels of electronic orbitals of $^{163}\text{Dy}^{65+}$ (from $1s_{1/2}$ to $4f_{7/2}$) are shown for different nuclear models: Point (pt), Spherical (sp), Fermi (fm) and HFBCS (hf). We have defined the following quantities: $\Delta E_{n_1, i}^{m_2} \equiv \frac{E_i^{m_2} - E_i^{m_1}}{10^{-4}E_i^{m_1}}$ with $m_2 \in \{\text{sp, fm, hf}\}$ and $m_1 \in \{\text{pt, fm}\}$ and $\Delta E_{161, i}^{163} \equiv \frac{E_i^{163} - E_i^{161}}{E_i^{161}}$ with i running from $1s_{1/2}$ to $4f_{7/2}$. In the upper panel of the figure, the relative difference with the point charge is shown. This relative difference is always very small, of the order of 0.01%, and is comparable for the three more realistic nuclear models. Moreover, for the same model, the affected states are almost exclusively the s states, and the effect decreases with the quantum number n . The $p_{1/2}$ states are minimally affected, which is due to the greater penetration of s orbitals inside the nucleus, where there are strong deviations from the point-charge model. Moreover, as n increases, the amplitude of the wave function in the nuclear region decreases.

In order to estimate the effect of a microscopic modeling of the nucleus (HFBCS model) as compared to a macroscopic description (Fermi model), the lower panel shows the relative energy difference between the two models defined by $\Delta E_{\text{hf}, i}^{\text{fm}}$. This quantity is very small, always less than 0.001%. The same trends can be observed as those discussed for the upper panel.

Finally, the influence of the isotope on the energy shift of the orbitals is also studied by evaluating $\Delta E_{161, i}^{163} \equiv \frac{E_i^{163} - E_i^{161}}{E_i^{161}}$. This quantity is shown in the lower panel, and its value is always less than 0.0001%. As before, the same trends can be observed as those discussed for the upper panel.

Figure 17b presents the results of the same type of calculations as in Fig. 17a, but for a muonic atom. As expected, the major difference is the very significant increase in the value of the quantities

studied. $\Delta E_{\text{pt},i}^{m_2}$ with $m_2 \in \{\text{sp}, \text{fm}, \text{hf}\}$ is of the order of ten percent, reaching over 40% for the $1s_{1/2}$ orbital. The same observation can be made for the muonic p orbitals, but with the addition of a noticeable deviation for the $p_{3/2}$ states. We can therefore test the description of the nucleus on orbital energies. Moreover, the relative difference between HFBCS and Fermi models is no longer negligible, and can reach 1% for the $1s_{1/2}$ orbital. Finally, a less negligible isotopic effect is observed with $\Delta E_{161,i}^{163}$ of the order of 0.01%.

Figure 18 shows the Breit-Rosenthal correction obtained for different nuclear models and orbitals. This quantity is denoted by ε_{BR} , as defined in Eq. (119), and is shown in the upper panel. The different nuclear models all exhibit approximately the same behaviour and results. As expected, ε_{BR} is much larger for $ns_{1/2}$ orbitals, with a value of around 5%. It is much smaller for $np_{1/2}$ orbitals and practically zero for $np_{3/2}$ orbitals and the others. When we compare the value of ε_{BR} as a function of n for $s_{1/2}$ and $p_{1/2}$ orbitals, we see that it is almost constant.

On the lower panel of the figure, the quantity $\Delta\varepsilon_{\text{fm}}^{\text{hf}} \equiv \frac{\varepsilon_{\text{BR}}^{\text{hf}} - \varepsilon_{\text{BR}}^{\text{fm}}}{\varepsilon_{\text{BR}}^{\text{fm}}}$ is represented. It quantifies the extent of the corrections made by a microscopic model (i.e. HFBCS) compared with a more macroscopic one, namely the Fermi model. The correction is of the order of one percent for all orbitals except for the $np_{3/2}$ orbitals, where it reaches more than 5%. The lower panel of the figure also shows the quantity $\Delta\varepsilon_{161}^{163} \equiv \frac{\varepsilon_{\text{BR}}^{\text{hf}}(163) - \varepsilon_{\text{BR}}^{\text{hf}}(161)}{\varepsilon_{\text{BR}}^{\text{hf}}(161)}$. It provides information on the influence of the isotope on the Breit-Rosenthal correction. The isotopic effect is of the order of 0.2% for all orbitals except for the $np_{3/2}$ orbitals, where it reaches about 1%.

Figure 19 is identical to Fig. 18, but pertains to a muonic atom. As in the electronic case, the different models yield similar results. What is very different is the value of the correction, which is close to 100% for $ns_{1/2}$ orbitals. This value is more than 20 times higher than the one obtained

(a) Electronic orbitals of $^{163}\text{Dy}^{65+}$. (b) Muonic orbitals of $^{163}\text{Dy}^{65+}(\mu^-)$.

FIG. 17: (color online) Monopolar shifts in the energy levels of electronic orbitals of $^{163}\text{Dy}^{65+}$ (from $1s_{1/2}$ to $4f_{7/2}$) in different nuclear models, Point (pt), Spherical (sp), Fermi (fm) and HFBCS (hf). We have defined, $\Delta E_{m_1,i}^{m_2} \equiv \frac{E_i^{m_2} - E_i^{m_1}}{E_i^{m_1}}$ with $m_2 = \text{sp}, \text{fm}, \text{hf}$ and $m_1 = \text{pt}, \text{fm}$ and $\Delta E_{161,i}^{163} \equiv \frac{E_i^{163} - E_i^{161}}{E_i^{161}}$ with i running from $1s_{1/2}$ to $4f_{7/2}$. This latter quantity was evaluated using the energies of the HFBCS model. As there are very small differences, the results for $^{161}\text{Dy}^{65+}$ are given in the appendix (cf. Fig. 35a).

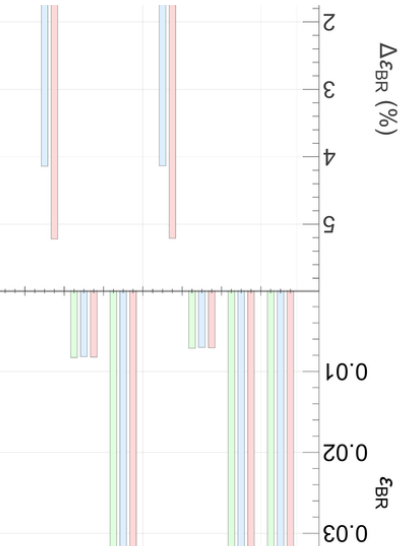


FIG. 18: (color online) Breit-Rosenthal correction ε_{BR} for $^{163}\text{Dy}^{65+}$ in different nuclear models: Spherical, Fermi and HFBCS. We have defined, $\Delta\varepsilon_{\text{fm}}^{\text{hf}} \equiv \frac{\varepsilon_{\text{BR}}^{\text{hf}} - \varepsilon_{\text{BR}}^{\text{fm}}}{\varepsilon_{\text{BR}}^{\text{fm}}}$ (reading on the left axis) and $\Delta\varepsilon_{161}^{163} \equiv \frac{\varepsilon_{\text{BR}}^{\text{hf}}(163) - \varepsilon_{\text{BR}}^{\text{hf}}(161)}{\varepsilon_{\text{BR}}^{\text{hf}}(161)}$ (reading on the right axis). The results for $^{161}\text{Dy}^{65+}$ are given in the appendix (cf. Fig. 36).

in the electronic case. This increase is a direct consequence of the greater penetration of wave functions into the nucleus. The difference between $ns_{1/2}$ and $np_{1/2}$ is smaller in the muonic case, and the corrections to the $np_{3/2}$ orbitals are no longer negligible.

In the case of $\Delta\varepsilon_{\text{fm}}^{\text{hf}}$ and $\Delta\varepsilon_{161}^{163}$, as can be seen in the lower panel, the situation is very different between the electronic and muonic cases. In hydrogen-like Dy, the ℓ -dependence of the BR effect is controlled by the orbital's spatial extent relative to the nucleus: for electrons, increasing ℓ drives the probability density rapidly outward via centrifugal effects, so that near R_{N} the wavefunctions from different models and isotopes converge toward one another much faster than their respective BR effects decay. Hence the quantities $\Delta\varepsilon_{\text{fm}}^{\text{hf}}$ and $\Delta\varepsilon_{161}^{163}$ remain roughly constant as functions of ℓ since the numerators decay to zero faster than the denominators. For muons, the much smaller Bohr radius keeps the wavefunctions concentrated closer to the nuclear surface, so model- and isotope-dependent differences in wavefunctions remain large and decay more slowly than the BR effect as functions of ℓ . Hence the denominators in $\Delta\varepsilon_{\text{fm}}^{\text{hf}}$ and $\Delta\varepsilon_{161}^{163}$ decay to zero faster than the numerator terms, resulting in monotonically increasing fractional effects with ℓ . Focusing on the electronic case, the largest relative BR signals arise for $j = \frac{3}{2}$ ($p_{3/2}, d_{3/2}$). Their absolute interior amplitude is modest, while $(\Delta\Psi/\Psi)$ is strongly model and isotope dependent, so the observable BR effect is

comparatively large.

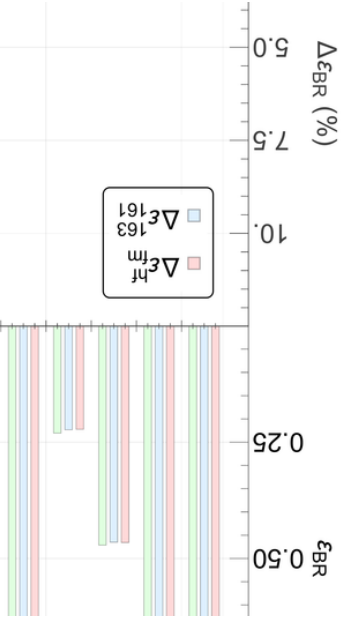


FIG. 19: (color online) Same as Fig. 18 but for a muonic hydrogen-like ion. The results for $^{161}\text{Dy}^{65+}$ are given in the appendix (cf. Fig. 37).

It is interesting to note however, that model discrepancies for the s states are of the same order of magnitude as QED and nuclear polarisation effects [89] ($\approx 10 - 100$ eV), this hints at $p_{1/2}$ states being more favorable for studying the effect of the internal nuclear structure as the effect is relatively one order of magnitude larger, all the while ε_{BR} is only half the absolute value, relegating QED and nuclear polarisation effects down in importance.

2. Magnetic corrections

Let us now analyse the results for the Bohr-Weisskopf correction defined in Eq. (120) and denoted by the quantity ε_{BW} . Figure 20 shows the contributions of the various orbital and spin currents ($j_p^{(\ell)}$, $j_n^{(\ell)}$, $j_p^{(s)}$ and $j_n^{(s)}$) to the ε_{BW} term for the orbitals $1s_{1/2}$ to $4f_{7/2}$ for the two hydrogen-like isotopes $^{161}\text{Dy}^{65+}$ and $^{163}\text{Dy}^{65+}$, in the upper and lower panels respectively.

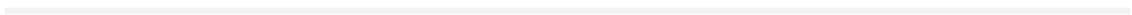
We can clearly see that for all orbitals of both isotopes, the dominant contribution is provided by the neutron spin current. In accordance with preceding discussions, this observation can be attributed to both isotopes having an even number of paired protons and a single unpaired neutron. Moreover, all of the corrections provided by this current are positive, despite the two isotopes

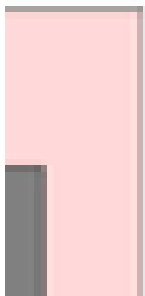
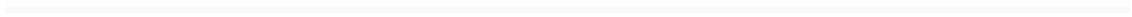
having magnetic moments of opposite signs. The correction terms increase positively since the absolute magnitudes in the denominators all decrease in size. We also observe that for both isotopes the two proton contributions, induced by the aforementioned neutron currents, are negative and that the contribution associated with the orbital motion is almost non-existent. This leads us to conclude that it is the nuclear magnetism due to the spins of the nucleons that acts on the atomic electrons through the hyperfine interaction. The strongest corrections affect the s orbitals, which penetrate deeper into the nucleus. The total correction is around 2%, which is far from negligible. Finally, another noteworthy comparison between the two isotopes is that the magnitudes of the spin contributions of protons and neutrons are larger for ^{163}Dy than for ^{161}Dy . However, since the proton contributions are positive while the neutron contributions are negative, we can see that the total correction remains approximately unchanged.

Figure 21 is similar to Fig. 20, but for a muonic ion. As expected, the main difference is the very significant increase in the value of the quantities studied. Indeed, the correction is increased by a factor of 50 compared with the electronic case and is of the same order as that obtained from the calculation without correction (i.e. close to 100%), consistent with the order of magnitude calculated for other elements [89]. Moreover, these results fall within the same order of magnitude as recent experimental results for neighbouring lanthanides, providing corroborating evidence for our calculations [28]. Overall, the conclusions are the same as for the electronic case, although there is one significant difference: the $np_{1/2}$ orbitals are just as strongly affected as the $ns_{1/2}$ orbitals. As in the case of the electron, we can see that it is the nuclear magnetism induced by the spins of the nucleons that acts on the atomic muons through the hyperfine interaction.

Figure 22 shows the BR and BW corrections on the same graph for the two isotopes as a function of the principal quantum number n for the $s_{1/2}$, $p_{1/2}$ and $p_{3/2}$ orbitals. Isotopic effects are very small. They can only be observed for the BW correction and the $s_{1/2}$ and $p_{1/2}$ orbitals. The behaviour of ε_{BR} and ε_{BW} as a function of n is almost constant from $n = 2$ onward.

Figure 23 is similar to Fig. 22, but for a muonic ion. As expected, the isotopic effects are greater than in the electronic case, particularly for the $p_{1/2}$ orbitals. In contrast to the electronic case, the values of the BR and BW corrections are almost similar for the three types of orbitals. This was not the situation for the electrons, where the BR corrections were much larger than those for the BW case. Finally, the behaviour as a function of n is less constant than in the electronic case, with significant variation for small values of n .





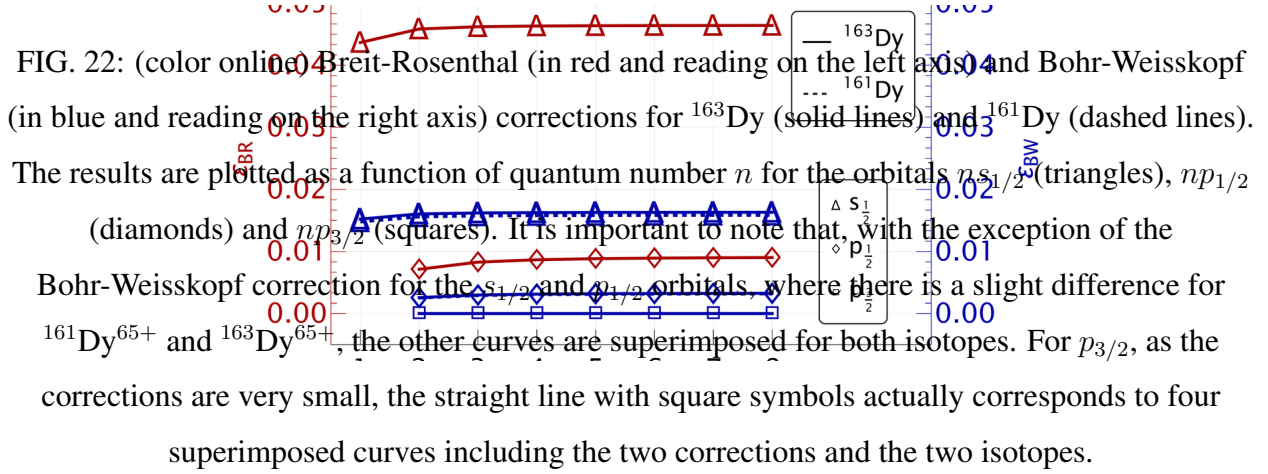


FIG. 23: (color online) Same as Fig. 22 but for muonic hydrogen-like ions.

3. Hyperfine anomaly

The hyperfine anomaly for both dysprosium isotopes is shown in Fig. 24, where both electronic and muonic cases are shown on the same graph. As expected, the hyperfine anomaly is most prominent in the $j = 1/2$ states, and especially the s states, showcasing the importance of the Fermi contact term [90]. For example, for the s orbitals of muonic ions, we can reach values of Δ_{163}^{161} larger than 10%. Moreover, it is still of the order of 1% for $j = 3/2$ states in the muonic case, whereas it is practically nonexistent for the electronic case in this situation, demonstrating the increased sensitivity of the muonic ions to the internal nuclear structure beyond the Fermi contact term.

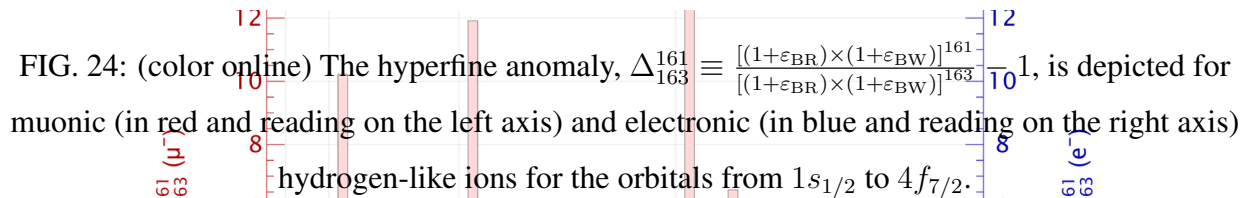
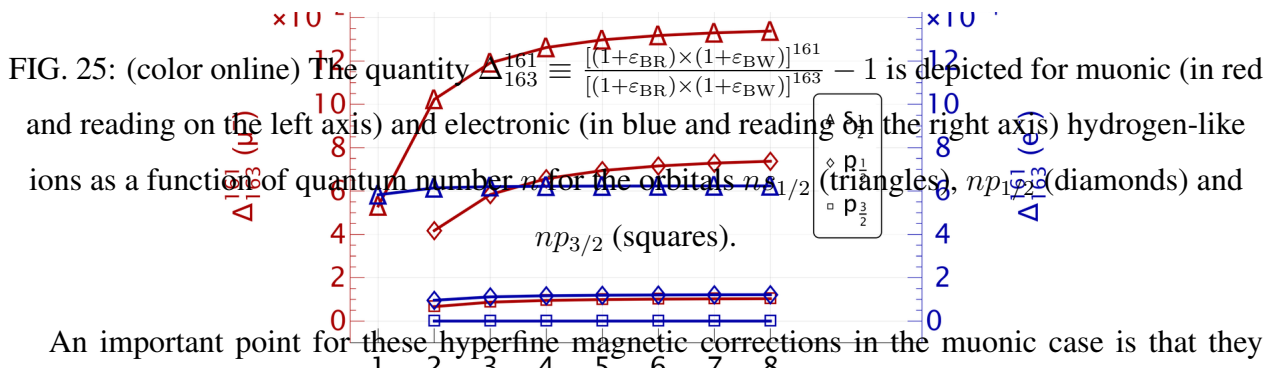


Figure 25 shows the hyperfine anomaly as a function of the principal quantum number n again for the electronic as well as the muonic case. It can be seen that for muonic ions the value of Δ_{163}^{161} increases with n and reaches a plateau for $n > 6$ whereas the behaviour is effectively constant for electronic ions. This result gives credence to the customary assumption that the Fermi contact term and hence the hyperfine anomaly is n -independent. However, for muonic ions, it becomes apparent

that the hyperfine anomaly is heavily dependent on n , with e.g. the anomaly for the $1s_{1/2}$ state being of the order of 5%, less than half of that for $n \geq 2$. Given that a lot of muonic studies focus near the ground $1s_{1/2}$ state [90, 91], this observation indicates that simply importing the electronic-atom intuition to the muonic sector can lead to sizeable systematic biases when extracting nuclear properties from hyperfine data. More precisely, any analysis that constrains nuclear magnetisation radii or higher-order nuclear moments using only (or predominantly) $1s_{1/2}$ muonic transitions may underestimate the impact of nuclear-structure effects on levels with larger n . This is particularly relevant when extracting the hyperfine anomaly from s - s transitions, as in the electronic case. [92]. This n -dependence needs to be taken into account.

Furthermore, these results demonstrate the relevance of our model for the first-principles calculation of the Fermi contact term for specific shells, which is commonly treated as a free parameter extracted from experimental data.



An important point for these hyperfine magnetic corrections in the muonic case is that they become significantly larger than QED and nuclear polarisation corrections to the hyperfine constant, which were calculated to be only around 0.1% of that of the Bohr-Weisskopf correction [89] for example. This means that experimentally obtained hyperfine anomalies mainly only originate from the finite size effects.

4. Correction of the quadrupole term

In the following we will discuss the results obtained for the hyperfine quadrupole term given by the formulas Eq. (116) and Eq. (117). Figure 26 shows the three quantities introduced in ?? III D 4 c.

For ΔB^m , defined in Eq. (132) and shown in the upper panel of the figure, we see that: (i) the four models give almost identical results; (ii) The $np_{3/2}$ orbitals make by far the largest contribution and; (iii) for $m = \text{pt}$, ΔB^{pt} quantifies the quadrupole moment correction due to penetration into the nucleus. This is of the order of 0.006% for the $np_{3/2}$ orbitals. Let us recall that the $s_{1/2}$ and $p_{1/2}$

contributions to the quadrupole term are identically zero due to spherical symmetry of the orbital wavefunctions.

In the lower panel of the figure we have plotted ΔB , which measures the relative deviation between the results of the microscopic model and those from the nuclear model with a Fermi distribution, which is the most accurate of the non-microscopic models. We can clearly see that the relative difference is extremely small, of the order of $10^{-6}\%$. So the use of a simple model like that of Fermi is well-suited to this situation. Let us point out that the choice of nuclear model only affects the electronic wavefunctions that appear in the integral used to define the quadrupole constant (b) of Eq. (116). In that same integral, the nuclear charge distribution must always be taken from the HFBCS calculation, because the other empirical nuclear models considered here are by definition spherically symmetric. As a consequence, ΔB does not have a sound physical definition; it is introduced solely as a numerical benchmark to test whether one really needs to solve the Dirac equation with the full HFBCS nuclear structure, or whether it is sufficient to use the HFBCS charge distribution only in the post-processing stage, together with atomic wavefunctions obtained from a simpler nuclear model.

The lower panel also shows ΔB_{161}^{163} which measures the isotopic effect on the hyperfine quadrupolar correction. This quantity is calculated using the most sophisticated nuclear model (HFBCS) and includes the quadrupole moment correction due to the penetration into the nucleus (i.e. $b = b_{\text{wp}}^{\text{hf}}$). It is interesting to see that this quantity is virtually constant (at 4%) across all the electronic orbitals presented.

For electronic ions, the quadrupole shifts are approximately $10^{-3}\%$ for $p_{3/2}$ states, which is considerably larger than the dipole corrections (BR and BW) for the same states. Moreover, the quadrupole contribution to the hyperfine splitting of the $2p_{3/2}$ state (transition $F = 4 \rightarrow F = 3$) in $^{163}\text{Dy}^{65+}$ is around 24 meV, nearly eight times larger than the dipole contribution (≈ 3 meV). Nonetheless, this quadrupole shift of $10^{-3}\%$ of the total transition energy is still difficult to measure for electronic ions, as it would amount to a difference of the order of ≈ 10 meV.

In contrast, the quadrupole shifts for the muonic orbitals of $^{163}\text{Dy}^{65+}(\mu^-)$, as seen in Fig. 27, are much larger: around 50% for $p_{3/2}$ states, 5 to 10% for $d_{3/2}$ states, and 5% for $d_{5/2}$ states. These values can be compared to the magnetic hyperfine corrections for the same states, which are between 1% and 2%. Here, the quadrupole contribution to the hyperfine splitting of the $2p_{3/2}$ state in the muonic ion is of the order of hundreds of keV, consistent with experimental data [28, 93, 94],

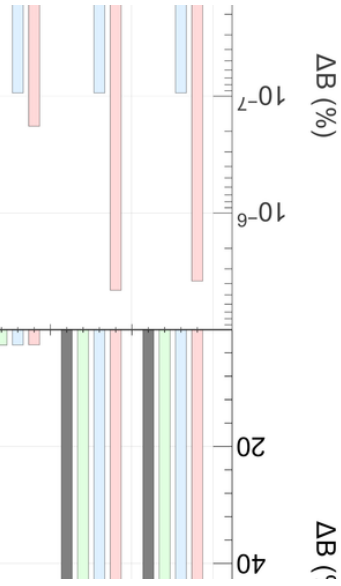


FIG. 26: (color online) Quadrupole shifts for electronic $^{163}\text{Dy}^{65+}$. (Upper panel) $\Delta B^m \equiv \frac{b_{\text{np}}^{\text{pt}} - b_{\text{wp}}^m}{b_{\text{np}}^{\text{pt}}}$ with $m \in \{\text{pt}, \text{sp}, \text{fm}, \text{hf}\}$. The subscript indices np and wp represent calculations with no penetration and with penetration, respectively (see text for explanation). (Lower panel) Two quantities are depicted: $\Delta B \equiv \frac{b_{\text{wp}}^{\text{fm}} - b_{\text{wp}}^{\text{hf}}}{B_{\text{wp}}^{\text{fm}}}$ for $^{163}\text{Dy}^{65+}$ (in red and reading on the left axis) and $\Delta B_{161}^{163} \equiv \frac{b_{\text{wp}}^{\text{hf}}(163) - b_{\text{wp}}^{\text{hf}}(161)}{b_{\text{wp}}^{\text{hf}}(161)}$ (in blue and reading on the right axis). Note that the $s_{1/2}$ and $p_{1/2}$ contributions are zero. The results for electronic $^{161}\text{Dy}^{65+}$ are given in the appendix (cf. Fig. 38).

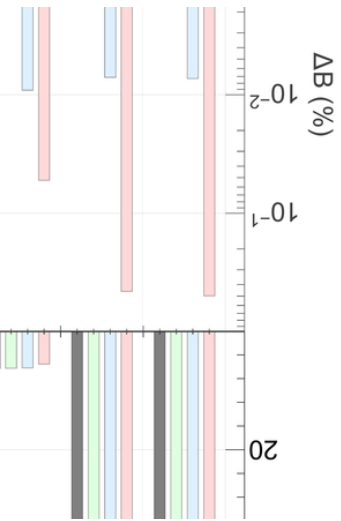


FIG. 27: (color online) Same as Fig. 26 but for muonic $^{163}\text{Dy}^{65+}$. The results for muonic $^{161}\text{Dy}^{65+}$ are given in the appendix (cf. Fig. 39).

and significantly higher than the dipole contribution ($\approx 100s$ eV). Therefore, we may note that the

quadrupole interaction is the dominant factor in the hyperfine splitting of the muonic $2p_{3/2}$ state, making the quadrupole shift measurable in this case, with an energy shift of the order of tens of keV. Recent studies have also concluded that the QED and second-order corrections to the quadrupolar constant in muonic atoms are of the order of $0.1 - 1$ keV [95], placing both the finite size effects and the latter in the same ballpark for their effect on muonic quadrupolar splittings. It is also interesting to compare the shifts between the Fermi and HFBCS models ($\Delta B_{\text{fm}}^{\text{hf}}$) for the muonic ions in the lower panel of Fig. 27, which show an increase of roughly 5 orders of magnitude from the electronic case in Fig. 26. This renders it experimentally relevant, as the corresponding energy shift falls within the experimental precision of the order of eVs [28]. As for the isotopic effect, ΔB_{161}^{163} , we can see the increased sensitivity of the muonic orbitals to the orbital quantum number that was not visible in the electronic case.

As a complement, Fig. 28 illustrates how the penetration of the electronic and muonic wavefunctions into the nucleus of ^{163}Dy affects the quadrupole constant, by comparing the results with those obtained for a point-like quadrupole. The magnitude of this relative difference reflects the significance of finite-size effects on the quadrupole interaction, as opposed to a simplistic point-charge approximation. For the electronic case, the deviation reaches at most about 10^{-4} , rendering it negligible from an experimental standpoint. In contrast, for the muonic configuration, the effect is roughly 10^4 times larger, while the absolute quadrupole interaction itself is also orders of magnitude greater, making it a quantitatively relevant contribution.

As observed in Figs. 26 and 27, the relative difference of the quadrupole constant between the two dysprosium isotopes is effectively constant around 4%, with deviations from that value becoming more apparent in the muonic case. This constant corresponds naturally to the relative difference of the calculated quadrupole constants for the two isotopes.

In order to resolve the finer changes due to the internal nuclear structure, a quantity similar to the magnetic hyperfine anomaly can be defined, namely the quadrupole hyperfine anomaly. The latter is further calculated for both electronic and muonic ions, as defined by

$${}_Q\Delta_B^A \equiv \frac{b(A)}{b(B)} \frac{Q_0^{(2),(\text{spec})}(B)}{Q_0^{(2),(\text{spec})}(A)} - 1, \quad (144)$$

where $b(A)$ and $b(B)$ are the quadrupole hyperfine constants for isotopes A and B , $Q_0^{(2),(\text{spec})}(A)$ and $Q_0^{(2),(\text{spec})}(B)$ are their respective nuclear quadrupole moments.

Unlike the magnetic hyperfine anomaly, the quadrupole anomaly does not need to be decom-

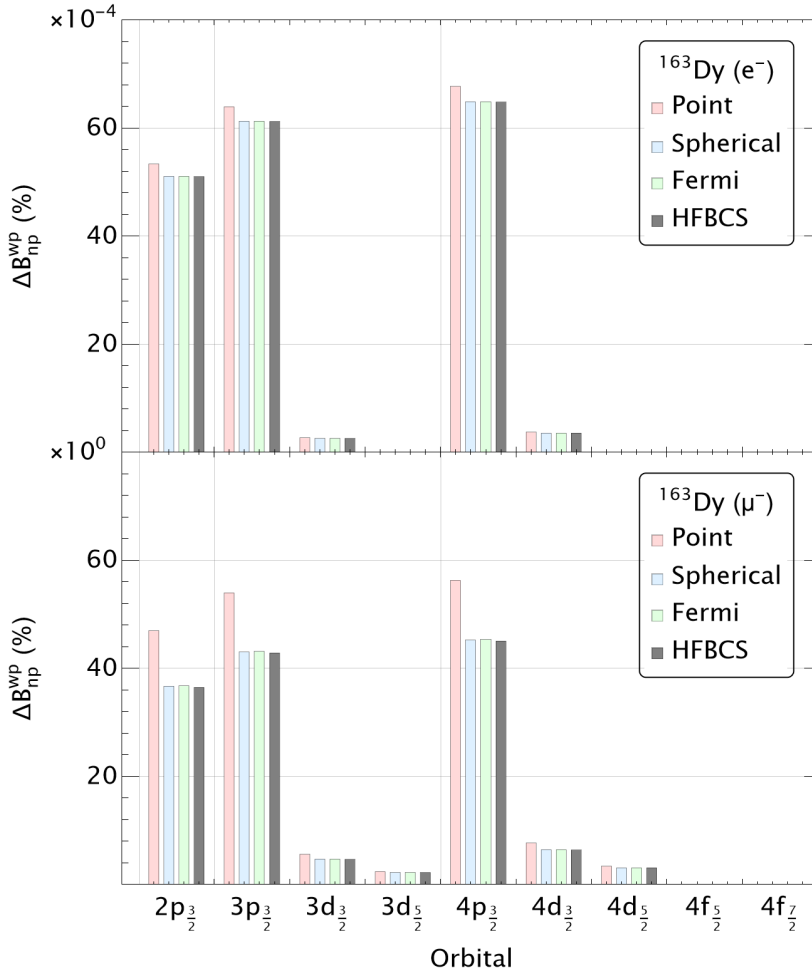
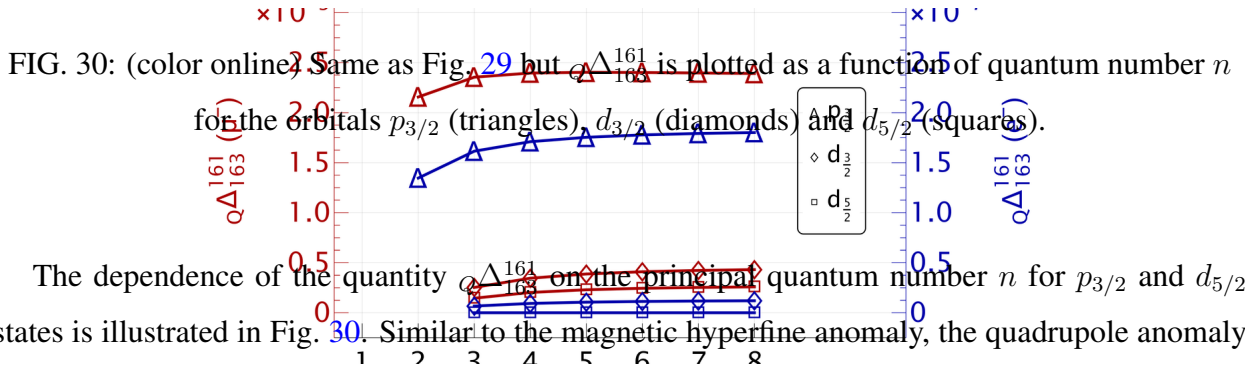


FIG. 28: (color online) Relative change of the quadrupole constant $\Delta B_{np}^{wp} \equiv \frac{b_{wp} - b_{np}}{b_{np}}$ for each model (pt, sp, fm, hf) calculated with penetration (wp) and with no penetration (np) for electronic (Upper panel) and muonic (Lower panel) $^{163}\text{Dy}^{65+}$, respectively. Note that the $s_{1/2}$ and $p_{1/2}$ contributions are zero.

FIG. 29: (color online) The ratio by isotope of the shift in quadrupole moment from the simplest (np, pt) to most complex (wp, hf) model is defined by: $Q\Delta_{163}^{161} = \frac{\Delta B(161)}{\Delta B(163)} - 1$ where $\Delta B(A) \equiv \frac{b_{wp}^{hf}(A)}{b_{np}^{pt}(A)}$. Results for the electronic and muonic ions are shown in blue and red, with readings on the right and left axes respectively. Note that the $s_{1/2}$ and $p_{1/2}$ contributions are zero.

posed into two separate contributions. The magnetic anomaly arises from both (i) the finite nuclear charge distribution and (ii) the finite nuclear current (magnetisation) distribution, whereas

the quadrupole anomaly is sourced solely by the finite charge distribution. As shown in Figs. 29 and 30, our results suggest that the anomaly is of the order of 10^{-7} for the electronic ion and 10^{-3} for the muonic ion. Coupled with the much larger quadrupole hyperfine interaction in the muonic case, this makes the quadrupole hyperfine anomaly observable for the muonic ion but not for the electronic ion.



The dependence of the quantity $\alpha\Delta_{163}^{161}$ on the principal quantum number n for $p_{3/2}$ and $d_{5/2}$ states is illustrated in Fig. 30. Similar to the magnetic hyperfine anomaly, the quadrupole anomaly is fairly constant with n , with a slight dip for the $2p_{3/2}$ state. The behaviour is consistent across both electronic and muonic ions, aside from the difference of four orders of magnitude.

5. Remark regarding the choice of the empirical nuclear radius

As a last remark, we would like to point out the impact that the choice of R_{rms} (and consequently $R_{\text{N}} = \sqrt{\frac{5}{3}R_{\text{rms}}^2}$) has on the computed results. For example, instead of using the empirical formula $R_{\text{rms}} = (0.836A^{1/3} + 0.57)$ fm [73], the root-mean-square radius ($R_{\text{rms}} = \sqrt{\langle R^2 \rangle}$) of both the uniform spherical distribution and the Fermi distribution of Eq. (94) can be redefined to match the R_{rms} of the HFBCS model. The results are shown in Appendix VIII D. Once all charge distributions are renormalised to the HFBCS R_{rms} , the electronic binding energies from the Fermi and HFBCS models agree at the level of $10^{-6}\%$, so that R_{rms} essentially fixes the spectrum and a renormalised Fermi model is sufficient [73]. For the electronic ion, this means that the HFBCS value of R_{rms} obtained via our method effectively encapsulates the nuclear model and can be used as the sole nuclear-structure input in the atomic calculations, providing a computationally simplified implementation of our approach. In contrast, for muonic ions residual differences of order $10^{-3}\%$ remain, showing that their energy levels are sensitive to nuclear-structure details beyond R_{rms} and thus still provide a valuable probe for discriminating between different nuclear models.

V. CONCLUSIONS

In this work we have presented a comprehensive microscopic treatment of hyperfine interactions in heavy hydrogen-like ions, explicitly bridging nuclear and atomic length scales within a single, internally consistent framework. Starting from self-consistent nuclear structure calculations within the Skyrme–Hartree–Fock framework supplemented with BCS pairing and self-consistent blocking, we obtained, via this microscopic approach involving a quantum-mechanical treatment of the structure of the nucleus, proton and neutron densities and currents for the prolate deformed rare-earth nuclei ^{159}Tb , ^{161}Dy , ^{163}Dy , and ^{165}Ho . These microscopic densities provide the source terms for a multipole expansion of the nuclear electric and magnetic fields entering the Dirac equation for a bound electron or muon. By solving the Dirac equation with finite-size nuclear potentials, we analysed finite-size effects for both charge (Breit–Rosenthal) and current/magnetisation (Bohr–Weisskopf) corrections to hyperfine structure constants. At the same time, the same nuclear quantities that reproduce measured spectroscopic quadrupole and magnetic dipole moments were employed directly to compute hyperfine splittings and hyperfine anomalies between the two dysprosium isotopes, providing a unified approach in which atomic and nuclear ingredients are treated on equal footing.

The Skyrme–HF+BCS calculations predict substantially prolate deformed shapes for all nuclei studied here. Proton and neutron densities exhibit significant differences in the nuclear interior, reflecting underlying shell structure. The corresponding current densities show non-trivial loop structures that depend on the occupancy of valence orbitals. In ^{161}Dy and ^{163}Dy , the unpaired neutron dominates the intrinsic magnetisation, whereas in ^{159}Tb and ^{165}Ho it is the unpaired proton. Induced currents in the even–even core, caused by the breaking of time-reversal symmetry generated by the unpaired nucleon, are an order of magnitude smaller, but contribute with opposite sign, highlighting the importance of core polarisation and demonstrating that a realistic Bohr–Weisskopf correction must resolve the underlying nucleonic current components.

When these microscopic densities are used as inputs to the Dirac equation for hydrogen-like electronic ions, finite-size effects on the electronic wave functions are moderate. Breit–Rosenthal charge corrections to the magnetic hyperfine constant a are at the level of a few percent for $ns_{1/2}$ states and are much smaller for $np_{1/2}$ states, consistent with the relativistic contact-density systematics. Bohr–Weisskopf corrections are dominated by spin currents: the neutron spin current

provides the leading contribution to a in Dy isotopes, while induced proton spin and orbital currents give smaller, often opposite, contributions. For the electronic ions considered here the net BW correction is at the 2 % level, while the resulting hyperfine anomalies (vanishing for a point-like nucleus) remain below 10^{-4} for electronic states. These findings reinforce the broader point that, with the ever-improving precision of modern experimental platforms, nuclear magnetisation and charge distributions must be included consistently alongside relativistic atomic structure to avoid biased extraction of nuclear moments from spectroscopic data.

The situation changes dramatically for muonic ions, where the Bohr radius is much smaller and the lepton wave function has substantial overlap with the nuclear interior. Finite-size corrections become decisive: the BR correction exceeds 40 % for the $1s_{1/2}$ muon orbital and the BW correction approaches 100 % for s -states. Hyperfine anomalies can exceed 10 % for muonic s -states and reach the 10^{-4} level in quadrupole interactions. These large anomalies trace directly to the radial overlap of the muon wave function with the nuclear currents, turning muonic spectroscopy into a highly sensitive probe of the spatial distribution of nuclear magnetisation and charge. This enhanced sensitivity is precisely what makes muonic ions an exceptional tool to benchmark microscopic nuclear models. Because the muon samples the nuclear interior, the dominant contributions to the muonic hyperfine splittings depend on the *radial profiles* of the charge density and magnetisation density rather than only on their integrated moments. In practice, different nuclear structure descriptions that reproduce the same spectroscopic dipole moment and quadrupole moment can still predict measurably different Bohr–Weisskopf and Breit–Rosenthal corrections once folded with the sharply peaked muonic wave functions. The resulting hyperfine anomalies therefore act as differential observables that are directly sensitive to core polarisation, the balance of spin and orbital currents, and the spatial distribution of the valence-nucleon magnetisation. This creates a stringent consistency test: a nuclear model must simultaneously account for electromagnetic moments *and* the muon-weighted overlap integrals that govern the hyperfine shifts. In this sense, systematic measurements of muonic ions on sets of isotopes (and across different muonic orbitals) provide a controlled way to disentangle deformations, single-particle configurations, and induced core currents, offering a powerful discriminator among effective interactions and beyond-mean-field refinements. Moreover, we find that the electric quadrupole interaction—often negligible in electronic hydrogen-like ions—becomes the dominant hyperfine contribution for muonic $p_{3/2}$ and d -states: for $^{163}\text{Dy}^{65+}(\mu^-)$ the quadrupole shift of the $2p_{3/2}$ state is of order 100 keV, dwarfing

the dipole contribution. In all cases, the calculated spectroscopic magnetic dipole moments $\mu_{\text{tot}}^{(\text{spec})}$ and electric quadrupole moments $Q_{20}^{(\text{spec})}$ agree with available experimental data from atomic-beam magnetic resonance measurements, supporting the consistency of the nuclear inputs.

Beyond the specific isotopes studied, the present results highlight a general conclusion: precision hyperfine spectroscopy of heavy ions increasingly demands a genuinely combined atomic–nuclear treatment. Finite magnetisation (Bohr–Weisskopf) and finite-size (Breit–Rosenthal) effects are not small add-ons but leading systematics once one targets high accuracy, particularly in highly charged systems where relativistic enhancement increases sensitivity to the nuclear interior. In this sense, the framework developed here is well aligned with the broader trajectory from early atomic time standards [1] to modern precision platforms, including directions where nuclear structure is central rather than incidental, such as the ^{229}Th low-energy nuclear transition and the nuclear-clock program.

VI. PERSPECTIVES

Our fully microscopic approach demonstrates the feasibility and utility of treating the nucleus and the bound electron or muon within a unified quantum-mechanical framework. By disentangling contributions of different nucleonic currents, quantifying finite-size effects, and predicting hyperfine anomalies for both electronic and muonic systems, we have shown that, in particular, muonic spectroscopy of heavy hydrogen-like ions can provide stringent tests of nuclear models. In particular, the large anomalies and sizeable quadrupole shifts predicted for muonic ions define clear experimental targets capable of discriminating between competing microscopic descriptions of nuclear magnetisation and deformation, especially when combined with isotope-chain systematics and hyperfine-anomaly measurements that help separate electronic-structure and nuclear-distribution effects [14, 15, 17]. Several extensions follow naturally. On the atomic side, incorporating radiative QED corrections and other higher-order effects will enable direct, quantitative confrontation with forthcoming high-precision data in the heaviest systems [18, 21]. On the nuclear side, exploring other effective interactions (e.g. Gogny forces) and systematically comparing EDF parameterisations will refine uncertainty estimates for magnetisation distributions and their induced hyperfine signatures [37, 54, 57]. The formalism can also be generalised to multi-electron ions: specific differences of hyperfine splittings in H-like and Li-like (or other few-electron) ions can

cancel significant electronic correlations and isolate nuclear-structure contributions, providing an experimentally accessible pathway to nuclear magnetisation profiles with reduced atomic-theory systematics [18, 21]. Finally, the same microscopic understanding of hyperfine couplings is increasingly relevant beyond metrology, for example in nuclear-spin and molecular-spin platforms for quantum technologies, where controlling hyperfine interactions and their material dependence is essential [9–11, 20]. Overall, combining high-precision hyperfine spectroscopy—especially in muonic systems—with the kind of microscopic calculations presented here will deepen our understanding of the interplay between atomic and nuclear physics and open new avenues for probing nuclear structure with unprecedented sensitivity.

VII. ACKNOWLEDGEMENTS

This work was funded by the French National Research Agency (ANR) through the Programme d’Investissement d’Avenir under contract ANR-11-LABX-0058 NIE and ANR-17-EURE-0024 within the Investissement d’Avenir program ANR-10-IDEX-0002-02. J-G.H. also acknowledges QUSTEC funding from the European Union’s Horizon 2020 research and innovation program under the Marie Skłodowska-Curie Grant Agreement No. 847471. The authors would like to acknowledge the High Performance Computing Center of the University of Strasbourg for supporting this work by providing scientific support and access to computing resources. Part of the computing resources were funded by the Equipex Equip@Meso project (Programme Investissements d’Avenir) and the CPER Alsacalcul/Big Data. Finally, we are grateful for the helpful discussions with J. Meyer.

VIII. APPENDICES

A. Intrinsic vs. spectroscopic multipole moments

1. General expressions

The components of the spectroscopic multipole moment operators $\mathcal{M}_\lambda^{(\text{spec})}$ of rank λ (expressed in the laboratory reference frame), are related to the components of the intrinsic multipole moment operators $\mathcal{M}_\lambda^{(\text{intr})^{(\theta)}}$ (expressed in the reference frame of the nucleus) via the well known formula

for spherical tensor operators [96]

$$\mathcal{M}_{\lambda\mu}^{(\text{spec})} = \sum_{\nu=-\lambda}^{\lambda} \mathcal{D}_{\mu\nu}^{\lambda*}(\theta) \mathcal{M}_{\lambda\nu}^{(\text{intr})(\theta)}, \quad (145)$$

where $\mathcal{D}_{\mu\nu}^{\lambda}(\theta)$ represents the Wigner functions at Euler angles $\theta = (\alpha, \beta, \gamma)$ [96], specifying the orientation of the intrinsic frame with respect to the laboratory frame.

In the framework of the nuclear collective model, the total Hamiltonian H of the nuclear system is composed of a collective H_{Coll} , and an intrinsic part H_{intr}

$$H = H_{\text{Coll}} + H_{\text{intr}}. \quad (146)$$

The collective part of the Hamiltonian reads

$$H_{\text{Coll}} = \sum_{k=1}^3 \frac{\hbar^2}{2\mathcal{J}_k} \mathfrak{R}_k^2, \quad (147)$$

where $k = 1, 2, 3$ label the intrinsic axes, and $\vec{\mathfrak{R}}$ represents the angular momentum of the core, considered as a quantum rotor and \mathcal{J}_k are the components of the inertia tensor.

The total spin \vec{I} of the nucleus is obtained by coupling the core angular momentum $\vec{\mathfrak{R}}$ with the intrinsic angular momentum \vec{J} , i.e.

$$\vec{I} = \vec{\mathfrak{R}} + \vec{J}. \quad (148)$$

Reverting this expression to $\vec{\mathfrak{R}} = \vec{I} - \vec{J}$, one easily obtains

$$H_{\text{Coll}} = \sum_{k=1}^3 \frac{\hbar^2}{2\mathcal{J}_k} I_k^2 - \sum_{k=1}^3 \frac{\hbar^2}{\mathcal{J}_k} I_k J_k + \sum_{k=1}^3 \frac{\hbar^2}{2\mathcal{J}_k} J_k^2. \quad (149)$$

In this expression, the first term in the right member is usually called the rotation Hamiltonian H_{Rot} , the second is the (Coriolis) coupling term H_{Coupl} , and the last term is called the recoil term H_{Recoil} . The recoil term acts on the intrinsic degrees of freedom, and is therefore usually incorporated in the intrinsic part of the Hamiltonian.

Assuming adiabaticity (the intrinsic structure follows intimately the rotational motion of the core) will allow for expressing the total nuclear wave functions essentially as a product of an intrinsic and a rotational wave function. This means that the coupling term H_{Coupl} can be ignored. Stretching effects due to centrifugal forces will also be neglected, so that it will be sufficient to only consider H_{Rot} .

Furthermore we will assume axial symmetry of the intrinsic Hamiltonian. This assumption leads to the fact that K , the projection of the total angular momentum \vec{I} on the symmetry axis of the nucleus (chosen as the “3” axis), is a good quantum number. Note that since the system (the nucleus) is isolated in space, the total angular momentum is always conserved because of isotropy in space (the total Hamiltonian is rotationally invariant), thus I is a good quantum number. Also, its projection onto the “ z ” laboratory axis, the quantum number M , is a good quantum number as well. For the rotational part, H_{Rot} , axial symmetry of the nuclear shape leads to the symmetric-rotor case $\mathcal{J}_1 = \mathcal{J}_2 \equiv \mathcal{J}$. We will not consider the third component $\frac{\hbar^2}{2\mathcal{J}_3} I_3^2$ in H_{Rot} since states that would be rotated around the 3-axis cannot be distinguished in a collective rotation (it is meaningless to speak about a rotation of a quantum core about its symmetry axis, just like it would be impossible, for a macroscopic object with a carefully polished surface, to distinguish optically a rotation about such an axis). Also, the angular momentum vector of the core, $\vec{\mathfrak{R}}$, is perpendicular to the symmetry axis. We consider therefore

$$H_{\text{Rot}} = \sum_{k=1}^2 \frac{\hbar^2}{2\mathcal{J}} I_k^2 = \frac{\hbar^2}{2\mathcal{J}} (I^2 - I_3^2). \quad (150)$$

We will also assume that the intrinsic Hamiltonian is invariant with respect to a rotation of 180° around an axis perpendicular to its symmetry axis. Conventionally, we use this axis to be the intrinsic “2” axis (all axes perpendicular to the symmetry axis being, in this respect, equivalent). This assumption leads to the fact that states with $K \neq 0$ are doubly degenerate. In the following, and if not otherwise stated, we will use only positive values of K ($K \geq 0$).

We shall use in the following the normalised and symmetrised wave functions, as given, e.g., in Ref. [97, 98] (ξ denotes the set of intrinsic variables):

$$\begin{aligned} \langle \alpha\beta\gamma; \xi | \widetilde{IMK} \rangle \equiv \psi_{MK}^I = & \frac{1}{\sqrt{2(1 + \delta_{K0})}} \sqrt{\frac{2I + 1}{8\pi^2}} \left\{ \mathcal{D}_{MK}^{I*}(\alpha\beta\gamma) \Phi_K(\xi) \right. \\ & \left. + (-)^{I+K} \mathcal{D}_{M-K}^{I*}(\alpha\beta\gamma) \Phi_{\bar{K}}(\xi) \right\}; \quad K \geq 0. \end{aligned} \quad (151)$$

In this expression we have introduced the intrinsic wave functions Φ_K and $\Phi_{\bar{K}}$ according to their development onto a basis of good intrinsic angular momentum [98]:

$$\Phi_K = \sum_J C_J \Phi_{JK} \quad (152)$$

and

$$\Phi_{\bar{K}} \equiv \mathcal{R}_i^{-1} \Phi_K \equiv e^{i\pi J_2} \Phi_K = \sum_J (-)^{J+K} C_J \Phi_{J,-K}. \quad (153)$$

We use the same notation as Bohr and Mottelson [98] for the operator describing a rotation by the angle π around the “2” axis, namely $\mathcal{R}_i \equiv e^{-i\pi J_2}$.

In what follows, we will also make use of the ket notation

$$|\bar{K}\rangle = \mathcal{R}_i^{-1} |K\rangle = \mathcal{R}_i^\dagger |K\rangle. \quad (154)$$

Moreover when using symmetrised bras and kets as in Eq. (151), these will be specified with a tilda symbol. If they are not symmetrised, the tilda symbol is omitted.

Further notations are used, for normalised wave functions (depending on whether they are symmetrised or not, and whether one adds intrinsic wave functions or not) :

$$\langle \alpha\beta\gamma | IMK \rangle \equiv \sqrt{\frac{2I+1}{8\pi^2}} \mathcal{D}_{MK}^{I*}(\alpha\beta\gamma), \quad (155)$$

$$\langle \alpha\beta\gamma; \xi | IMK \rangle \equiv \sqrt{\frac{2I+1}{8\pi^2}} \mathcal{D}_{MK}^{I*}(\alpha\beta\gamma) \Phi_K(\xi), \quad (156)$$

$$\langle \alpha\beta\gamma | \widetilde{IMK} \rangle = \frac{1}{\sqrt{2(1+\delta_{K0})}} \sqrt{\frac{2I+1}{8\pi^2}} \left\{ \mathcal{D}_{MK}^{I*}(\alpha\beta\gamma) + (-)^{I+K} \mathcal{D}_{M-K}^{I*}(\alpha\beta\gamma) \right\}, \quad (157)$$

and for the kets we use

$$|\widetilde{IMK}\rangle \equiv \frac{1}{\sqrt{2(1+\delta_{K0})}} \left\{ |IMK\rangle + (-)^{I+K} |IM-K\rangle \right\}; \quad K \geq 0. \quad (158)$$

Using Eq. (145) and integrating over all possible orientations of the intrinsic reference frame (i.e. integrating over Euler angles), one can evaluate the matrix elements of the multipole moment operator as

$$\begin{aligned} \langle \widetilde{I_2 M_2 K_2} | \mathcal{M}_{\lambda\mu}^{(\text{spec})} | \widetilde{I_1 M_1 K_1} \rangle &= \sum_{\nu=-\lambda}^{\lambda} \int d\theta \langle \widetilde{I_2 M_2 K_2} | \mathcal{D}_{\mu\nu}^{\lambda*}(\theta) \mathcal{M}_{\lambda\nu}^{(\text{intr})}(\theta) | \widetilde{I_1 M_1 K_1} \rangle \\ &= \frac{1}{\sqrt{2(1+\delta_{K_1 0})} \sqrt{2(1+\delta_{K_2 0})}} \sum_{\nu=-\lambda}^{\lambda} \left[(a)_\nu + (-)^{I_2+K_2} (b)_\nu \right. \\ &\quad \left. + (-)^{I_1+K_1} (c)_\nu + (-)^{I_1+K_1} (-)^{I_2+K_2} (d)_\nu \right]. \end{aligned} \quad (159)$$

In this expression one has

$$\begin{aligned} (a)_\nu &= \langle K_2 | \mathcal{M}_{\lambda\nu}^{(\text{intr})}(\theta) | K_1 \rangle \int d\theta \langle I_2 M_2 K_2 | \theta \rangle \mathcal{D}_{\mu\nu}^{\lambda*}(\theta) \langle \theta | I_1 M_1 K_1 \rangle \\ &= \langle K_2 | \mathcal{M}_{\lambda\nu}^{(\text{intr})}(\theta) | K_1 \rangle \sqrt{\frac{2I_1+1}{8\pi^2}} \sqrt{\frac{2I_2+1}{8\pi^2}} \int d\theta \mathcal{D}_{M_2 K_2}^{I_2}(\theta) \mathcal{D}_{\mu\nu}^{\lambda*}(\theta) \mathcal{D}_{M_1 K_1}^{I_1*}(\theta), \end{aligned} \quad (160)$$

which can be evaluated using the formula [96]

$$\int d\theta \mathcal{D}_{M_3 K_3}^{I_3}(\theta) \mathcal{D}_{M_2 K_2}^{I_2^*}(\theta) \mathcal{D}_{M_1 K_1}^{I_1^*}(\theta) = \frac{8\pi^2}{2I_3 + 1} (I_1 M_1 I_2 M_2 | I_3 M_3) (I_1 K_1 I_2 K_2 | I_3 K_3). \quad (161)$$

As a result, the term $(a)_\nu$ can be written as

$$(a)_\nu = \langle K_2 | \mathcal{M}_{\lambda\nu}^{(\text{intr})}(\theta) | K_1 \rangle \sqrt{2I_1 + 1} \frac{(I_1 M_1 \lambda \mu | I_2 M_2)}{\sqrt{2I_2 + 1}} (I_1 K_1 \lambda \nu | I_2 K_2). \quad (162)$$

In a very similar way, we get for the other terms :

$$(b)_\nu = \langle \bar{K}_2 | \mathcal{M}_{\lambda\nu}^{(\text{intr})}(\theta) | K_1 \rangle \sqrt{2I_1 + 1} \frac{(I_1 M_1 \lambda \mu | I_2 M_2)}{\sqrt{2I_2 + 1}} (I_1 K_1 \lambda \nu | I_2 - K_2), \quad (163)$$

and

$$(c)_\nu = \langle K_2 | \mathcal{M}_{\lambda\nu}^{(\text{intr})}(\theta) | \bar{K}_1 \rangle \sqrt{2I_1 + 1} \frac{(I_1 M_1 \lambda \mu | I_2 M_2)}{\sqrt{2I_2 + 1}} (I_1 - K_1 \lambda \nu | I_2 K_2), \quad (164)$$

and finally

$$(d)_\nu = \langle \bar{K}_2 | \mathcal{M}_{\lambda\nu}^{(\text{intr})}(\theta) | \bar{K}_1 \rangle \sqrt{2I_1 + 1} \frac{(I_1 M_1 \lambda \mu | I_2 M_2)}{\sqrt{2I_2 + 1}} (I_1 - K_1 \lambda \nu | I_2 - K_2). \quad (165)$$

Grouping these results together, one obtains

$$\begin{aligned} \langle \widetilde{I_2 M_2 K_2} | \mathcal{M}_{\lambda\mu}^{(\text{spec})} | \widetilde{I_1 M_1 K_1} \rangle &= \frac{1}{2} \sqrt{\frac{2I_1 + 1}{(1 + \delta_{K_1 0})(1 + \delta_{K_2 0})}} \frac{(I_1 M_1 \lambda \mu | I_2 M_2)}{\sqrt{2I_2 + 1}} \\ &\times \sum_{\nu=-\lambda}^{\lambda} \left[(I_1 K_1 \lambda \nu | I_2 K_2) \langle K_2 | \mathcal{M}_{\lambda\nu}^{(\text{intr})}(\theta) | K_1 \rangle \right. \\ &+ (-)^{I_2 + K_2} (I_1 K_1 \lambda \nu | I_2 - K_2) \langle \bar{K}_2 | \mathcal{M}_{\lambda\nu}^{(\text{intr})}(\theta) | K_1 \rangle \\ &+ (-)^{I_1 + K_1} (I_1 - K_1 \lambda \nu | I_2 K_2) \langle K_2 | \mathcal{M}_{\lambda\nu}^{(\text{intr})}(\theta) | \bar{K}_1 \rangle \\ &\left. + (-)^{I_1 + K_1} (-)^{I_2 + K_2} (I_1 - K_1 \lambda \nu | I_2 - K_2) \langle \bar{K}_2 | \mathcal{M}_{\lambda\nu}^{(\text{intr})}(\theta) | \bar{K}_1 \rangle \right]. \end{aligned} \quad (166)$$

Now, on the other hand, one has directly

$$\begin{aligned}
\langle \widetilde{I_2 M_2 K_2} | \mathcal{M}_{\lambda\mu}^{(\text{spec})} | \widetilde{I_1 M_1 K_1} \rangle &= \frac{1}{2} \frac{1}{\sqrt{(1 + \delta_{K_1 0})(1 + \delta_{K_2 0})}} \\
&\times \left[\langle I_2 M_2 K_2 | \mathcal{M}_{\lambda\mu}^{(\text{spec})} | I_1 M_1 K_1 \rangle \right. \\
&+ (-)^{I_2 + K_2} \langle I_2 M_2 - K_2 | \mathcal{M}_{\lambda\mu}^{(\text{spec})} | I_1 M_1 K_1 \rangle \\
&+ (-)^{I_1 + K_1} \langle I_2 M_2 K_2 | \mathcal{M}_{\lambda\mu}^{(\text{spec})} | I_1 M_1 - K_1 \rangle \\
&\left. + (-)^{I_1 + K_1} (-)^{I_2 + K_2} \langle I_2 M_2 - K_2 | \mathcal{M}_{\lambda\mu}^{(\text{spec})} | I_1 M_1 - K_1 \rangle \right], \tag{167}
\end{aligned}$$

which can be transformed using the Wigner-Eckart theorem

$$\langle I_2 M_2 K_2 | \mathcal{M}_{\lambda\mu}^{(\text{spec})} | I_1 M_1 K_1 \rangle = \frac{(-1)^{2\lambda}}{\sqrt{2I_2 + 1}} (I_1 M_1 \lambda \mu | I_2 M_2) \langle I_2 K_2 || \mathcal{M}_{\lambda}^{(\text{spec})} || I_1 K_1 \rangle \tag{168}$$

into (note that since λ is integer here, we have $(-1)^{2\lambda} = 1$)

$$\begin{aligned}
\langle \widetilde{I_2 M_2 K_2} | \mathcal{M}_{\lambda\mu}^{(\text{spec})} | \widetilde{I_1 M_1 K_1} \rangle &= \frac{1}{2} \frac{1}{\sqrt{(1 + \delta_{K_1 0})(1 + \delta_{K_2 0})}} \frac{(I_1 M_1 \lambda \mu | I_2 M_2)}{\sqrt{2I_2 + 1}} \\
&\times \left[\langle I_2 K_2 || \mathcal{M}_{\lambda}^{(\text{spec})} || I_1 K_1 \rangle \right. \\
&+ (-)^{I_2 + K_2} \langle I_2 - K_2 || \mathcal{M}_{\lambda}^{(\text{spec})} || I_1 K_1 \rangle \\
&+ (-)^{I_1 + K_1} \langle I_2 K_2 || \mathcal{M}_{\lambda}^{(\text{spec})} || I_1 - K_1 \rangle \\
&\left. + (-)^{I_1 + K_1} (-)^{I_2 + K_2} \langle I_2 - K_2 || \mathcal{M}_{\lambda}^{(\text{spec})} || I_1 - K_1 \rangle \right]. \tag{169}
\end{aligned}$$

Furthermore, one has by definition

$$\begin{aligned}
\langle \widetilde{I_2 K_2} || \mathcal{M}_{\lambda}^{(\text{spec})} || \widetilde{I_1 K_1} \rangle &\equiv \frac{1}{2} \frac{1}{\sqrt{(1 + \delta_{K_1 0})(1 + \delta_{K_2 0})}} \\
&\times \left[\langle I_2 K_2 || \mathcal{M}_{\lambda}^{(\text{spec})} || I_1 K_1 \rangle \right. \\
&+ (-)^{I_2 + K_2} \langle I_2 - K_2 || \mathcal{M}_{\lambda}^{(\text{spec})} || I_1 K_1 \rangle \\
&+ (-)^{I_1 + K_1} \langle I_2 K_2 || \mathcal{M}_{\lambda}^{(\text{spec})} || I_1 - K_1 \rangle \\
&\left. + (-)^{I_1 + K_1} (-)^{I_2 + K_2} \langle I_2 - K_2 || \mathcal{M}_{\lambda}^{(\text{spec})} || I_1 - K_1 \rangle \right], \tag{170}
\end{aligned}$$

allowing to write

$$\langle \widetilde{I_2 M_2 K_2} | \mathcal{M}_{\lambda\mu}^{(\text{spec})} | \widetilde{I_1 M_1 K_1} \rangle = \frac{(I_1 M_1 \lambda \mu | I_2 M_2)}{\sqrt{2I_2 + 1}} \langle \widetilde{I_2 K_2} | \mathcal{M}_{\lambda\mu}^{(\text{spec})} | \widetilde{I_1 K_1} \rangle, \quad (171)$$

which can actually be viewed as a generalisation of the Wigner-Eckart theorem for symmetrised states.

We now identify expression Eq. (171) with Eq. (166) to get the reduced laboratory matrix elements expressed with the help of intrinsic matrix elements as :

$$\begin{aligned} \langle \widetilde{I_2 K_2} | \mathcal{M}_{\lambda}^{(\text{spec})} | \widetilde{I_1 K_1} \rangle &= \frac{1}{2} \sqrt{\frac{2I_1 + 1}{(1 + \delta_{K_1 0})(1 + \delta_{K_2 0})}} \\ &\times \sum_{\nu=-\lambda}^{\lambda} \left[(I_1 K_1 \lambda \nu | I_2 K_2) \langle K_2 | \mathcal{M}_{\lambda\nu}^{(\text{intr})(\theta)} | K_1 \rangle \right. \\ &+ (-)^{I_2 + K_2} (I_1 K_1 \lambda \nu | I_2 - K_2) \langle \bar{K}_2 | \mathcal{M}_{\lambda\nu}^{(\text{intr})(\theta)} | K_1 \rangle \\ &+ (-)^{I_1 + K_1} (I_1 - K_1 \lambda \nu | I_2 K_2) \langle K_2 | \mathcal{M}_{\lambda\nu}^{(\text{intr})(\theta)} | \bar{K}_1 \rangle \\ &\left. + (-)^{I_1 + K_1} (-)^{I_2 + K_2} (I_1 - K_1 \lambda \nu | I_2 - K_2) \langle \bar{K}_2 | \mathcal{M}_{\lambda\nu}^{(\text{intr})(\theta)} | \bar{K}_1 \rangle \right]. \end{aligned} \quad (172)$$

Using the selection rules for the Clebsh-Gordan coefficients, since K_1 and K_2 are fixed, the sum over the index ν disappears.

The first coefficient is non zero only for $K_1 + \nu = K_2$, and therefore this imposes $\nu = -K_-$, where $K_- \equiv K_1 - K_2$. The second coefficient is non zero only for $K_1 + \nu = -K_2$, or $\nu = -K_+$, where $K_+ \equiv K_1 + K_2$. In the same way, the third coefficient demands $\nu = K_+$, and finally the last one requires $\nu = K_-$. This leads to the expression

$$\begin{aligned} \langle \widetilde{I_2 K_2} | \mathcal{M}_{\lambda}^{(\text{spec})} | \widetilde{I_1 K_1} \rangle &= \frac{1}{2} \sqrt{\frac{2I_1 + 1}{(1 + \delta_{K_1 0})(1 + \delta_{K_2 0})}} \\ &\times \left[(I_1 K_1 \lambda - K_- | I_2 K_2) \langle K_2 | \mathcal{M}_{\lambda, -K_-}^{(\text{intr})(\theta)} | K_1 \rangle \right. \\ &+ (-)^{I_2 + K_2} (I_1 K_1 \lambda - K_+ | I_2 - K_2) \langle \bar{K}_2 | \mathcal{M}_{\lambda, -K_+}^{(\text{intr})(\theta)} | K_1 \rangle \\ &+ (-)^{I_1 + K_1} (I_1 - K_1 \lambda K_+ | I_2 K_2) \langle K_2 | \mathcal{M}_{\lambda K_+}^{(\text{intr})(\theta)} | \bar{K}_1 \rangle \\ &\left. + (-)^{I_1 + K_1} (-)^{I_2 + K_2} (I_1 - K_1 \lambda K_- | I_2 - K_2) \langle \bar{K}_2 | \mathcal{M}_{\lambda K_-}^{(\text{intr})(\theta)} | \bar{K}_1 \rangle \right]. \end{aligned} \quad (173)$$

We will now demonstrate that the first and the last terms in this expression are identical and, in the same way, that the second and third terms are equal.

For this purpose we shall make use of the following property of the Clebsh-Gordan coefficients [96]:

$$(AaBb|Cc) = (-)^{A+B-C}(A-a B-b|C-c). \quad (174)$$

With the help of this expression and Eq. (154), the last term can be written as

$$\begin{aligned} & (-)^{I_1+K_1}(-)^{I_2+K_2}(-)^{I_1+\lambda-I_2} (I_1K_1\lambda - K_-|I_2K_2)\langle\bar{K}_2|\mathcal{M}_{\lambda K_-}^{(\text{intr})}(\theta)|\bar{K}_1\rangle \\ &= (-)^{I_1+K_1}(-)^{I_2+K_2}(-)^{I_1+\lambda-I_2} (I_1K_1\lambda - K_-|I_2K_2)\langle K_2|\mathcal{R}_i\mathcal{M}_{\lambda K_-}^{(\text{intr})}(\theta)\mathcal{R}_i^\dagger|K_1\rangle. \end{aligned} \quad (175)$$

Now, for any irreducible spherical tensor operator \mathcal{T}_λ , we can write the transformation rule under the action of the unitary transformation \mathcal{R}_i as [99]

$$\begin{aligned} \mathcal{R}_i\mathcal{T}_{\lambda\mu}\mathcal{R}_i^\dagger &= \sum_{\nu} \mathcal{D}_{\nu\mu}^\lambda(0, \pi, 0)\mathcal{T}_{\lambda\nu} \\ &= \sum_{\nu} d_{\nu\mu}^\lambda(\pi)\mathcal{T}_{\lambda\nu} \\ &= \sum_{\nu} (-)^{\lambda-\mu}\delta_{\mu,-\nu}\mathcal{T}_{\lambda\nu} \\ &= (-)^{\lambda-\mu}\mathcal{T}_{\lambda-\mu}. \end{aligned} \quad (176)$$

Applying this expression to the multipole operator $\mathcal{M}_\lambda^{(\text{intr})}(\theta)$ allows to express Eq. (175) as

$$\begin{aligned} & (-)^{I_1+K_1}(-)^{I_2+K_2}(-)^{I_1+\lambda-I_2} (I_1K_1\lambda - K_-|I_2K_2)(-)^{\lambda-K_-}\langle K_2|\mathcal{M}_{\lambda,-K_-}^{(\text{intr})}(\theta)|K_1\rangle \\ &= (-)^{I_1+K_1}(-)^{I_2+K_2}(-)^{I_1+\lambda-I_2} (-)^{\lambda-K_1+K_2}(I_1K_1\lambda - K_-|I_2K_2)\langle K_2|\mathcal{M}_{\lambda,-K_-}^{(\text{intr})}(\theta)|K_1\rangle \\ &= (-)^{I_1+K_1+I_2+K_2+I_1+\lambda-I_2+\lambda-K_1+K_2}(I_1K_1\lambda - K_-|I_2K_2)\langle K_2|\mathcal{M}_{\lambda,-K_-}^{(\text{intr})}(\theta)|K_1\rangle \\ &= (-)^{2(I_1+K_2)}(I_1K_1\lambda - K_-|I_2K_2)\langle K_2|\mathcal{M}_{\lambda,-K_-}^{(\text{intr})}(\theta)|K_1\rangle \end{aligned} \quad (177)$$

since λ is integer.

Now, K is the projection of I onto the “3” axis of the intrinsic reference frame, and therefore the phase factor $(-)^{2(I_1+K_2)}$ is always equal to unity, thus terminating the proof that the first and the last term in Eq. (173) are equal.

In the same way, the second term in Eq. (173) can be written as

$$\begin{aligned}
& (-)^{I_2+K_2} (I_1 K_1 \lambda - K_+ | I_2 - K_2) \langle \bar{K}_2 | \mathcal{M}_{\lambda, -K_+}^{(\text{intr})}(\theta) | K_1 \rangle \\
&= (-)^{I_2+K_2} (-)^{I_1+\lambda-I_2} (I_1 - K_1 \lambda K_+ | I_2 K_2) \langle K_2 | \mathcal{R}_i \mathcal{M}_{\lambda, -K_+}^{(\text{intr})}(\theta) | K_1 \rangle \\
&= (-)^{I_1+K_2+\lambda} (I_1 - K_1 \lambda K_+ | I_2 K_2) (-)^{\lambda+K_+} \langle K_2 | \mathcal{M}_{\lambda K_+}^{(\text{intr})}(\theta) \mathcal{R}_i | K_1 \rangle \\
&= (-)^{I_1+K_2+\lambda} (I_1 - K_1 \lambda K_+ | I_2 K_2) (-)^{\lambda+K_+} \langle K_2 | \mathcal{M}_{\lambda K_+}^{(\text{intr})}(\theta) \mathcal{R}_i^2 | \bar{K}_1 \rangle \quad (178) \\
&= (-)^{I_1+K_1+2K_2+2I_1} (I_1 - K_1 \lambda K_+ | I_2 K_2) \langle K_2 | \mathcal{M}_{\lambda K_+}^{(\text{intr})}(\theta) | \bar{K}_1 \rangle \\
&= (-)^{2(I_1+K_2)} (-)^{I_1+K_1} (I_1 - K_1 \lambda K_+ | I_2 K_2) \langle K_2 | \mathcal{M}_{\lambda K_+}^{(\text{intr})}(\theta) | \bar{K}_1 \rangle \\
&= (-)^{I_1+K_1} (I_1 - K_1 \lambda K_+ | I_2 K_2) \langle K_2 | \mathcal{M}_{\lambda K_+}^{(\text{intr})}(\theta) | \bar{K}_1 \rangle
\end{aligned}$$

since $\mathcal{R}_i^2 = (-)^{2I}$ [98], and since $(-)^{2(I_1+K_2)} = 1$ for the reason explained above. Thus we have demonstrated that the second and the third terms in Eq. (173) are equal.

Finally we can write Eq. (173) as

$$\begin{aligned}
\langle \widetilde{I_2 K_2} | \mathcal{M}_{\lambda}^{(\text{spec})} | \widetilde{I_1 K_1} \rangle &= \sqrt{\frac{2I_1 + 1}{(1 + \delta_{K_1 0})(1 + \delta_{K_2 0})}} \\
&\times \left[(I_1 K_1 \lambda K_2 - K_1 | I_2 K_2) \langle K_2 | \mathcal{M}_{\lambda, K_2 - K_1}^{(\text{intr})}(\theta) | K_1 \rangle \right. \\
&\left. + (-)^{I_1+K_1} (I_1 - K_1 \lambda K_2 + K_1 | I_2 K_2) \langle K_2 | \mathcal{M}_{\lambda, K_2 + K_1}^{(\text{intr})}(\theta) | \bar{K}_1 \rangle \right]. \quad (179)
\end{aligned}$$

2. Electric quadrupole moment

Let us consider as one of the most important applications the electric quadrupole moment operator (or simply quadrupole moment operator). In this case, one has $\lambda = 2$, and we will denote the corresponding tensor by Q instead of \mathcal{M} .

We will define the intrinsic quadrupole moment, generally depending on K , as [97]

$$Q_0^K \equiv \frac{1}{e} \sqrt{\frac{16\pi}{5}} \langle K | Q_{20}^{(\text{intr})} | K \rangle, \quad (180)$$

where e stands for the elementary charge, and the spectroscopic quadrupole moment as [97]

$$Q^K \equiv \frac{1}{e} \sqrt{\frac{16\pi}{5}} \langle IM = IK | Q_{20}^{(\text{spec})} | IM = IK \rangle. \quad (181)$$

Using the Wigner-Eckart theorem Eq. (171) and the result Eq. (179), one gets immediately

$$Q^K = \frac{1}{(1+\delta_{K0})} \left[(II20|II)(IK20|IK)Q_0^K + (II20|II)(I - K \ 2 \ 2K|IK)(-)^{I+K} \frac{1}{e} \sqrt{\frac{16\pi}{5}} \langle K|Q_{2,2K}^{(\text{intr})}|\bar{K}\rangle \right]. \quad (182)$$

Owing to this expression, one can discuss separately the following cases :

- If $K = 0$, it is easy to see that the first and the second term in this expression are identical. This is so, because one must have

$$(-)^I \Phi_{\bar{0}} = \Phi_0 \quad (183)$$

to ensure that for $K = 0$ the wave function Eq. (151) is not identically vanishing. As a consequence, one has

$$Q^{K=0} = (II20|II)(I020|I0)Q_0^{K=0}. \quad (184)$$

- If $K > 1$, only the first term has to be considered because the second index $2K$ of the quadrupole tensor cannot be greater than 2 in absolute value. Therefore one gets

$$Q^{K>1} = (II20|II)(I120|I1)Q_0^{K>1}. \quad (185)$$

- The previous cases can be cast into the general formula

$$Q^{K=0 \text{ or } K>1} = (II20|II)(IK20|IK)Q_0^{K=0 \text{ or } K>1}. \quad (186)$$

The product of the two Clebsh-Gordan coefficients in this formula can be simplified further with the help of the following expressions, that can be found in [96]:

$$(AaBb|CC) = \delta_{a+b,C} (-)^{A-a} \times \left[\frac{(2C+1)!(A+B-C)!(A+a)!(B+b)!}{(A+B+C+1)!(A-B+C)!(-A+B+C)!(A-a)!(B-b)!} \right]^{1/2}, \quad (187)$$

for $C = c$, and

$$(AaBb|A+B-2; a+b) = \left[\frac{2A(2A-1)2B(2B-1)}{2(2A+2B-2)(2A+2B-1)} \right]^{1/2} \times \left[\binom{2A}{A-a} \binom{2B}{B-b} \binom{2A+2B-4}{A+B-a-b-2} \right]^{-1/2} \times \left[\binom{2A-2}{A-a} \binom{2B-2}{B+b} - 2 \binom{2A-2}{A-a-1} \binom{2B-2}{B+b-1} + \binom{2A-2}{A-a-2} \binom{2B-2}{B+b-2} \right] \quad (188)$$

for $C = A + B - 2$.

One obtains then the well known result

$$Q^{K=0 \text{ or } K>1} = \frac{3K^2 - I(I+1)}{(I+1)(2I+3)} Q_0^{K=0 \text{ or } K>1}. \quad (189)$$

One can notice the remarkable result that for nuclei with spin $I = 0$ (thus having $K = 0$), the spectroscopic quadrupole moment automatically vanishes, although the intrinsic quadrupole moment could be well different from zero. This expresses the fact that the latter is actually not an observable, for example, for the ground state of even-even nuclei, for which $I = 0$ is verified.

- If $K = 1/2$ or $K = 1$ the full expression in Eq. (182) has in principle to be considered. Note however that for even-even nuclei the case $K = 1/2$ cannot occur, because K must be integer since I itself is integer.

3. Magnetic dipole moment

Let us consider as another important application the magnetic dipole moment operator (or simply dipole moment operator). In this case, one has $\lambda = 1$, and we will denote the corresponding tensor by M instead of \mathcal{M} .

Following, e.g., Rowe [97] we define the intrinsic dipole moment, in the state $|K\rangle$, as

$$\mu_0^K \equiv \sqrt{\frac{4\pi}{3}} \langle K | M_{10}^{(\text{intr})} | K \rangle \quad (190)$$

and the spectroscopic dipole moment in the state $|\widetilde{IM = IK}\rangle$ as

$$\mu^K \equiv \sqrt{\frac{4\pi}{3}} \langle \widetilde{IM = IK} | M_{10}^{(\text{spec})} | \widetilde{IM = IK} \rangle. \quad (191)$$

Using again the Wigner-Eckart theorem in Eq. (171) and the result of Eq. (179), one gets in this case

$$\begin{aligned} \mu^K &= \frac{1}{(1+\delta_{K0})} \left[(II10|II)(IK10|IK) \mu_0^K \right. \\ &\quad \left. + (II10|II)(I - K \ 1 \ 2K|IK) (-)^{I+K} \sqrt{\frac{4\pi}{3}} \langle K | M_{1,2K}^{(\text{intr})} | \bar{K} \rangle \right]. \end{aligned} \quad (192)$$

The Clebsh-Gordan coefficients appearing in the first term of this expression are given by [96]

$$(II10|II) = \left[\frac{I}{I+1} \right]^{1/2} \quad (193)$$

and

$$(IK10|IK) = K \left[\frac{1}{I(I+1)} \right]^{1/2}, \quad (194)$$

and a similar discussion as for the electric quadrupole moment finally leads to the conclusion that for $K = 0$ or $K > 1/2$, one gets

$$\mu^{K=0 \text{ or } K>1/2} = \frac{K}{I+1} \mu_0^K. \quad (195)$$

To close this appendix, let us recall that to obtain the spectroscopic magnetic dipole and electric quadrupole moments of the bandhead state of a rotational band with $K \notin \{1/2, 1\}$ one has to set $I = K$ in Eqs. (189) and (195).

B. Multipole expansion of the magnetic vector potential

1. General case

We start from the form of the vector potential in the Coulomb gauge, given by

$$\vec{A}(\vec{r}) = \frac{\mu_0}{4\pi} \int \frac{\vec{j}(\vec{R})}{|\vec{r} - \vec{R}|} d^3R. \quad (196)$$

Given a set of normalised spherical harmonics $\{C_q^{(k)}(\theta, \phi)\}_{k,q}$, one can define the following normalised vector spherical harmonics, for $k \geq 1$,

$$\vec{Y}_q^{(k)} = \vec{e}_r C_q^{(k)}(\theta, \phi), \quad (197)$$

$$\vec{\Psi}_q^{(k)} = \frac{1}{\sqrt{k(k+1)}} \left[r \vec{\nabla} C_q^{(k)}(\theta, \phi) \right], \quad (198)$$

$$\vec{\Phi}_q^{(k)} = \frac{i}{\hbar \sqrt{k(k+1)}} \left[\vec{L} C_q^{(k)}(\theta, \phi) \right]. \quad (199)$$

It should be emphasised that while the definition of $\vec{Y}_q^{(k)}$ remains unchanged for $(k=0, q=0)$, both $\vec{\Psi}_0^{(0)}$ and $\vec{\Phi}_0^{(0)}$ are identically zero. Any vector field $\vec{V}(\vec{r})$ can be decomposed into a series of vector spherical harmonics as

$$\vec{V}(\vec{r}) = \sum_{k=0}^{\infty} \sum_{q=-k}^k \left({}^{(r)}V_q^{(k)}(r) \vec{Y}_q^{(k)} + {}^{(1)}V_q^{(k)}(r) \vec{\Psi}_q^{(k)} + {}^{(2)}V_q^{(k)}(r) \vec{\Phi}_q^{(k)} \right). \quad (200)$$

However,

$$\vec{\nabla} \cdot \vec{V} = \left(\frac{d}{dr} \left[{}^{(r)}V_q^{(k)} \right] + \frac{2}{r} {}^{(r)}V_q^{(k)} - \frac{k(k+1)}{r} {}^{(1)}V_q^{(k)} \right) C_q^{(k)}(\theta, \phi), \quad (201)$$

and \vec{A} respects the Coulomb gauge condition $\vec{\nabla} \cdot \vec{A} = 0$, therefore, \vec{A} can be expressed into a series of $\vec{\Phi}_q^{(k)}$ only, taking the form

$$\vec{A}(\vec{r}) = \frac{\mu_0}{4\pi} \sum_{k=1}^{\infty} \sum_{q=-k}^k \frac{i}{\hbar \sqrt{k(k+1)}} \left[\vec{L}C_q^{(k)}(\theta, \phi) \right] A_q^{(k)}(r). \quad (202)$$

Using the orthogonality relation

$$\frac{-1}{\hbar^2 k(k+1)} \int_{\theta, \phi} \left[\vec{L}C_{q'}^{(k')}(\theta, \phi) \right] \cdot \left[\vec{L}C_{-q}^{(k)}(\theta, \phi) \right] d^2\Omega = (-1)^q \delta_{k,k'} \delta_{q,q'}, \quad (203)$$

one obtains

$$A_q^{(k)}(r) = \frac{4\pi}{\mu_0} \frac{i}{\hbar \sqrt{k(k+1)}} (-1)^q \int_{\theta, \phi} \left[\vec{L}C_{-q}^{(k)}(\theta, \phi) \right] \cdot \vec{A}(\vec{r}) d^2\Omega. \quad (204)$$

The multipolar expansion of $\frac{1}{|\vec{r}-\vec{R}|}$ in Eq. (196),

$$\begin{aligned} \vec{A}(\vec{r}) &= \frac{\mu_0}{4\pi} \sum_{k=0}^{\infty} \frac{1}{r^{k+1}} \sum_{q=-k}^k (-1)^q C_q^{(k)}(\theta, \phi) \int_{R=0}^r C_{-q}^{(k)}(\Theta, \Phi) \vec{j}(\vec{R}) R^k d^3R, \\ &+ \frac{\mu_0}{4\pi} \sum_{k=0}^{\infty} r^k \sum_{q=-k}^k (-1)^q C_q^{(k)}(\theta, \phi) \int_{R=r}^{\infty} C_{-q}^{(k)}(\Theta, \Phi) \vec{j}(\vec{R}) \frac{1}{R^{k+1}} d^3R, \end{aligned} \quad (205)$$

can be inserted in Eq. (204), and, computing the effect of each component of \vec{L} on $C_{-q}^{(k)}$, one can prove that

$$\left(\int_{\theta, \phi} (-1)^{q'} C_{q'}^{(k')}(\theta, \phi) \cdot \left[\vec{L}C_{-q}^{(k)}(\theta, \phi) \right] d^2\Omega \right) C_{-q'}^{(k')}(\Theta, \Phi) = \vec{L}C_{-q}^{(k)}(\Theta, \Phi), \quad (206)$$

therefore,

$$\begin{aligned} A_q^{(k)}(r) &= \frac{i}{\hbar \sqrt{k(k+1)}} \frac{1}{r^{k+1}} (-1)^q \int_{R=0}^r \left[\vec{L}C_{-q}^{(k)}(\Theta, \Phi) \right] \cdot \vec{j}(\vec{R}) R^k d^3R, \\ &+ \frac{i}{\hbar \sqrt{k(k+1)}} r^k (-1)^q \int_{R=r}^{\infty} \left[\vec{L}C_{-q}^{(k)}(\Theta, \Phi) \right] \cdot \vec{j}(\vec{R}) \frac{1}{R^{k+1}} d^3R. \end{aligned} \quad (207)$$

To follow convention, we can write the multipolar expansion of the vector potential as

$$\begin{aligned} \vec{A}(\vec{r}) &= \frac{\mu_0}{4\pi} \sum_{k=1}^{\infty} \sum_{q=-k}^k (-1)^q \frac{(-i)}{\hbar k} \left[\vec{L}C_q^{(k)}(\theta, \phi) \right] \text{in} M_{-q}^{(k)}(r) \frac{1}{r^{k+1}} \\ &+ \frac{\mu_0}{4\pi} \sum_{k=1}^{\infty} \sum_{q=-k}^k (-1)^q \frac{(-i)}{\hbar k} \left[\vec{L}C_q^{(k)}(\theta, \phi) \right] \text{ex} M_{-q}^{(k)}(r) r^k, \end{aligned} \quad (208)$$

with

$$\text{in} M_q^{(k)}(r) \equiv -\frac{i}{\hbar(k+1)} \int_{R=0}^r \left[\vec{L}C_q^{(k)}(\Theta, \Phi) \right] \cdot \vec{j}(\vec{R}) R^k d^3R, \quad (209)$$

and

$$\text{ex} M_q^{(k)}(r) \equiv -\frac{i}{\hbar(k+1)} \int_{R=r}^{\infty} \left[\vec{L}C_q^{(k)}(\Theta, \Phi) \right] \cdot \vec{j}(\vec{R}) \frac{1}{R^{k+1}} d^3R. \quad (210)$$

2. Magnetic dipole moment

Truncating the previous expansion to the first non-vanishing term ($k = 1$) yields

$$\begin{aligned}\vec{A}(\vec{r}) &= \frac{\mu_0}{4\pi} \sum_{q=-1}^1 (-1)^q \frac{(-i)}{\hbar} \left[\vec{L}C_q^{(1)}(\theta, \phi) \right] \frac{\text{in}M_{-q}^{(1)}(r)}{r^2} \\ &+ \frac{\mu_0}{4\pi} \sum_{q=-1}^1 (-1)^q \frac{(-i)}{\hbar} \left[\vec{L}C_q^{(1)}(\theta, \phi) \right] \text{ex}M_{-q}^{(1)}(r)r.\end{aligned}\quad (211)$$

For an arbitrary vector $\vec{v}^{(1)}$, one can show that

$$[\vec{r} \wedge \vec{v}^{(1)}]_\lambda = \frac{-i}{\hbar} \left[r \vec{L}C_\lambda^{(1)}(\theta, \phi) \right] \cdot \vec{v}^{(1)}.\quad (212)$$

We recall that for vectors \vec{v} , represented as first-rank tensors $\vec{v}^{(1)}$, the scalar product is defined as

$$\vec{v}^{(1)} \cdot \vec{u}^{(1)} = \sum_{\lambda} (-1)^\lambda v_\lambda^{(1)} u_{-\lambda}^{(1)}.\quad (213)$$

Moreover, it is important to remember \vec{L} commutes with any function of r , from there, one can look at the following scalar product:

$$\begin{aligned}\vec{A}(\vec{r}) \cdot \vec{v}^{(1)} &= \frac{\mu_0}{4\pi r^3} \sum_{q=-1}^1 (-1)^q \frac{(-i)}{\hbar} \left[r \vec{L}C_q^{(1)}(\theta, \phi) \right] \frac{\text{in}M_q^{(1)}(r)}{r^3} \cdot \vec{v}^{(1)} \\ &+ \frac{\mu_0}{4\pi} \sum_{q=-1}^1 (-1)^q \frac{(-i)}{\hbar} \left[r \vec{L}C_q^{(1)}(\theta, \phi) \right] \text{ex}M_{-q}^{(1)}(r) \cdot \vec{v}^{(1)} \\ &= \frac{\mu_0}{4\pi r^3} \sum_{q=-1}^1 (-1)^q [\vec{r} \wedge \vec{v}^{(1)}]_q \text{in}M_{-q}^{(1)}(r) + \frac{\mu_0}{4\pi} \sum_{q=-1}^1 (-1)^q [\vec{r} \wedge \vec{v}^{(1)}]_q \text{ex}M_{-q}^{(1)}(r) \\ &= \frac{\mu_0}{4\pi r^3} \text{in}\vec{M}^{(1)}(r) \cdot (\vec{r} \wedge \vec{v}^{(1)}) + \frac{\mu_0}{4\pi} \text{ex}\vec{M}^{(1)}(r) \cdot (\vec{r} \wedge \vec{v}^{(1)}) \\ &= \left(\frac{\mu_0}{4\pi r^3} (\text{in}\vec{M}^{(1)}(r) \wedge \vec{r}) + \frac{\mu_0}{4\pi} (\text{ex}\vec{M}^{(1)}(r) \wedge \vec{r}) \right) \cdot \vec{v}^{(1)}.\end{aligned}\quad (214)$$

Therefore, one obtains

$$\vec{A}(\vec{r}) = \frac{\mu_0}{4\pi} \frac{\text{in}\vec{M}^{(1)}(r) \wedge \vec{r}}{r^3} + \frac{\mu_0}{4\pi} \left(\text{ex}\vec{M}^{(1)}(r) \wedge \vec{r} \right),\quad (215)$$

with, also using Eq. (212),

$$\text{in}\vec{M}^{(1)}(r) = \frac{1}{2} \int_{R=0}^r \vec{R} \wedge \vec{j}(\vec{R}) d^3R\quad (216)$$

and

$$\text{ex}\vec{M}^{(1)}(r) = \frac{1}{2} \int_{R=r}^{\infty} \frac{\vec{R} \wedge \vec{j}(\vec{R})}{R^3} d^3R.\quad (217)$$

C. Hyperfine interactions

1. Dipole

One can rewrite Eqs. (211) and (215) as

$$\vec{A}(\vec{r}) \equiv \frac{\mu_0}{4\pi} \sum_{q=-1}^1 (-1)^q \frac{(-i)}{\hbar} \left[\vec{L}C_q^{(1)}(\theta, \phi) \right] f_{M, -q}(r), \quad (218)$$

$$\vec{f}_M(r) = \frac{1}{2} \left(\frac{1}{r^2} \int_{R=0}^r \vec{R} \wedge \vec{j}(\vec{R}) d^3R + r \int_{R=r}^{\infty} \frac{\vec{R} \wedge \vec{j}(\vec{R})}{R^3} d^3R \right), \quad (219)$$

and insert it in ${}^{\text{at}}H_{\text{hf,dip}} = -ec\vec{\alpha} \cdot \vec{A}(\vec{r})$,

$$\begin{aligned} \langle n_a \kappa_a F M_F | {}^{\text{at}}H_{\text{hf,dip}} | n_b \kappa_b F M_F \rangle = \\ -iec \frac{\mu_0}{4\pi\hbar} \sum_{q=-1}^1 (-1)^q \langle n_a \kappa_a m_a F M_F | \left[\vec{\alpha} \cdot \vec{L}C_q^{(1)}(\theta, \phi) \right] f_{M, -q}(r) | n_b \kappa_b m_b F M_F \rangle \end{aligned} \quad (220)$$

The Wigner-Eckart theorem states that

$$\langle F M_F | T_q^{(k)} | F' M_{F'} \rangle = (-1)^{F-M_F} \begin{pmatrix} F & k & F' \\ -M_F & q & M_{F'} \end{pmatrix} \langle F || T^{(k)} || F' \rangle, \quad (221)$$

where $T_q^{(k)}$ is a tensor operator of rank k and q is the projection of the operator in the z -axis.

$\langle F || T^{(k)} || F' \rangle$ is the reduced matrix element of the operator, independent of M_F and $M_{F'}$.

Using Eq. (221), one can obtain that

$$\begin{aligned} \langle I M_I | f_{M, -q}(r) | I M_I' \rangle &= (-1)^{I-M_I} \begin{pmatrix} I & 1 & I \\ -M_I & -q & M_I' \end{pmatrix} \langle I || f_M(r) || I \rangle \\ &= (-1)^{I-M_I} \begin{pmatrix} I & 1 & I \\ -M_I & -q & M_I' \end{pmatrix} \begin{pmatrix} I & 1 & I \\ -I & -q & I \end{pmatrix}^{-1} \langle II | f_{M, -q}(r) | II \rangle. \end{aligned} \quad (222)$$

Given two irreducible tensor operators $T^{(k)}$ and $U^{(k)}$ of rank k , acting, respectively on the electronic and nuclear spaces, one can compute the matrix element of their scalar product as

$$\begin{aligned} \langle (J_a I) F M_F | T^{(k)} \cdot U^{(k)} | (J_b I) F' M_{F'} \rangle \\ = (-1)^{J_b + I + F} \delta_{F, F'} \delta_{M_F, M_{F'}} \begin{Bmatrix} J_b & I & F \\ I & J_a & k \end{Bmatrix} \langle J_a || T^{(k)} || J_b \rangle \langle I || U^{(k)} || I \rangle. \end{aligned} \quad (223)$$

Therefore, since only $f_{M,0}(r)$ is non-zero, one can write

$$\begin{aligned}
& \langle n_a \kappa_a F M_F | [\vec{\alpha} \cdot \vec{L} C_q^{(1)}(\theta, \phi)] f_{M,0}(r) | n_b \kappa_b F M_F \rangle \\
&= (-1)^{J_b + I + F} \delta_{F, F'} \delta_{M_F, M_{F'}} \delta_{q, 0} \begin{Bmatrix} J_b & I & F \\ I & J_a & 1 \end{Bmatrix} \\
&\times \langle n_a \kappa_a | [\vec{\alpha} \cdot \vec{L} C_q^{(1)}(\theta, \phi)] \langle II | f_{M,0}(r) | II \rangle | | n_b \kappa_b \rangle \begin{pmatrix} I & 1 & I \\ -I & 0 & I \end{pmatrix}^{-1}.
\end{aligned} \tag{224}$$

One notices that

$$\begin{aligned}
& \langle (J_a I) F M_F | \vec{I} \cdot \vec{J} | (J_b I) F' M_{F'} \rangle = \\
& (-1)^{J_b + I + F} \delta_{F, F'} \delta_{M_F, M_{F'}} \begin{Bmatrix} J_b & I & F \\ I & J_a & 1 \end{Bmatrix} \langle J_a || \vec{J} || J_b \rangle \langle I || \vec{I} || I \rangle.
\end{aligned} \tag{225}$$

Since,

$$\langle j || \vec{J} || j' \rangle = \sqrt{j(2j+1)(j+1)} \delta_{jj'}, \tag{226}$$

one sees Eq. (225) vanishes for states with different F , I or κ (equiv. J). Furthermore, comparing Eqs. (224) and (225), one can see that for diagonal matrix elements, the magnetic dipole hyperfine interaction is proportional to $\vec{I} \cdot \vec{J}$,

$$\langle n_a \kappa_a F M_F |^{\text{at}} H_{\text{hf, dip}} | n_a \kappa_a F M_F \rangle = a \langle n_a \kappa_a F M_F | \vec{I} \cdot \vec{J} | n_a \kappa_a F M_F \rangle, \tag{227}$$

and

$$a \equiv -ie c \frac{\mu_0}{4\pi \hbar} \frac{\langle n_a \kappa_a | [\vec{\alpha} \cdot \vec{L} C_0^{(1)}(\theta, \phi)] \langle II | f_{M,0}(r) | II \rangle | | n_a \kappa_a \rangle}{\begin{pmatrix} I & 1 & I \\ -I & 0 & I \end{pmatrix} \langle J_a || \vec{J} || J_a \rangle \langle I || \vec{I} || I \rangle}. \tag{228}$$

This expression can be readily computed in the case of a single electron. One can calculate the matrix element $\langle n_a \kappa_a m_a | [\vec{\alpha} \cdot \vec{L} C_0^{(1)}(\theta, \phi)] {}^I f_M(r) | n_b \kappa_b m_b \rangle$, where ${}^I f_M(r) \equiv \langle II | f_{M,0}(r) | II \rangle$, by noticing that \vec{L} commutes with any function of r , and by extension so does $\vec{\alpha} \cdot \vec{L}$

$$[\vec{\alpha} \cdot \vec{L} C_0^{(1)}(\theta, \phi)] {}^I f_M(r) = {}^I f_M(r) [\vec{\alpha} \cdot \vec{L} C_0^{(1)}(\theta, \phi)] = \vec{\alpha} \cdot \vec{L} [C_0^{(1)I} f_M(r)], \tag{229}$$

and

$$\vec{\alpha} \cdot \vec{L} [C_0^{(1)}(\theta, \phi) | n \kappa m \rangle] = [\vec{\alpha} \cdot \vec{L} C_0^{(1)}(\theta, \phi)] | n \kappa m \rangle + C_0^{(1)}(\theta, \phi) [\vec{\alpha} \cdot \vec{L} | n \kappa m \rangle], \tag{230}$$

since \vec{L} is a differential operator this is simply the Leibniz product rule.

Thus,

$$\begin{aligned} \langle n_a \kappa_a m_a | \vec{\alpha} \cdot \vec{L} [C_0^{(1)}(\theta, \phi)^I f_M(r)] | n_b \kappa_b m_b \rangle = \\ \left[\langle n_a \kappa_a m_a | \vec{\alpha} \cdot \vec{L} [C_0^{(1)}(\theta, \phi)^I f_M(r) | n_b \kappa_b m_b \rangle \right] - \left[\langle n_a \kappa_a m_a | f_M(r) C_0^{(1)}(\theta, \phi) \right] \left[\vec{\alpha} \cdot \vec{L} | n_b \kappa_b m_b \rangle \right] \end{aligned} \quad (231)$$

Moreover,

$$\vec{\alpha} \cdot \vec{L} | n \kappa m \rangle = \begin{pmatrix} 0 & \vec{\sigma} \cdot \vec{L} \\ \vec{\sigma} \cdot \vec{L} & 0 \end{pmatrix} \frac{1}{r} \begin{pmatrix} P_{n\kappa}(r) \chi_{\kappa m}(\theta, \phi) \\ i Q_{n\kappa}(r) \chi_{-\kappa m}(\theta, \phi) \end{pmatrix} = \frac{1}{r} \begin{pmatrix} \hbar(\kappa - 1) i Q_{n\kappa}(r) \chi_{-\kappa m}(\theta, \phi) \\ \hbar(-\kappa - 1) P_{n\kappa}(r) \chi_{\kappa m}(\theta, \phi) \end{pmatrix}, \quad (232)$$

since $(\vec{\sigma} \cdot \vec{L} + \hbar) \chi_{\kappa m}(\theta, \phi) = -\hbar \kappa \chi_{\kappa m}(\theta, \phi)$.

Hence, one can write

$$\begin{aligned} \langle n_a \kappa_a | [\vec{\alpha} \cdot \vec{L} C_0^{(1)}(\theta, \phi)]^I f_M(r) | n_b \kappa_b \rangle = \\ -i\hbar(\kappa_a + \kappa_b) \langle \kappa_a m_a | C_0^{(1)}(\theta, \phi) | -\kappa_b m_b \rangle \int_{r=0}^{\infty} I f_M(r) (P_{n_a \kappa_a}(r) Q_{n_b \kappa_b}(r) + Q_{n_a \kappa_a}(r) P_{n_b \kappa_b}(r)) dr. \end{aligned} \quad (233)$$

Or, alternatively,

$$\begin{aligned} \langle n_a \kappa_a m_a | [\vec{\alpha} \cdot \vec{L} C_0^{(1)}(\theta, \phi)]^I f_M(r) | n_b \kappa_b m_b \rangle = \\ -i\hbar(\kappa_a + \kappa_b) \langle \kappa_a | C^{(1)}(\theta, \phi) | -\kappa_b \rangle \int_{r=0}^{\infty} I f_M(r) (P_{n_a \kappa_a}(r) Q_{n_b \kappa_b}(r) + Q_{n_a \kappa_a}(r) P_{n_b \kappa_b}(r)) dr. \end{aligned} \quad (234)$$

One can now calculate the hyperfine splitting due to the magnetic dipole interaction, using Eq. (224),

$$\langle \kappa_a || C^{(k)} || \kappa_b \rangle = (-1)^{J_a} i \sqrt{[J_a][J_b]} \begin{pmatrix} J_a & J_b & k \\ -1/2 & 1/2 & 0 \end{pmatrix} \Pi(L_a + k + L_b) \quad (235)$$

with

$$[x] \equiv 2x + 1, \quad \Pi(l) \equiv \begin{cases} 1, & \text{if } l \text{ is even} \\ 0, & \text{if } l \text{ is odd} \end{cases}. \quad (236)$$

This means that

$$\langle \kappa_a || C^{(1)}(\theta, \phi) || -\kappa_a \rangle = -\frac{1}{2} \sqrt{\frac{[J_a]}{J_a(J_a + 1)}}. \quad (237)$$

Finally,

$$\begin{pmatrix} I & 1 & I \\ -I & 0 & I \end{pmatrix} = \sqrt{\frac{I}{(I+1)[I]}}, \quad (238)$$

thus, recalling Eqs. (226) to (228),

$$\begin{aligned} a &= ec \frac{\mu_0}{2\pi} \frac{\kappa_a}{IJ_a(J_a+1)} \int_{r=0}^{\infty} \langle II | f_{M,0} | II \rangle P_{n_a \kappa_a}(r) Q_{n_a \kappa_a}(r) dr. \\ &= ec \frac{\mu_0}{2\pi} \frac{\kappa_a}{IJ_a(J_a+1)} \mathcal{I}_{\text{intr/spec}}^{M_1} \int_{r=0}^{\infty} \frac{1}{2} \left(\frac{1}{r^2} \int_{R=0}^r \vec{R} \wedge \vec{j}(\vec{R}) d^3 R \right. \\ &\quad \left. + r \int_{R=r}^{\infty} \frac{\vec{R} \wedge \vec{j}(\vec{R})}{R^3} d^3 R \right) P_{n_a \kappa_a}(r) Q_{n_a \kappa_a}(r) dr, \end{aligned} \quad (239)$$

where $\mathcal{I}_{\text{spec/intr}}^{M_1}$ is the conversion factor from the intrinsic magnetic dipole to the laboratory one.

Ultimately, using Eqs. (225) to (227), and

$$\begin{aligned} \begin{Bmatrix} J & I & F \\ I & J & 1 \end{Bmatrix} &= (-1)^{F+I+J+1} \frac{2(I(I+1) + J(J+1) - F(F+1))}{\sqrt{2I(2I+1)(2I+2)2J(2J+1)(2J+2)}} \\ &= (-1)^{F+I+J} \frac{F(F+1) - I(I+1) - J(J+1)}{2\langle J || \vec{J} || J \rangle \langle I || \vec{I} || I \rangle}, \end{aligned} \quad (240)$$

one obtains that

$$\langle n_a \kappa_a F M_F |^{\text{at}} H_{\text{hf,dip}} | n_a \kappa_a F M_F \rangle = \frac{a}{2} \tilde{K}_a \quad (241)$$

where $\tilde{K}_a \equiv F(F+1) - I(I+1) - J_a(J_a+1)$.

While Eq. (241) is a general expression for the magnetic dipole hyperfine interaction, it is particularly useful for the case of a single electron, where a can be computed explicitly with relative ease. In the case of multiple electrons, the expression of a is more complex, but the general form remains the same, and referring to Eqs. (221), (226), (228) and (238), one has

$$\begin{aligned} a &= -iec \frac{\mu_0}{4\pi\hbar} \frac{\langle n_a \kappa_a || \vec{\alpha} \cdot \vec{L} C_0^{(1)}(\theta, \phi) \langle II | f_{M,0}(r) | II \rangle || n_a \kappa_a \rangle}{I \sqrt{J_a(2J_a+1)(J_a+1)}} \\ &= -iec \frac{\mu_0}{4\pi\hbar} \frac{\langle n_a \kappa_a(J_a) m_J = J_a | \vec{\alpha} \cdot \vec{L} C_0^{(1)}(\theta, \phi) \langle II | f_{M,0}(r) | II \rangle | n_a \kappa_a(J_a) m_J = J_a \rangle}{IJ_a} \\ &\equiv -iec \frac{\mu_0}{4\pi\hbar} \frac{\langle n_a J_a J_a II | T_{M,0}^{(1)}(\vec{r}) | n_a J_a J_a II \rangle}{IJ_a}. \end{aligned} \quad (242)$$

It can be seen that, in the case one does not consider the electronic penetration inside the nucleus (i.e. $r \gg R$), $f_M(r)$ reduces to only one coordinate

$$f_M(r) = \frac{1}{2r^2} \int_{R=0}^{+\infty} \left[\vec{R} \wedge \vec{j}(\vec{R}) \right]_z d^3 R = \frac{M_z^{(1)}}{r^2}, \quad (243)$$

with $M_z^{(1)}$ the intrinsic nuclear magnetic moment, consequently,

$$\begin{aligned} a &= -iec \frac{\mu_0}{4\pi\hbar} \frac{\langle II | M_z^{(1)} | II \rangle \langle n_a \kappa_a (J_a) m_J = J_a | \vec{\alpha} \cdot \vec{L} C_0^{(1)}(\theta, \phi) r^{-2} | n_a \kappa_a (J_a) m_J = J_a \rangle}{IJ_a} \\ &= -iec \frac{\mu_0}{4\pi\hbar} M_z^{(1),(\text{spec})} \frac{\langle n_a J_a J_a | \vec{\alpha} \cdot \vec{L} C_0^{(1)}(\theta, \phi) r^{-2} | n_a J_a J_a \rangle}{J_a}, \end{aligned} \quad (244)$$

with $M_z^{(1),(\text{spec})} \equiv \mathcal{I}_{\text{intr/spec}}^{M_1} M_z^{(1)}$ the spectroscopic nuclear magnetic moment.

Or, in the case of the single electron again, one can write,

$$a = |e|c \frac{\mu_0}{2\pi} M_z^{(1),(\text{spec})} \frac{\kappa_a}{IJ_a(J_a + 1)} \int_{r=0}^{\infty} \frac{1}{r^2} P_{n_a \kappa_a}(r) Q_{n_a \kappa_a}(r) dr. \quad (245)$$

2. Quadrupole

Starting from the multipole expansion of the quadrupolar nuclear potential

$${}^{\text{at}} H_{\text{hf,quad}} = e\phi_2(\vec{r}), \quad (246)$$

with

$$\phi_2(\vec{r}) = \frac{1}{4\pi\epsilon_0} f_{\mathcal{Q},0}(r) \quad (247)$$

and

$$f_{\mathcal{Q},0}(r) = \frac{1}{2r^3} \int_{R=0}^r \rho(\vec{R}) R^2 (3 \cos^2(\Theta) - 1) d^3R + r^2 \int_{R=r}^{\infty} \frac{\rho(\vec{R}) (3 \cos^2(\Theta) - 1)}{2R^3} d^3R, \quad (248)$$

similarly to Eq. (224), one can write

$$\begin{aligned} &\langle n_a \kappa_a F M_F | {}^{\text{at}} H_{\text{hf,quad}} | n_b \kappa_b F M_F \rangle = \\ &(-1)^{J_b + I + F} \delta_{F, F'} \delta_{M_F, M_{F'}} \left\{ \begin{matrix} J_b & I & F \\ I & J_a & 2 \end{matrix} \right\} \langle n_a \kappa_a || C_0^{(2)}(\theta, \phi) \langle II | f_{\mathcal{Q},0}(r) | II \rangle || n_b \kappa_b \rangle \begin{pmatrix} I & 2 & I \\ -I & 0 & I \end{pmatrix}^{-1}, \end{aligned} \quad (249)$$

with, in the case of a single electron,

$$\begin{aligned} &\langle n_a \kappa_a || C_0^{(2)}(\theta, \phi) \langle II | f_{\mathcal{Q}}(r) | II \rangle || n_b \kappa_b \rangle = \\ &\langle \kappa_a || C^{(2)}(\theta, \phi) || \kappa_b \rangle \int_{r=0}^{\infty} \langle II | f_{\mathcal{Q},0}(r) | II \rangle (P_{n_a \kappa_a}(r) P_{n_b \kappa_b}(r) + Q_{n_a \kappa_a}(r) Q_{n_b \kappa_b}(r)) dr. \end{aligned} \quad (250)$$

The use of the following relations

$$\begin{pmatrix} I & J & F \\ J & I & 2 \end{pmatrix} = (-1)^{I+J+F} \begin{pmatrix} J & 2 & J \\ -J & 0 & J \end{pmatrix} \begin{pmatrix} I & 2 & I \\ -I & 0 & I \end{pmatrix} \frac{6\tilde{K}(\tilde{K}+1) - 8J(J+1)I(I+1)}{2I(2I-1)2J(2J-1)}, \quad (251)$$

$$\begin{pmatrix} I & 2 & I \\ -I & 0 & I \end{pmatrix} = \sqrt{\frac{2I(2I-1)}{[I](2I+2)(2I+3)}}, \quad (252)$$

$$\langle \kappa_a \| C^{(2)}(\theta, \phi) \| \kappa_a \rangle \stackrel{\text{Eq. (235)}}{=} -\frac{1}{4} \sqrt{\frac{(2J-1)[J](2J+3)}{J(J+1)}}, \quad (253)$$

allows one to write

$$\langle n_a \kappa_a F M_F |^{\text{at}} H_{\text{hf,quad}} | n_a \kappa_a F M_F \rangle = \frac{b}{2} \frac{3\tilde{K}_a(\tilde{K}_a+1) - 4J_a(J_a+1)I(I+1)}{2I(2I-1)2J_a(2J_a-1)}, \quad (254)$$

with

$$\begin{aligned} b &= -\frac{e}{4\pi\epsilon_0} \left(\frac{2J_a-1}{J_a+1} \right) \int_{r=0}^{\infty} \langle II | f_{\mathcal{Q}}(r) | II \rangle (P_{n_a \kappa_a}^2(r) + Q_{n_a \kappa_a}^2(r)) dr \\ &= -\frac{e}{4\pi\epsilon_0} \left(\frac{2J_a-1}{J_a+1} \right) \mathcal{I}_{\text{intr/spec}}^{E_2} \\ &\quad \times \int_{r=0}^{\infty} \left(\frac{1}{r^3} \int_{R=0}^r \rho(\vec{R}) R^2 (3 \cos^2(\Theta) - 1) d^3 R \right. \\ &\quad \left. + r^2 \int_{R=r}^{\infty} \frac{\rho(\vec{R}) (3 \cos^2(\Theta) - 1) d^3 R}{R^3} \right) (P_{n_a \kappa_a}^2(r) + Q_{n_a \kappa_a}^2(r)) dr, \end{aligned} \quad (255)$$

where $\mathcal{I}_{\text{intr/spec}}^{E_2}$ is the conversion factor from the intrinsic quadrupole moment to the laboratory one.

Just as for the magnetic dipole hyperfine interaction, in the case of multiple electrons, the expression of b is more complex to compute,

$$\begin{aligned} b &= -\frac{e}{4\pi\epsilon_0} \sqrt{\frac{2J(2J-1)}{[J](2J+2)(2J+3)}} \langle \kappa_a \| C^{(2)}(\theta, \phi) \| \kappa_b \rangle \\ &\quad \times \int_{r=0}^{\infty} \langle II | 4f_{\mathcal{Q}}(r) | II \rangle (P_{n_a \kappa_a}^2(r) + Q_{n_a \kappa_a}^2(r)) dr. \end{aligned} \quad (256)$$

Finally, in the case where one does not consider the electronic penetration inside the nucleus (i.e. $r \gg R$), $f_{\mathcal{Q}}(r)$ reduces to

$$4f_{\mathcal{Q}}(r) = \frac{2}{r^3} \int_{R=0}^{+\infty} \rho(\vec{R}) R^2 (3 \cos^2(\Theta) - 1) d^3 R = \frac{2\mathcal{Q}_0^{(2),(\text{spec})}}{r^3}, \quad (257)$$

where Q is the intrinsic nuclear quadrupole moment, and consequently

$$\begin{aligned}
b &= \frac{e}{4\pi\epsilon_0} \sqrt{\frac{2J(2J-1)}{[J](2J+2)(2J+3)}} \langle \kappa_a || C^{(2)}(\theta, \phi) || \kappa_b \rangle \langle II | 2Q | II \rangle \int_{r=0}^{\infty} \frac{1}{r^3} (P_{n_a \kappa_a}^2(r) + Q_{n_a \kappa_a}^2(r)) dr \\
&= \frac{2e}{4\pi\epsilon_0} Q_0^{(2),(\text{spec})} \sqrt{\frac{2J(2J-1)}{[J](2J+2)(2J+3)}} \langle \kappa_a || C^{(2)}(\theta, \phi) || \kappa_b \rangle \int_{r=0}^{\infty} \frac{1}{r^3} (P_{n_a \kappa_a}^2(r) + Q_{n_a \kappa_a}^2(r)) dr,
\end{aligned} \tag{258}$$

with $Q_0^{(2),(\text{spec})} \equiv \langle II | Q | II \rangle = \mathcal{I}_{\text{intr/spec}}^{E_2} Q_0^{(2),(\text{intr})}$ the spectroscopic nuclear quadrupole moment.

Or, in the case of the single electron again, one can write,

$$b = -\frac{e}{4\pi\epsilon_0} Q_0^{(2),(\text{spec})} \left(\frac{2J_a - 1}{J_a + 1} \right) \int_{r=0}^{\infty} \frac{1}{r^3} (P_{n_a \kappa_a}^2(r) + Q_{n_a \kappa_a}^2(r)) dr. \tag{259}$$

D. Note on the definition of the nuclear radius

As a last remark, we would like to point out the impact the choice of R_{rms} (and consequently $R_N = \sqrt{\frac{5}{3}R_{\text{rms}}^2}$) has on the computed results. For example, instead of using the empirical $R_{\text{rms}} = (0.836A^{1/3} + 0.57)$ fm [73], the root-mean-square radius ($R_{\text{rms}} = \sqrt{\langle R^2 \rangle}$) of both the uniform spherical distribution and the Fermi distribution Eq. (94) can be redefined to match the R_{rms} of the HFBCS model.

In Fig. 31a the empirical nuclear radius was used, while in Fig. 31b the HFBCS-derived radius was used. Therefore, the x -abscissae of these two figures are not to scale, but instead show the effect of the calculated nuclear radius on the relative differences between the different nuclear models. The monopole charge densities are shown in the lower panels, with the monopole potentials in the upper panels. The HFBCS model results are compared with the uniform sphere, Fermi-function, and point-charge Coulomb potentials. We can observe that after normalising by the HFBCS-derived radius, the monopole potential, and the charge density at the nuclear surface are in better agreement with the Fermi-function model.

The recalculated binding energies for both electronic and muonic ions are summarised in Tab. VIII and can be compared with the results in Tab. VI and Tab. VII showing the binding energies where the empirical R_{rms} has been chosen.

By performing this renormalisation, one observes that the energy shifts between the Fermi distribution and the HFBCS model for the electronic ion are of the order of $10^{-6}\%$, corresponding to a difference of hundreds of μeV . This indicates that, for electronic hydrogen-like ions, the R_{rms} is the

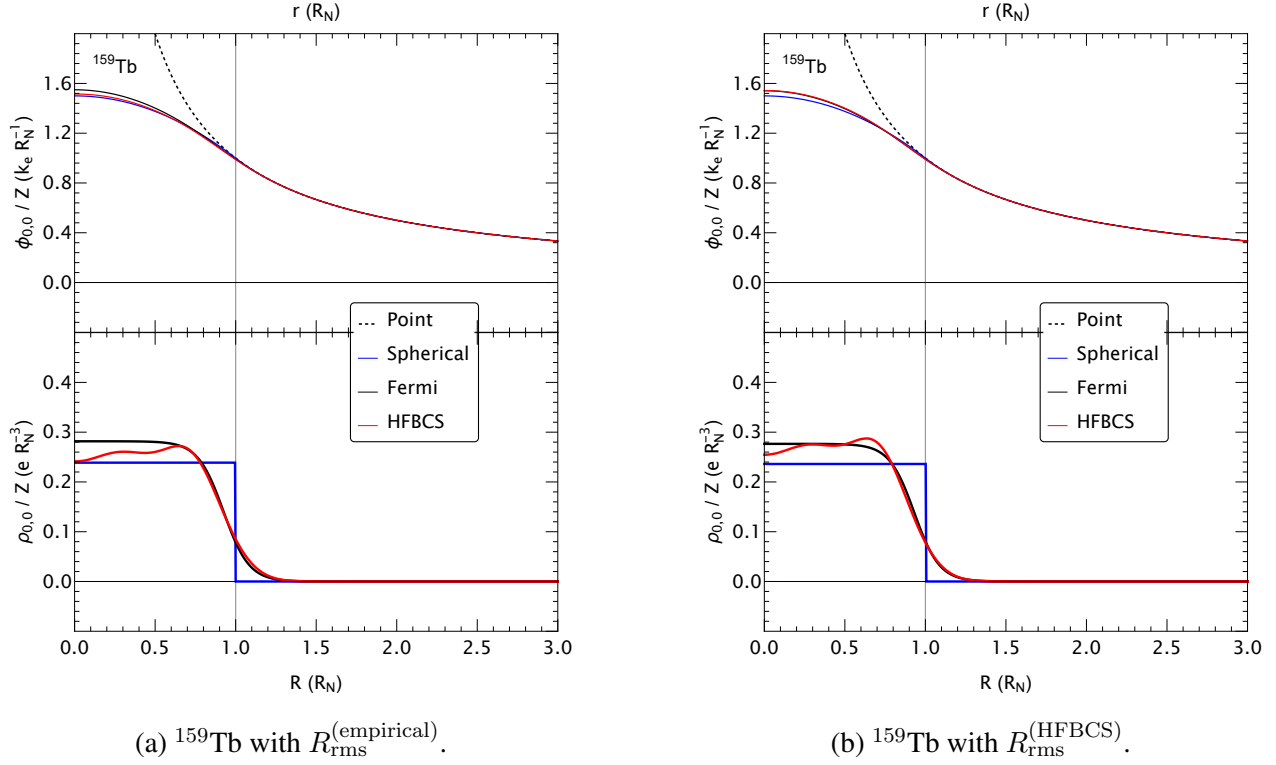


FIG. 31: (color online) Z -normalised (radial, spherically averaged) proton monopole charge densities (lower panels) and the corresponding monopole electron potentials (upper panels) for ^{159}Tb . The radial coordinate is shown as r/R_N for the potentials seen by atomic electrons (upper panels) and as R/R_N for the nuclear charge densities (lower panels), normalised with respect to the model-specific nuclear radius: in (a) R_N is the empirical radius and in (b) the HFBCS-derived radius for ^{159}Tb . The densities are in units of e/R_N^3 ; potentials are in units of k_e/R_N , with $k_e \equiv \frac{e}{4\pi\epsilon_0}$. HFBCS-type (red) calculations are compared with a uniform sphere (blue), a Fermi distribution (black), and a point-charge Coulomb potential (dotted).

dominant factor in determining energy levels, as previously noted in [73]. Consequently, one can use the HFBCS model to determine the R_{rms} of the nucleus and calculate the energy levels using the Fermi distribution, renormalised with the same R_{rms} . This approach yields accurate results while reducing computational costs.

The energy shifts between the Fermi distribution and the HFBCS model for the muonic ion are of the order of $10^{-3}\%$, corresponding to a difference of hundreds of eV, which is still significant. This means that the R_{rms} is not the only factor necessary in determining the energy levels of the muonic ion, and their binding energies still represent a valuable tool for discriminating between

different nuclear models.

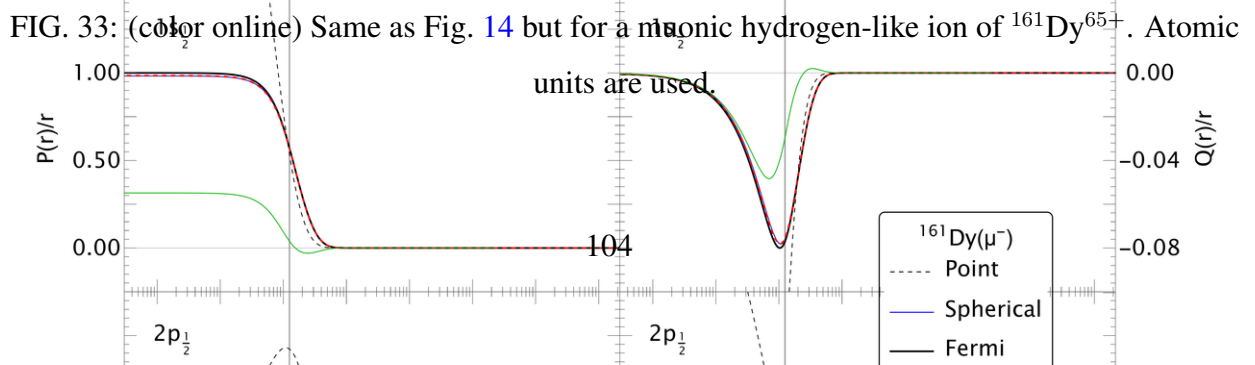
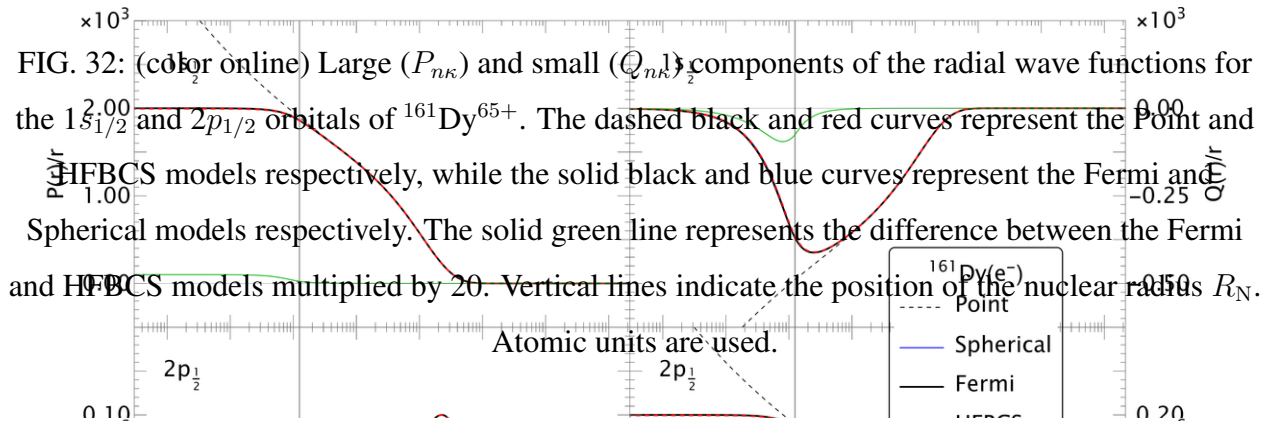
$n\ell_j$	E^{pt}	E^{sp}	E^{fm}	E^{hf}
$1s_{1/2}$	-2321.4948	-2321.0385	-2321.0392	-2321.0245
$2s_{1/2}$	-589.6305	-589.5601	-589.5603	-589.5580
$2p_{1/2}$	-589.6305	-589.6269	-589.6269	-589.6268
$2p_{3/2}$	-552.6315	-552.6315	-552.6315	-552.6315
$3s_{1/2}$	-257.8394	-257.8184	-257.8184	-257.8177
$3p_{1/2}$	-257.8394	-257.8382	-257.8382	-257.8381
$3p_{3/2}$	-246.8293	-246.8293	-246.8293	-246.8293
$3d_{3/2}$	-246.8293	-246.8293	-246.8293	-246.8293
$3d_{5/2}$	-243.5797	-243.5797	-243.5797	-243.5797
$4s_{1/2}$	-143.2890	-143.2802	-143.2802	-143.2799
$4p_{1/2}$	-143.2890	-143.2884	-143.2884	-143.2884
$4p_{3/2}$	-138.6699	-138.6699	-138.6699	-138.6699
$4d_{3/2}$	-138.6699	-138.6699	-138.6699	-138.6699
$4d_{5/2}$	-137.2922	-137.2922	-137.2922	-137.2922
$4f_{5/2}$	-137.2922	-137.2922	-137.2922	-137.2922
$4f_{7/2}$	-136.6220	-136.6220	-136.6220	-136.6220

TABLE VI: Binding energies in Hartrees for $n\ell_j$ states of the $^{163}\text{Dy}^{65+}$ ion. E^{m} denotes the relativistic energy values (excluding the rest mass) calculated by solving the Dirac equation for a (m=pt) point nucleus, (m=sp) sphere model, (m=fm) Fermi model, and (m=hf) spherically averaged HFBCS model.

E. Results for ^{161}Dy

$n\ell_j$	E^{pt}	E^{sp}	E^{fm}	E^{hf}
$1s_{1/2}$	-479680.4	-285823.2	-286916.6	-284560.7
$2s_{1/2}$	-121832.8	-90810.8	-91087.4	-90671.6
$2p_{1/2}$	-121832.8	-115503.4	-115443.9	-115250.1
$2p_{3/2}$	-114187.8	-111674.2	-111596.0	-111468.7
$3s_{1/2}$	-53276.2	-43553.2	-43650.9	-43513.4
$3p_{1/2}$	-53276.2	-51122.5	-51106.6	-51042.3
$3p_{3/2}$	-51001.3	-50101.0	-50076.4	-50032.1
$3d_{3/2}$	-51001.3	-50980.2	-50978.1	-50976.4
$3d_{5/2}$	-50329.8	-50322.2	-50320.8	-50319.9
$4s_{1/2}$	-29607.2	-25412.2	-25456.7	-25395.6
$4p_{1/2}$	-29607.2	-28664.8	-28658.5	-28630.5
$4p_{3/2}$	-28652.8	-28250.6	-28240.1	-28220.4
$4d_{3/2}$	-28652.8	-28640.1	-28638.8	-28637.8
$4d_{5/2}$	-28368.1	-28363.4	-28362.6	-28362.1
$4f_{5/2}$	-28368.1	-28368.1	-28368.1	-28368.1
$4f_{7/2}$	-28229.6	-28229.6	-28229.6	-28229.6

TABLE VII: Same as in Tab. VI but for the $n\ell_j$ states of the muonic $^{163}\text{Dy}^{65+}(\mu^-)$ ion.



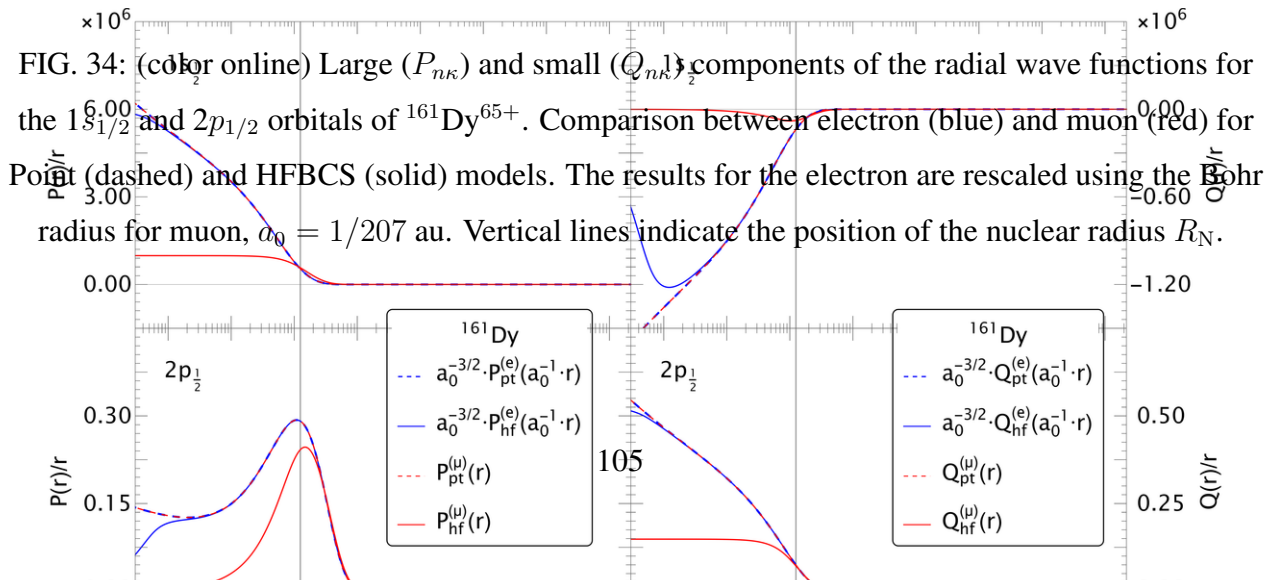
$n\ell_j$	E^{sp}	E^{fm}	E^{hf}
$1s_{1/2}$	-2321.0242	-2321.0249	-2321.0245
$2s_{1/2}$	-589.5579	-589.5581	-589.5580
$2p_{1/2}$	-589.6268	-589.6268	-589.6268
$2p_{3/2}$	-552.6315	-552.6315	-552.6315
$3s_{1/2}$	-257.8177	-257.8178	-257.8177
$3p_{1/2}$	-257.8381	-257.8381	-257.8381
$3p_{3/2}$	-246.8293	-246.8293	-246.8293
$3d_{3/2}$	-246.8293	-246.8293	-246.8293
$3d_{5/2}$	-243.5797	-243.5797	-243.5797
$4s_{1/2}$	-143.2799	-143.2799	-143.2799
$4p_{1/2}$	-143.2884	-143.2884	-143.2884
$4p_{3/2}$	-138.6699	-138.6699	-138.6699
$4d_{3/2}$	-138.6699	-138.6699	-138.6699
$4d_{5/2}$	-137.2922	-137.2922	-137.2922
$4f_{5/2}$	-137.2922	-137.2922	-137.2922
$4f_{7/2}$	-136.6220	-136.6220	-136.6220

$n\ell_j$	E^{sp}	E^{fm}	E^{hf}
$1s_{1/2}$	-283536.8	-284602.4	-284560.7
$2s_{1/2}$	-90405.7	-90677.2	-90671.6
$2p_{1/2}$	-115315.7	-115256.5	-115250.1
$2p_{3/2}$	-111551.3	-111473.7	-111468.7
$3s_{1/2}$	-43419.0	-43515.2	-43513.4
$3p_{1/2}$	-51060.0	-51044.4	-51042.3
$3p_{3/2}$	-50058.0	-50033.7	-50032.1
$3d_{3/2}$	-50978.7	-50976.5	-50976.4
$3d_{5/2}$	-50321.5	-50320.0	-50319.9
$4s_{1/2}$	-25352.5	-25396.3	-25395.6
$4p_{1/2}$	-28637.6	-28631.4	-28630.5
$4p_{3/2}$	-28231.5	-28221.1	-28220.4
$4d_{3/2}$	-28639.2	-28637.9	-28637.8
$4d_{5/2}$	-28363.0	-28362.1	-28362.1
$4f_{5/2}$	-28368.1	-28368.1	-28368.1
$4f_{7/2}$	-28229.6	-28229.6	-28229.6

(a) Binding energies for the electronic $^{163}\text{Dy}^{65+}$ ion.

(b) Binding energies for the muonic $^{163}\text{Dy}^{65+}(\mu^-)$ ion.

TABLE VIII: Binding energies in Hartrees for different $n\ell_j$ states of the $^{163}\text{Dy}^{65+}$ ion, with spherical and Fermi distributions normalised for the same R_{rms} values as the HFBCS model.



(a) Electronic orbitals of $^{161}\text{Dy}^{65+}$.

(b) Muonic orbitals of $^{161}\text{Dy}^{65+}(\mu^-)$.

FIG. 35: (color online) Monopolar shifts in the energy levels of electronic orbitals of $^{161}\text{Dy}^{65+}$ (from $1s_{1/2}$ to $4f_{7/2}$) in different nuclear models, Point (pt), Spherical (sp), Fermi (fm) and HFBCS (hf). We have defined, $\Delta E_{m_1,i}^{m_2} \equiv \frac{E_i^{m_2} - E_i^{m_1}}{E_i^{m_1}}$ with $m_2 \in \{\text{sp, fm, hf}\}$ and $m_1 \in \{\text{pt, fm}\}$ and $\Delta E_{163,i}^{161} \equiv \frac{E_i^{161} - E_i^{163}}{E_i^{163}}$ with i running from $1s_{1/2}$ to $4f_{7/2}$. This latter quantity was evaluated using the energies of the HFBCS model.

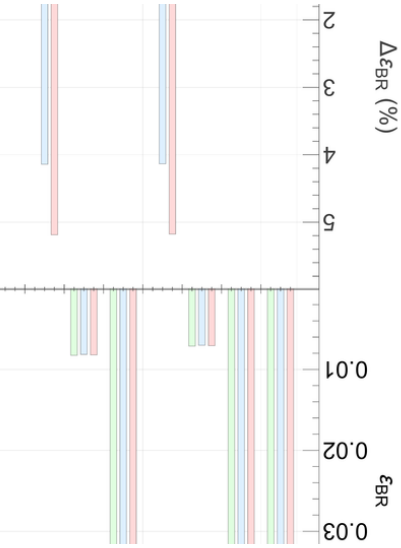


FIG. 36: (color online) (Upper panel) Breit-Rosenthal correction ε_{BR} for $^{161}\text{Dy}^{65+}$ in different nuclear models: Spherical, Fermi and HFBCS. (Lower panel) We have defined, $\Delta\varepsilon_{\text{fm}}^{\text{hf}} \equiv \frac{\varepsilon_{\text{BR}}^{\text{hf}} - \varepsilon_{\text{BR}}^{\text{fm}}}{\varepsilon_{\text{BR}}^{\text{fm}}}$ (reading on the left axis) and $\Delta\varepsilon_{163}^{161} \equiv \frac{\varepsilon_{\text{BR}}^{\text{hf}}(161) - \varepsilon_{\text{BR}}^{\text{hf}}(163)}{\varepsilon_{\text{BR}}^{\text{hf}}(163)}$ (reading on the right axis).

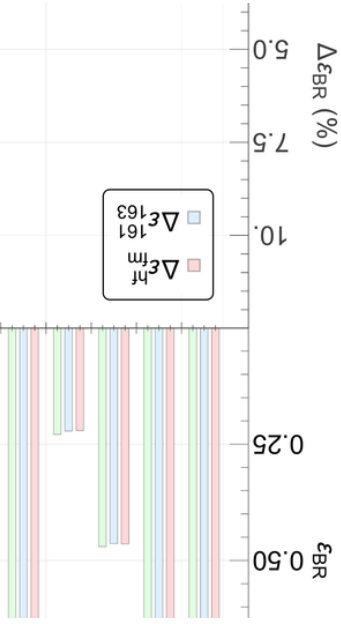


FIG. 37: (color online) Same as Fig. 36 but for a muonic hydrogen-like ion.

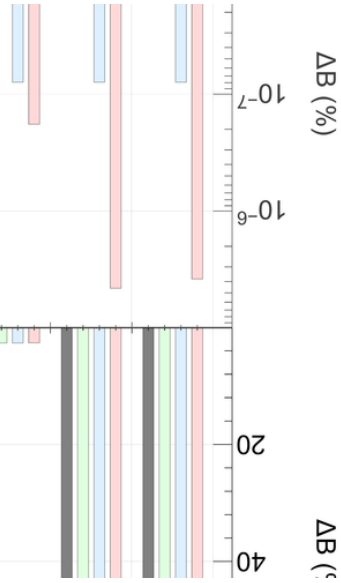


FIG. 38: (color online) Quadrupole shifts for electronic $^{161}\text{Dy}^{65+}$. (Upper panel) $\Delta B^m \equiv \frac{b_{\text{np}}^{\text{pt}} - b_{\text{wp}}^m}{b_{\text{np}}^{\text{pt}}}$ with $m \in \{\text{pt}, \text{sp}, \text{fm}, \text{hf}\}$ and subscript indices np and wp representing calculations with no penetration and with penetration, respectively. (Lower panel) Two quantities are depicted: $\Delta B \equiv \frac{b_{\text{wp}}^{\text{fm}} - b_{\text{wp}}^{\text{hf}}}{B_{\text{wp}}^{\text{fm}}}$ for $^{161}\text{Dy}^{65+}$ (in red and reading on the left axis) and $\Delta B_{161}^{163} \equiv \frac{b_{\text{wp}}^{\text{hf}}(161) - b_{\text{wp}}^{\text{hf}}(163)}{b_{\text{wp}}^{\text{hf}}(163)}$ (in blue and reading on the right axis). Note that the $s_{1/2}$ and $p_{1/2}$ contributions are zero.

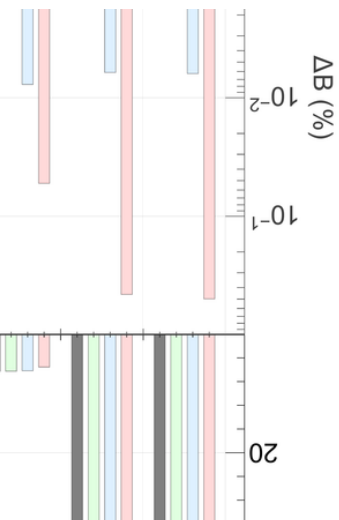


FIG. 39: (color online) Same as Fig. 38 but for muonic $^{161}\text{Dy}^{65+}$.

-
- [1] L. Essen and J. V. L. Parry, *Nature*, **176**, 280 (1955).
- [2] E. Peik and Y. N. Okhapkin, *C. R. Physique* **16**, 516 (2015).
- [3] F. F. Karpeshin, S. Wycech, I. M. Band, M. B. Trzhaskovskaya, M. Pfützner, and J. Żylicz, *Phys. Rev. C* **57**, 3085 (1998).
- [4] E. V. Tkalya and A. V. Nikolaev, *Phys. Rev. C* **94**, 014323 (2016).
- [5] B. Seiferle et al., *Nature* **573**, 243 (2019).
- [6] C. J. Campbell, A. G. Radnaev, and A. Kuzmich, *Phys. Rev. Lett.* **106**, 223001 (2011)
- [7] H. W. T. Morgan, H. B. Tran Tan, R. Elwell, A. N. Alexandrova, Eric R. Hudson, and Andrei Derevianko, *Phys. Rev. Lett.* **134**, 253801 (2025).
- [8] C. Mény and P. Panissod, *Modern Magnetic Resonance*, Springer International Publishing (2017).
- [9] S. Thiele, F. Balestro, R. Ballou, S. Klyatskaya, M. Ruben and W. Wernsdorfer, *Science* **344**, 1135 (2014).
- [10] C. Godfrin, A. Ferhat, R. Ballou, S. Klyatskaya, M. Ruben, W. Wernsdorfer and F. Balestro, *Phys. Rev. Lett.* **119**, 187702 (2017).
- [11] X. Yu, B. Wilhelm, D. Holmes, A. Vaartjes, D. Schwienbacher, M. Nurizzo, A. Kringhøj, M.R. van Blankenstein, A.M. Jakob, P. Gupta, F.E. Hudson, K.M. Itoh, R.J. Murray, R. Blume-Kohout, T.D. Ladd, N. Anand, A.S. Dzurak, B.C. Sanders, D.N. Jamieson and A. Morello, *Nature Physics* **21**, 362 (2025).
- [12] R. Pohl, A. Antognini, F. Nez, F.D. Amaro, F. Biraben, J.M.R. Cardoso, D.S. Covita, A. Dax, S. Dhawan, L.M.P. Fernandes, A. Giesen, T. Graf, T.W. Hänsch, P. Indelicato, L. Julien, C.-Y. Kao, P. Knowles, E.-O. Le Bigot, Y.-W. Liu, J.A.M. Lopes, L. Ludhova, C.M.B. Monteiro, F. Mulhauser, T. Nebel, P. Rabinowitz, J.M.F. dos Santos, L.A. Schaller, K. Schuhmann, C. Schwob, D. Taqqu, J.F.C.A. Veloso and F. Kottmann, *Nature* **466**, 213 (2010).
- [13] A. Antognini, F. Nez, K. Schuhmann, F.D. Amaro, F. Biraben, J.M.R. Cardoso, D.S. Covita, A. Dax, S. Dhawan, M. Diepold, L.M.P. Fernandes, A. Giesen, A.L. Gouvea, T. Graf, T.W. Hänsch, P. Indelicato, L. Julien, C.-Y. Kao, P. Knowles, F. Kottmann, E.-O. Le Bigot, Y.-W. Liu, J.A.M. Lopes, L. Ludhova, C.M.B. Monteiro, F. Mulhauser, T. Nebel, P. Rabinowitz, J.M.F. dos Santos, L.A. Schaller, C. Schwob, D. Taqqu, J.F.C.A. Veloso, J. Vogelsang and R. Pohl, *Science* **339**, 417 (2013).

- [14] J. E. Rosenthal and G. Breit, Phys. Rev. **41**, 459 (1932).
- [15] A. Bohr and V. F. Weisskopf, Phys. Rev. **77**, 94 (1950).
- [16] F. F. Karpeshin and M. B. Trzhaskovskaya, Nucl. Phys. A **941**, 66 (2015).
- [17] B.M. Roberts and J.S.M. Ginges, Phys. Rev. A **104**, 022823 (2021).
- [18] A.V. Volotka, D.A. Glazov, O.V. Andreev, V.M. Shabaev, I.I. Tupitsyn and G. Plunien, Phys. Rev. Lett. **108**, 073001 (2012).
- [19] M. Bender, P.-H. Heenen, and P.-G. Reinhard, Rev. Mod. Phys. **75**, 121 (2003).
- [20] E Moreno-Pineda, C Godfrin, F Balestro, W Wernsdorfer, M Ruben, Chemical Society Reviews **47**, 501 (2018).
- [21] A. V. Volotka, D. A. Glazov, G. Plunien, and V. M. Shabaev, Ann. Phys. (Berlin) **525**, 636 (2013).
- [22] S. Boucard, PhD thesis, Université Pierre et Marie Curie – Paris VI (1998).
- [23] S. Boucard and P. Indelicato, Eur. Phys. J. D **8**, 59 (2000).
- [24] U.D. Jentschura, Canadian Journal of Physics **89**, 109 (2011).
- [25] N.S. Oreshkina, Phys. Rev. Res. **4**, L042040 (2022).
- [26] V.M. Shabaev, A.N. Artemyev, V.A. Yerokhin, O.M. Zhrebtsov and G. Soff, Phys. Rev. Lett. **86**, 3959 (2001).
- [27] A.N. Artemyev, V.M. Shabaev, G. Plunien, G. Soff and V.A. Yerokhin, Phys. Rev. A **63**, 062504 (2001).
- [28] J.R. Persson, arXiv:2310.16398 (2025).
- [29] Paul Scherrer Institute (PSI), Swiss Muon Source ($S\mu S$), facility overview and beamlines (accessed Oct. 2025).
- [30] Harald Friedrich, Theoretical Atomic Physics, Springer (2017).
- [31] K. A. Brueckner, Phys. Rev. **97**, 1353 (1955).
- [32] J. W. Negele, Phys. Rev. C **1**, 1260 (1970).
- [33] J. W. Negele, Rev. Mod. Phys. **54**, 913 (1982).
- [34] K. T. R. Davies, M. Baranger, Phys. Rev. C **1**, 1640 (1970).
- [35] X. Campi, D. W. Sprung, Nucl. Phys. A **194**, 401 (1972).
- [36] D. Gogny, Nuclear self-consistent fields, Trieste, 1975, eds. G. Ripka and M. Porneuf (North Holland, Amsterdam, 1975) p. 333.
- [37] J. Dechargé and D. Gogny, Phys. Rev. C **21**, 1568 (1980).

- [38] S. A. Moszkowski, Phys. Rev. C **2**, 402 (1970).
- [39] T. H. R. Skyrme, Nucl. Phys. **9**, 615 (1959).
- [40] D. Vautherin, D. M. Brink, Phys. Rev. C **5**, 626 (1972).
- [41] D. Vautherin, Phys. Rev. C **7**, 296 (1973).
- [42] M. J. Giannoni, P. Quentin, Phys. Rev. **21**, 2076 (1980).
- [43] J. Engel, D. Brink, K. Goeke, S. J. Krieger, D. Vautherin, Nucl. Phys. A **249**, 215 (1975).
- [44] V. Hellemans, P. -H. Heenen, M. Bender, Phys. Rev. C **85**, 014326 (2012).
- [45] L. Bonneau, N. Minkov, Dao Duy Duc, P. Quentin, J. Bartel, Phys. Rev. C **91**, 054307 (2015).
- [46] Density Functional Theory in Quantum Chemistry, Takao Tsuneda. (2014).
<https://doi.org/10.1007/978-4-431-54825-6>
- [47] W. Kohn and L. J. Sham, Phys. Rev. **140**, 1133 (1965).
- [48] M. Beiner, H. Flocard, Nguyen van Giai and P. Quentin, Nucl. Phys. **A283** (1975) 29.
- [49] J. Bartel, P. Quentin, M. Brack, C. Guet and H.-B. Håkansson, Nucl. Phys. A **386**, 79 (1982).
- [50] E. Chabanat, P. Bonche, P. Haensel, J. Meyer, R. Schaeffer, Nucl. Phys. A **627**, 710 (1997).
- [51] E. Chabanat, P. Bonche, P. Haensel, J. Meyer, R. Schaeffer, Nucl. Phys. A **635**, 231 (1998).
- [52] T. Lesinski, M. Bender, K. Bennaceur, T. Duguet, J. Meyer, Phys. Rev. C **76**, 014312 (2007).
- [53] M. Bender, K. Bennaceur, T. Duguet, P.-H. Heenen, T. Lesinski, J. Meyer, Phys. Rev. C **80**, 064302 (2009).
- [54] S. Goriely, N. Chamel, and J. M. Pearson, Phys. Rev. C **82**, 035804 (2010).
- [55] S. Sadoudi, T. Duguet, J. Meyer, M. Bender, Phys. Rev. C **88**, 064326 (2013).
- [56] S. Goriely, N. Chamel, J. M. Pearson, Phys. Rev. C **88**, 061302(R) (2013).
- [57] J. M. Pearson, N. Chamel, Phys. Rev. C **105**, 015803 (2022).
- [58] J. C. Slater, Phys. Rev. **81**, 385 (1951).
- [59] J. Damgaard, H. -C. Pauli, V. V. Paskhevich, and V. M. Strutinsky, Nucl. Phys. A **135**, 432 (1969).
- [60] H. Flocard, P. Quentin, A. K. Kerman and D. Vautherin, Nucl. Phys. A **203**, 433 (1973).
- [61] F. Chappert, N. Pillet, M. Girod, J. -F. Berger, Phys. Rev. C **91**, 034312 (2015).
- [62] C. Gonzales-Boquera, M. Centelles, X. Viñas, L. M. Robledo, Phys. Lett. B **779**, 195 (2018).
- [63] J. Dobaczewski, H. Flocard and J. Treiner, Nucl. Phys. A **422**, 103 (1984).
- [64] P. Ring and P. Schuck, *The Nuclear Many-Body Problem* (Springer, 1980).
- [65] Nurhafiza M. Nor, Nor-Anita Rezle, Kai-Wen Kelvin Lee, L. Bonneau, and P. Quentin, Phys. Rev. C

- 99**, 064306 (2019).
- [66] F. Herbut and M. Vujičić, *Phys. Rev.* **172**, 1031 (1968).
- [67] K. J. Pototzky, J. Erler, P.-G. Reinhard, and V. O. Nesterenko, *Eur. Phys. J. A* **46**, 299 (2010).
- [68] C. W. Reich and B. Singh, *Nucl. Data Sheets* **112**, 2497 (2011).
- [69] C. W. Reich and B. Singh, *Nucl. Data Sheets* **111**, 1211 (2010).
- [70] Y. K. Gambhir, P. Ring and A. Thimet, *Ann. Phys.* **198**, 132 (1990).
- [71] P. J. Moher, D. B. Newell, B. N. Taylor, and E. Tiesinga, *Rev. Mod. Phys.* **97**, 025002 (2025).
- [72] N. J. Stone, *Atomic Data and Nuclear Data Tables* **90** (2005) 75.
- [73] A. Pálffy, *Contemporary Physics*, **51**, 471 (2010).
- [74] N. J. Stone, *At. Data Nucl. Data Tables* **111**,1 (2016).
- [75] C. W. Reich, *Nucl. Data Sheets* **113**, 157 (2012).
- [76] B. Singh and J. Chen, *Nucl. Data Sheets* **194**, 460 (2024).
- [77] C. Schwartz, *Phys. Rev.* **97**, 380 (1955).
- [78] M. Chemtob, *Nucl. Phys. A* **123**, 449 (1969).
- [79] Å. Bohr and B. R. Mottelson, "Nuclear Structure" Vol. 2, Benjamin, New York, 1975.
- [80] O. Prior, F. Boehm, S. G. Nilsson, *Nucl. Phys. A* **110**, 257 (1968).
- [81] D. W. L. Sprung, S. G. Lie, M. Vallieres and P. Quentin, *Nucl. Phys. A* **326**, 37 (1979).
- [82] P. Strange, *Relativistic Quantum Mechanics*, Cambridge University Press, (2005).
- [83] José R. Crespo López-Urrutia, P. Beiersdorfer, Daniel W. Savin, and Klaus Widmann, *Phys. Rev. Lett.* **77**, 826 (1996).
- [84] W. R. Johnson, *Atomic Structure Theory, Lectures on Atomic Physics*, Springer (2007).
- [85] J. E. Rosenthal and G. Breit, *Phys. Rev.* **41**, 459 (1932).
- [86] A. Bohr and V. Weisskopf, *Phys. Rev.* **77**, 94 (1950).
- [87] S. Büttgenbach, *Hyperfine Interactions* **20**, 1 (1984).
- [88] R.P. de Groote and G. Neyens, *Spins and Electromagnetic Moments of Nuclei*, in *Handbook of Nuclear Physics*, ed. I. Tanihata, H. Toki and T. Kajino, Springer Nature, Singapore, (2020), pp. 1–36.
- [89] J. Vandeleur, G. Sanamyan, O.R. Smits, I.A. Valuev, N.S. Oreshkina and J.S.M. Ginges, *Phys. Rev. Lett.* **134**, 093003 (2025).
- [90] J. R. Persson, arXiv:2304.11995, 2023.
- [91] A. J. Freeman, J. V. Mallow, J. P. Desclaux, and M. Weinert, *Hyperfine Interact.* **19**, 865 (1984).

- [92] A. Pérez Galván, Y. Zhao, L. A. Orozco, E. Gómez, A. D. Lange, F. Baumer, and G. D. Sprouse, Phys. Lett. B **655**, 114 (2007).
- [93] H.P. Povel, Nuclear Physics A **217**, 573 (1973).
- [94] N. Michel, N.S. Oreshkina and C.H. Keitel, Phys. Rev. A **96**, 032510 (2017).
- [95] N. Michel and N.S. Oreshkina, Phys. Rev. A **99**, 042501 (2019).
- [96] D.A. Varshalovich, A.N. Moskalev and V.K. Khersonskii, Quantum Theory of Angular Momentum, World Scientific, Singapore, (1988). Da
- [97] D.J. Rowe, Nuclear Collective Motion, Methuen, London, (1970).
- [98] A. Bohr and B.R. Mottelson, Nuclear Structure, Vol. II, Benjamin, New York, (1975).
- [99] A. Bohr and B.R. Mottelson, Nuclear Structure, Vol. I, Benjamin, New York, (1969).
- [100] Note1, note that the notation is different in the Appendix VIII A: we have $M_z^{(1),(\text{spec})} \equiv M_{10}^{(\text{spec})}$.
- [101] Note2, note that the notation is different in the Appendix VIII A: we have $Q_0^{(2),(\text{spec})} \equiv Q_{20}^{(\text{spec})}$.
- [102] Note3, $i \left(\psi_{n,\ell}^* \nabla \psi_{n,\ell} - \psi_{n,\ell} \nabla \psi_{n,\ell}^* \right)$.